Lehrstuhl für Technische Elektrophysik

Modelling and Diagnostics of Low Pressure Plasma Discharges

Peter Scheubert

Vollständiger Abdruck der von der Fakultät für Elektrotechnik und Informationstechnik
der Technischen Universität München zur Erlangung des akademischen Grades eines
Doktors-Ingenieur (Dr.-Ing.)
genehmigten Dissertation.

Vorsitzender: Univ.-Prof. Dr.-Ing. habil. A. W. Koch
Prüfer der Dissertation:

1. Univ.-Prof. Dr. rer. nat. G. Wachutka
2. Univ.-Prof. Dr. rer. nat R. P. Brinkmann
3. Priv.-Doz. Dr.-Ing., Dr.-Ing. habil. P. Awakowicz

Die Dissertation wurde am 17.10.2001 bei der Technischen Universität München
eingereicht und durch die Fakultät für Elektrotechnik und Informationstechnik
am 26.02.2002 angenommen.

to all carrots growing on this planet

Contents

Zusammenfassung

Niederdruck-Plasmaverfahren sind zum unverzichtbaren Bestandteil moderner Hochtechnologieprozesse geworden. Neben einer Vielzahl innovativer Anwendungen im Bereich Oberflächenbehandlung bzw. -veredelung sowie Beleuchtungstechnik ist vor allem der Einsatz von Niederdruckentladungen in der Fertigung von Halbleitern bzw. Flachbildschirmen von wirtschaftlicher Bedeutung. Typischerweise sind Plasmaverfahren bei der Herstellung einer modernen integrierten Schaltung an bis zu 50 Teilprozeßschritten beteiligt. Die zunehmende Integrationsdichte und die stetig steigenden Anforderungen an die Ausbeute der Einzelschritte erfordern in zunehmendem Maße ein grundlegendes Verständnis der komplexen physikalischen sowie plasmachemischen Prozesse.

Die vorliegende Arbeit gibt einen Überblick, wie die in Niederdruckplasmen ablaufenden Transportprozesse mittels geeigneter mathematischer Modelle verstanden werden können. In gleichem Maße wird auf eine Validierung der theoretischen Daten Wert gelegt. Neben allgemeinen Betrachtungen zur Gültigkeit von hydrodynamischen Beschreibungen liegt der Schwerpunkt bei der Beschreibung moderner induktiver Plasmaquellen, wie sie vermehrt in der Halbleiterfertigung eingesetzt werden. Die Modellrechnungen werden vielfach mit experimentellen Daten verglichen. Es wird nachgewiesen, daß hydrodynamische Modelle in der Lage sind, mit großer Genauigkeit Elektronendichteverteilungen sowie Teilchenflüsse vorherzusagen. Neben einer ausführlichen und vergleichenden Diskussion verschiedener Modellsysteme wird im eindimensionalen Fall eine Empfindlichkeitsanalyse durchgeführt, die den Einfluß der zugrundeliegenden Eingabedaten der Modelle diskutiert. Große Aufmerksamkeit wird hierbei der Frage der Gültigkeit vereinfachter Modelle gewidmet, d.h. in welchen Bereichen evtl. vereinfachte, und deshalb schnellere und stabilere Modelle eingesetzt werden können.

Die gesamte Veröffentlichung gliedert sich in drei Teile. Um einen qualitativen Vergleich der verschieden komplexen Modellansätze zu ermöglichen, wird zunächst die allgemeine Klasse hydrodynamischer Modellsysteme aus der Boltzmann-Gleichung hergeleitet. Anhand einzelner Vereinfachungen gelangt man zu Erhaltungsgleichungen für Masse, Impuls und Energie. Die Frage einer numerischen Lösung, ebenso wie die Wahl geeigneter Randbedingungen, wird mit Hinblick auf bereits vorliegende Arbeiten anderer Autoren ausführlich diskutiert. Im zweiten Teil werden für eindimensionale Testprobleme die verschiedenen denkbaren Modellansätze qualitativ verglichen und die Gültigkeitsbereiche sowie Empfindlichkeiten gegenüber den verwendeten Eingabedaten analysiert. Im letzten Teil schließlich werden zweidimensionale induktive Entladungen behandelt. Theoretische Ergebnisse werden mit experimentellen Daten, gewonnen aus Sondenmessungen, verglichen und bestätigen in einem weiten Parameterbereich

die Anwendbarkeit hydrodynamischer Transportmodelle. Die abschließenden Abschnitte sind der Thematik Designregeln gewidmet. Exemplarisch wird dargestellt, wie mittels geeigneter optimierter Geometrie der Entladungskammer ein optimales Prozeßergebnis erzielt werden kann. Die wesentlichen physikalischen Grundmechanismen, die bei dem Entwurf von Entladungen ber”ucksichtigt werden sollten und eine Reihe von “Faustregeln” die Kammerdesign ohne aufwendige Modellrechnungen ermöglichen, werden diskutiert.

Summary

The presented thesis deals with various aspects of models for low pressure discharges. As well the theoretical background of hydrodynamic plasma models as the comparison of calculated data with experimental results are discussed.

In the first part of this work hydrodynamic conservation equations are derived from the Boltzmann equation. Main focus is the application to low pressure plasmas. Different model systems for electrons and ions are presented. The question in which case simplified models can be applied, is treated as well as numerical aspects and algorithms for obtaining a solution are discussed.

In a second part hydrodynamic models were used for performing one-dimensional simulations. The sensitivity of the model in dependence of input parameters like momentum exchange frequencies was analysed. As well different model systems were compared qualitatively in order to get an estimate for the error introduced by using simple and numerical more stable model systems.

In the third part hydrodynamic models were applied to simulate different kinds of low pressure discharges. Main focus were inductively driven plasmas like they are used in semiconductor fabrication as high density plasma source. Calculated data for this kind of discharge were compared with experimental values obtained from Langmuir probe measurements. Theory and experiment show very good agreement.

In a final part the scaling laws and geometry dependence derived from hydrodynamic models were used to assemble a set of general reactor design rules. Examples were presented, how reactor performance can be optimised by careful choice of geometry parameters. Also general dependencies on external parameters like discharge pressure were discussed.

Acknowledgements

For giving me the opportunity to perform this work as a member of the Institute for Physics of Electrotechnology, I would like to thank Univ.-Prof. Dr. rer. nat. Gerhard Wachutka. In numerous discussions he gave me support, pointing me especially on the analogies, showing the close relationship between semiconductor device simulation and modelling of low temperature plasma processes. Also, the excellent computer network and the various software tools being present at his institute were an essential prerequisite which made this work possible.

I am greatly indebted to Univ.-Prof. Dr. rer. nat. Ralf-Peter Brinkmann for essentially supporting me in critical moments of my work. By knowing the right numerical method for the right problem, he saved me more than once from having to code another dozen of possibilities which I would have tried to solve the problem. Also, his deep expertise concerning the theoretical background of low pressure plasmas more than once showed me the way in a difficult terrain.

My special thanks go to PD Dr. Peter Awakowicz who convinced me to undertake the adventure of writing a theoretical work with only limited knowledge about the theory of low pressure plasmas being available in the department. He gave me every possible support and was present all the time when some important decision had to be made. He also gave me the opportunity to perform a number of inhouse experiments in order to validate the theoretical results.

I also wish to thank my former and present colleagues Franz Burkhard Anschütz, Evelyn Landerer and Roland Schwefel for the cooperation in the plasma group of the institute. We did not only work together on common projects but also shared various spare time activities with each other.

In addition, I would like to thank all the other colleagues working at the Institute for Physics of Electrotechnology for their active cooperation and the overall atmosphere which remained friendly even when we were collectively stressed by advancing deadlines. Just as an example for them all I would like to mention the system administration group consisting of Winfried Kaindl, Peter Böhm, Stefan Schaub, Martin Lades and Robert Thalhammer and the electronic laboratory managed by Georg Heinzerling and Erich Steinmuss. For carefully proofreading and finding numerous typos in this thesis, my special thanks go to Dr. Gernot Keil and Peter Meßerer.

Furthermore I am particularly thankful to Dr. Ursel Fantz and her group at University of Augsburg for various discussions about inductive discharges and experimental cooperation. The experimental results measured in their ICP discharge were the final proof the accuracy of my own modelling activities.

My work has been supported by different students. I would like to mention the commitment of my diploma student Hannes Hoedl, the creative potential of Sigrid Zanon and the mathematical support by Georg Wenig. I especially want to thank Petra Wagner for finding literature I needed and her psychological support.

For partially funding the experimental part of this work, I would like to thank the Dr. Johannes Heidenhain Stiftung.

Last but not least I enjoyed all my friends being appreciative of me when I had to work on my thesis while the conditions would have been ideal for spending a weekend in my beloved Alps. They also consoled me whenever I could not climb difficult routes due to a lack of training.

Finally, I would like to express a warm thanks to my partner Stefanie Michalski who offered me essential support and frequently helped me to reach another step leading to the summit.

Chapter 1

Introduction

1.1 Application of low pressure, low temperature plasmas

Low pressure plasma discharges are used in an increasing number of technical applications. Examples are the deposition of thin films like for hardening of tools or to produce coatings with optical properties. While a great variety of applications for plasma processes exists[1], from an economical point of view, the most important field is semiconductor and flat panel display fabrication.

For example, more than 50 plasma steps are involved in producing a modern PC processor-chip. Low pressure, low temperature discharges are used for cleaning, etching, deposition and stripping. Plasma processing is one of the key technologies in modern semiconductor manufacturing. About 30 percent of all process steps involve plasma. During the last years, especially inductively driven high density plasma sources [46] were introduced for semiconductor fabrication processes.

According to the roadmap of the Semiconductor Industry Association [2], the future challenges for etch processing are largely driven by the decreasing critical dimensions and the need to use new materials:

> “The most challenging front end etch technical requirements are maintaining low bias and high uniformity of edge profile at continually larger wafer diameters and obtaining the required etch selectivity and etch profiles for the new materials.”

Especially, because of the large substrate diameters and the increasing number of process steps, a maximum yield must be guaranteed for each single step. For plasma process steps this means especially:

- Plasma parameters like ion flux or ion velocity should be as homogeneous as possible over the whole wafer area. The typical variation of deposition or etch rates should not exceed two percent.

---

[1] More exotic examples are the treatment of wool before dyeing, the coating of PET bottles in order to reduce oxidation of the filling, the sterilisation of medical equipment or plasma deposited anti-grafitti coatings.

- For sequentially processed wafers, the deposition or etch rates should be the same.
- As long as possible, the operating conditions in a reactor chamber should not vary.

It has to be emphasised that the desired results (uniformity of etch and deposition rate) will depend on a variety of interacting internal parameters of the process discharge like the electron density, electron temperature, neutral gas temperature, species concentration, ion fluxes, ion energies, potential distributions or the electron distribution function.

The internal parameters of the discharge, on the other hand, depend on externally adjustable parameters like discharge power, the process gases and their pressure, the externally applied magnetic fields or bias voltages. They have to be adjusted in order to optimise the process. The discharge geometry has a crucial influence on the process as well, but normally can not be varied while the process is in operation.

In Fig. 1.1 for an RF-discharge the interdependence of internal discharge parameters, external parameters (which can be chosen by the operator) and the process result are shown. From the manufacturer's point of view, the main goal is to design a reactor chamber and to find external process parameters which guarantee the process to operate stable and to deliver reproducible results.

While the internal parameters of the plasma process obviously have a crucial influence on the desired result, in a real world application the user of a plasma process (e.g. a semiconductor manufacturer) is often not aware of these internal parameters nor of their interdependence. This unconsciousness might not be satisfactory,, not only from a scientific point of view. The introduction of each new technology generation, i.e. decreasing structure sizes in combination with increasing wafer diameters, and shrinking tolerance margins narrow the size of the process window.

In future, it will not longer be possible to run processes without an understanding of the basic relations between the internal parameters. A process control by an accurate timing of each step might not be able to guarantee a result within the specified margins. This is the main reason why modelling of process equipment and the understanding of physical principles over the last years has become a topic not only for principle researchers, but also for process engineers.

1.2 Modelling of low pressure plasmas

A serious problem relating to increasing wafer sizes is the question of scalability of existing processes. The step to a larger wafer diameter requires more effort than just an up-scaling of existing reactor designs. As the costs for the equipment tend to increase massively from one technology generation to the next, an expensive try-and-error approach is unacceptable.

This answers the question, why simulation of low pressure plasma processes is of fundamental interest. Simulation can provide valuable information about internal parameters which otherwise could only be determined with high experimental effort. It is the only possibility to study the properties of a new discharge chamber without actually building it. This opinion is shared by the SIA roadmap authors, who expect an increasing importance of reactor models in the near future [2]:

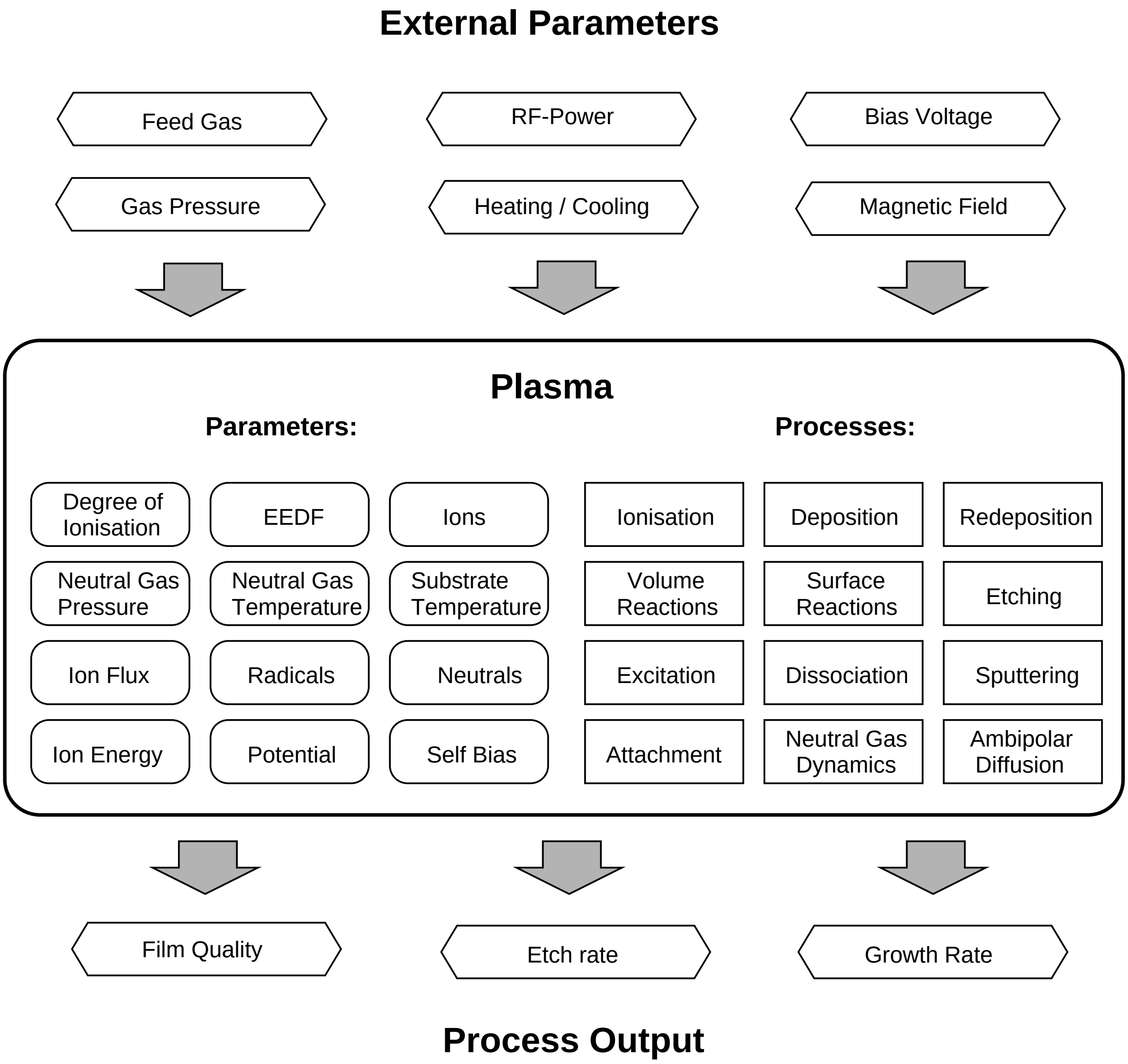

Figure 1.1: Influence of external parameters like RF-power and gas supply on the process parameters for radio frequency low pressure discharges. The external parameters determine characteristic internal parameters like electron density, the electron energy distribution function (EEDF), ion fluxes and energy. The desired process output depends directly on the internal parameters of the discharge.

> “Plasma modelling and simulation is one of the more difficult unit process simulation areas. Accurate plasma models, the link of this gas phase models to the features on a wafer (such as good sheath models), and the ability to predict the equipment related variations across a wafer would lead to a significant improvement in process understanding.”

While the need for accurate simulations is obvious, it is a very demanding task, as for real process applications an enormous number of coupled physical as well as chemical processes is involved. Input parameters like reaction rates, ionisation, excitation, and charge exchange cross sections or emission rate coefficients would be required for the process gases, the important radicals and unstable chemical species which are present in a process plasma. Unfortunately, data are only known for a limited number of materials or gases.

Furthermore, it is very difficult to test the reliability of a simulation result as only spectroscopic methods provide the possibility to measure the concentration of species inside the discharge without perturbing the setup. The experimental effort can be enormous, and even then it might not be possible to determine the concentration of all the involved species.

A very sensitive diagnostic method is the energy and mass spectroscopy (EMS). It provides mass selective information about particles (ions or neutrals) leaving the discharge. A valuable insight into the chemical reactions and their products might be acquired. But only those particles can be detected which leave the discharge. A direct measurement of internal parameters or volume processes is not possible. This reflects the second problem complicated plasma models suffer from:

The input parameters are unknown, and it is also impossible to compare simulation results with experimental data. Only those quantities which can be directly measured and spatially resolved are useful for model calibration. These are, for example, the electron density, the potential distribution, and the mean electron energy. For process applications relative species concentrations would be interesting. In previous works, different authors presented calculations for typical process gases [98], [65], [116] but did not show corresponding experimental results.

The goal of this thesis is to provide an overview of different approaches to model low temperature, low pressure plasma discharges. Especially the case of inductively coupled discharges (ICPs) will be treated. Different models and their specific advantages will be discussed and compared. The class of hydrodynamic models, which assume the plasma to be a mixture of different interacting fluids, will be especially dealt with. If it is possible, the presented simulation results will be compared with the corresponding experimental data. All used input parameters will be presented, and the references to the literature from which these parameters were taken will be given. The sensitivity of the models with respect to various input parameters will be discussed.

1.3 Diagnostics

In the previous section, the importance of diagnostic methods for evaluating and calibrating models of low pressure discharges was mentioned. But also diagnostics of real process applications can be expected to become more and more important in the near future. The reason again is the shrinking of tolerance margins for plasma processes caused by the technological advance in semiconductor fabrication.

Up to now, in many cases plasma processes in industrial environments were only controlled by the process timing. A very high effort is spent to ensure a maximum reproducibility, to guarantee that each batch of wafers is processed under identical conditions. On the other hand, it is well known that the coating of a process chamber during several days of operation causes a shift in the process parameters. The industrial answer to this problem is a regular cleaning of the chamber. However, recent investigations [101] showed that even directly after a clean cycle the measured internal discharge parameters like the electron density can vary dramatically. This means that the time and the effort spent for cleaning the chamber cannot guarantee identical process conditions. Furthermore, the conditions in a clean chamber are normally out of the process window, so that typically one batch of blank wafers has to be processed to reach a state where chamber walls are coated again.

It might be expected that for these reasons certain diagnostic methods will be integrated in industrial processes which

- are an indicator whether the chamber is operating properly or whether a clean cycle is required,
- check whether the process parameters are inside the specified tolerance margins,
- measure relevant process parameters and adjust the process timing according to the measured data.

At least, process monitoring can be expected to become standard during the next years, process control including feedback of measured quantities might be realised for future technology generations.

The enormous sensitivity of semiconductor plasma processes[2] is the reason why only a small selection of materials like aluminium, quartz or stainless steel are used for the construction of plasma equipment. While electrical probes could provide valuable information about the process conditions, their use is unacceptable in real applications as evaporated probe material could contaminate the process. However, diagnostic methods which are not invasive but make process monitoring possible have become more and more popular [16]. A very promising approach is the so-called Self Excited Electron Resonance Spectroscopy (SEERS), which measures the electron density and the elastic electron-neutral collision rate. It is based on harmonics generated by nonlinear effects in RF-sheaths [48],[47], [49], [101].

Another possibility to perform non invasive diagnostics [54] is Optical Emission Spectroscopy (OES). While the effort to obtain absolute or spatially resolved [25] information may be unacceptably high for a real process environment, a simplified version of OES can still provide valuable information. For example, in etch processes the light emission of materials which stem from the processed substrate can be used as an endpoint detection [38], [118].

Though non invasive methods (like OES, SEERS) are the only acceptable possibility to perform diagnostics in a highly sensitive process environment, they have the disadvantage of providing (line of sight or volume) averaged quantities, only. In order to interpret the results, knowledge e.g. about the electron density distribution inside the chamber is required. This underlines the close relation between diagnostics and modelling. For many diagnostic methods models are required in order to derive quantitative from raw data.

---

[2] Especially materials which could act as dopands are critical.

1.4 An introductory approach to plasma models

While the previous sections emphasised the need for a modelling of low pressure discharges, in the following an example will be given how such models can be implemented. As introduction a very simple model was chosen on purpose. The results as well as the limitations of such a simple approach will be discussed. This section is intended to give a general overview of particle based plasma models. The reader who is interested in details is referred to [13], [12].

As an introductory example let us consider an ensemble of electrons which move under the influence of an alternating electric field. This might happen in an inductively coupled plasma (ICP). Our goal is to understand the heating mechanisms of the setup.

It is well known that the so-called collisional heating [63] is an important heating mechanism for low pressure discharges. Electrons are accelerated in an alternating electric field and undergo collisions with neutral particles. Due to the mass ratio, in the case of elastic collisions the electron loses only a small fraction of its kinetic energy, which means that on average with each collision directed velocity (the electron drift velocity) is converted into randomly distributed velocity (thermal energy).

1.4.1 A simple Monte Carlo model

The most straightforward approach to study a plasma is to consider the discharge as an ensemble of charged particles which move under the influence of electric fields. The time evolution of the system can easily be calculated by solving the equation of motion for each particle. This so-called Monte Carlo (MC) approach has the advantage to be easy to code compared to mathematically more demanding algorithms which are based on continuum models and partial differential equations. The simplicity of the underlying algorithms in combination with the close relationship to the corresponding physical reality, is the reason why various authors used Monte Carlo based models for the simulation of low pressure plasmas [12], [13], [120], [106], [82] for a variety of different applications.

For simplicity, it will be assumed that the electric field of the test problem is time varying but constant in configuration space. It is be given by:

$$\vec{E}(t) = \vec{e}_x \cdot E \, \cos(\omega t). \tag{1.1}$$

The negative charge of the electrons is compensated by an equal amount of positive ions (quasineutrality) so that no space charge exists, and only the RF-field has to be considered.

In order to study the conductivity of the model problem, the transport of the carriers in the alternating field is going to be discussed. The angular frequency ω of the alternating field is assumed to be high enough so that the movement of the ions due to their mass can be neglected. Then the conductivity is only caused by the electrons.

In typical low pressure discharges the degree of ionisation will not exceed 10^{-3}. This means that the electrons are a minority compared to the number of neutral particles, and electrons will frequently undergo collisions, especially with neutral particles. To demonstrate this, we restrict ourselves to the noble gas argon, for which the corresponding cross sections are very well known from various theoretical and experimental works (c. f. Tbl. 4.3).

Now, all the parts can be assembled to give the simplest example of a low pressure plasma model. For each electron of the considered ensemble we have to solve the equation of motion:

$$\frac{d^2\vec{r}}{dt^2} = -\frac{e}{m_e}\,\vec{E}(t), \tag{1.2}$$

where e denotes the elementary charge and m_e the electron mass, and $\vec{r}$ the position of the electron in the configuration space. As the actual position is of minor interest, an alternative formulation of (1.2) introduces the electron's velocity

$$\vec{v} = \frac{d\vec{r}}{dt}.$$

The velocity change in time is then given by:

$$\frac{d\vec{v}}{dt} = -\frac{e}{m_e}\,\vec{E}(t). \tag{1.3}$$

We assumed that the electric field $\vec{E}$ has a non-vanishing component only in x-direction, so (1.3) can be reduced to give a scalar equation:

$$\frac{dv_x}{dt} = -\frac{e}{m_e}\,E\,\cos(t). \tag{1.4}$$

In order to formulate a computer implementation of the problem, a discretised version is required. A compromise between accuracy and simplicity is a trapezoidal integration rule:

$$v_x(t+\Delta t) = v_x(t) - \Delta t\,\frac{e}{m_e}\,E\,\cos(t+\frac{\Delta t}{2}). \tag{1.5}$$

Finally, collision processes have to be considered. The probability p_c that an electron hits a neutral particle while it travels a distance Δs is given by:

$$p_c = \Delta s \sigma(v) n_N, \tag{1.6}$$

where n_N is the volume density of the scatterers (in this case neutral argon atoms) and $\sigma(v)$ the velocity-dependent collision cross section. It has to be mentioned that (1.6) is only valid for sufficiently small values of Δs so that p_c is significantly smaller than unity. The corresponding time step Δt must therefore be chosen small enough to ensure that particles move less than their mean free path distance during one time step. At the first glance this looks like a restriction, but as we have to choose a time step which is much smaller than the RF-cycle, the probability of a collision during one time step becomes sufficiently small.

So far, we did not discuss the details of a collision. The electron might be scattered elastically and only lose a small fraction of its kinetic energy or it might cause an excitation or ionisation of the neutral particles (if it has sufficient kinetic energy). Such an inelastic collision consumes the corresponding kinetic energy and will slow down the electron.

In case of an elastic collision, the relative energy loss can be approximated by a simple textbook formula [95]:

$$\frac{\Delta E}{E} = \frac{2m_e}{m_N}\,(1-\cos(\chi))\,, \tag{1.7}$$

where m_N denotes the mass of the neutral scatterer, and χ is the angle between the initial direction of the electron and its direction after the scattering.

1.4.2 Results

The results presented in this section are based on the model described in Sect. 1.4.1. The time evolution of the ensemble of initially randomly distributed electrons was calculated over several hundred RF-cycles. After this time, the ensemble reached a periodic behaviour. This state will be called converged solution. Calculations were carried out for an argon discharge operating at a neutral gas pressure of $1\,\mathrm{Pa}$ and a temperature of $300\,\mathrm{K}$. An RF-frequency of $f_{RF} = 27\,\mathrm{MHz}$ and an amplitude of $E = 50\mathrm{V/m}$ was chosen according to the frequency which is widely used in plasma processing applications. As an initial condition of the ensemble a Maxwellian energy distribution with an electron temperature of $kT_e = 3\,\mathrm{eV}$ was used. The whole ensemble consisted of $2 \cdot 10^6$ electrons.

The intention was to study the oscillation of the electrons in the alternating electric field; so in Fig.1.2, the velocity of the electrons versus time is plotted for the first few RF-cycles. At first glance, the result does not look surprising. Both, the electric field and the electron velocity are sinusoidal, and a phase shift of approximately $\pi/2$ between field and velocity can be observed. With exception of the first cycle the electron velocity shows approximately periodic behaviour, but some statistic variations (for example, see the overshoot of velocity in RF-cycle 4) are also visible.

The simulation was started with a Maxwellian electron energy distribution function (EEDF). An arbitrary electron temperature of $kT_e = 3\,\mathrm{eV}$ had been chosen. It cannot be expected, that this start value is identical with the energy distribution of a converged simulation. Right from the beginning of the simulation, the average velocity of the electrons shows a periodic behaviour, no significant relaxation process occurs. There are two possible explanations for this unexpected periodicity:

- The average drift of the electrons reacts insensitive on changes of the EEDF.
- A change in the EEDF is such a slow process that an influence on the electron drift cannot be observed during the first few RF-cycles.

In order to demonstrate a change in the mean energy of the ensemble, the plot of the average kinetic energy during the first 25 RF-cycles is shown in Fig. 1.3 .

At the beginning of the simulation (during the first ten RF-cycles), the ensemble loses an amount of about 10 percent of its kinetic energy. The average energy reaches a minimum and then starts to increase slightly. The change in the mean energy is relatively small, i.e.

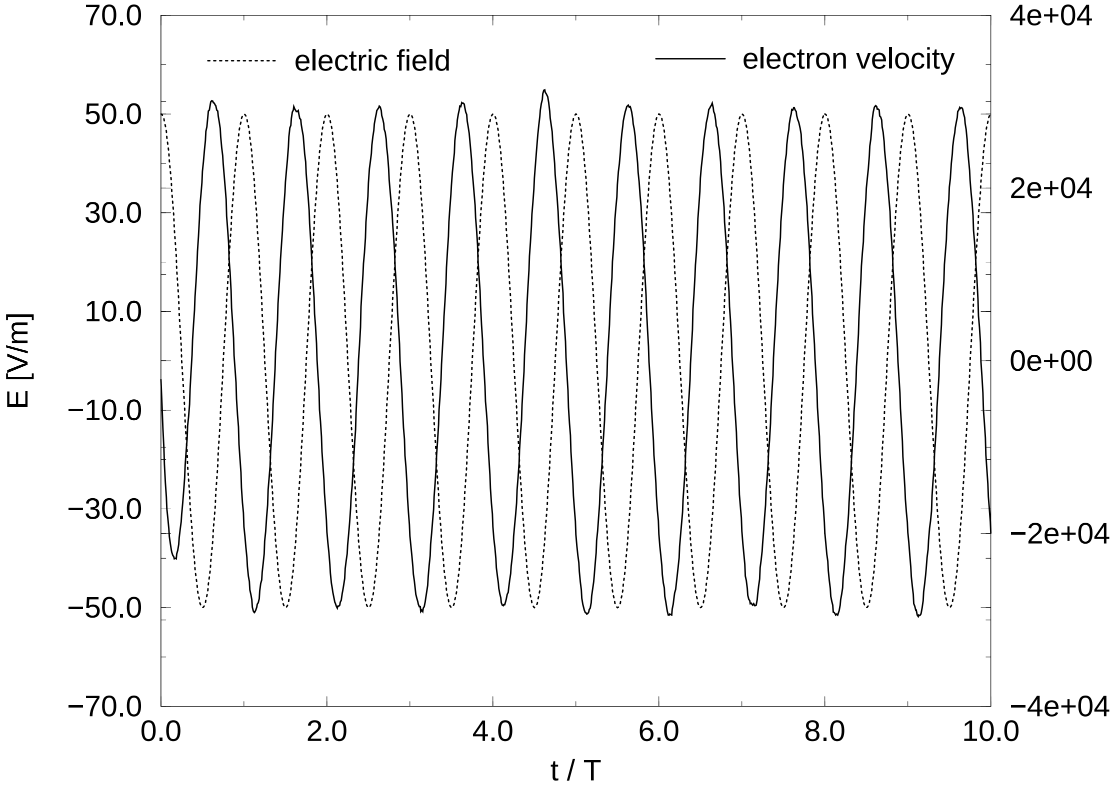

Figure 1.2: Electron velocity (full line, right axis) and electric field (dotted line, left axis) versus time for the first 10 RF-cycles. Results were calculated using a zero-dimensional Monte Carlo model for argon at 1 Pa and 300 K.

less than 10 percent of the start value. The reason for the energy loss during the first RF-cycles are collision processes. A Maxwellian electron energy distribution was used as a start distribution of the ensemble when the simulation was started. Compared with a converged solution, the Maxwellian distribution overestimates the number of electrons with energies above the ionisation and excitation threshold. Inelastic collisions like excitation and ionisation cause a loss of those high-energy electrons and cause a depletion in the high-energy region of the EEDF. After the first ten RF-cycles the high-energy part of the distribution is depleted. The change of the distribution function is shown in Fig. 1.4 in detail and will be discussed later.

The energy loss and the contribution of the different kinds of collision processes are also shown in Fig. 1.3 (logarithmic scale, right hand axis). The dominating energy loss mechanism are excitation processes. Ionisation causes a significant energy loss only right at the beginning of the simulation, where the high-energy region of the EEDF is still populated. The rapidly decreasing number of ionisation and excitation events indicates that the depletion is a fast process and that the time of ten RF-cycles is sufficiently long to reach a stable state.

The energy loss contributed by elastic collisions is mainly caused by the large number of slow electrons and therefore does not react sensitively on the depletion of the high-energy region

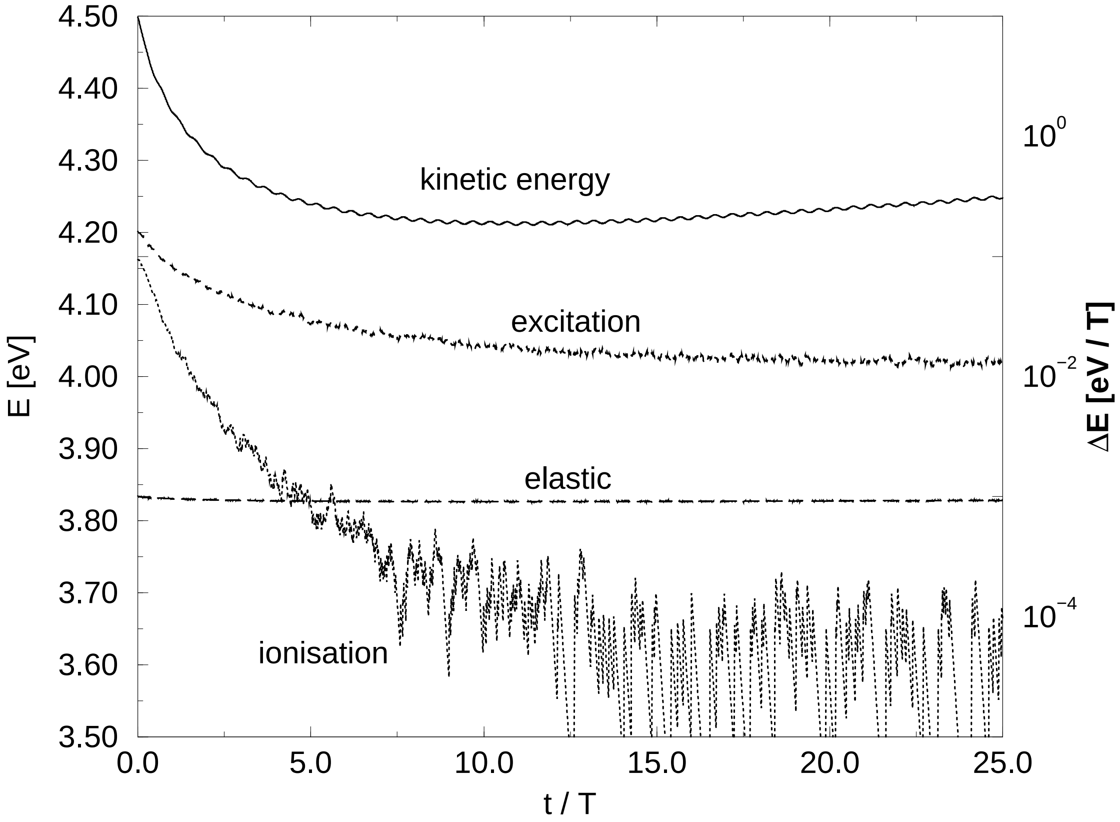

Figure 1.3: Averaged kinetic energy (linear scale, left hand axis) of the ensemble versus normalised time. The full line is the average kinetic energy of the ensemble. Dotted and dashed lines represent the energy loss ΔE per RF-cycle and electron due to elastic collisions, excitation and ionisation (logarithmic scale, right axis).

of the EEDF. Therefore, the elastic energy loss remains almost constant.

Another result shown in Fig. 1.3 is of interest: The change of average kinetic energy caused by the RF-oscillations (the periodic ripple) is less than one percent of the absolute value. This corresponds with a directed (drift) velocity of the electron which is much smaller than the average thermal velocity. The drift velocity of the electrons has a maximum value of $3 \cdot 10^4\,\mathrm{m/s}$ which is only a small fraction of the average thermal velocity $\overline{v_{th}} \approx 1.2 \cdot 10^6\,\mathrm{m/s}$. This means that the RF-field only causes a small modulation of the whole ensemble.

The change of the electron energy distribution function and its variation over the first few RF-cycles is shown in Fig. 1.4, where energy distributions are given at various simulation times. The simulation starts with a Maxwellian, i.e. linear distribution function on a logarithmic scale. Already after one RF-cycle, a significant part of the high-energy electrons vanished because they were scattered into the low energy part of the EEDF.

With increasing simulation time the high energy region depletes to form a Druyvesteyn like distribution function as it is also known from experiment. While this depletion process

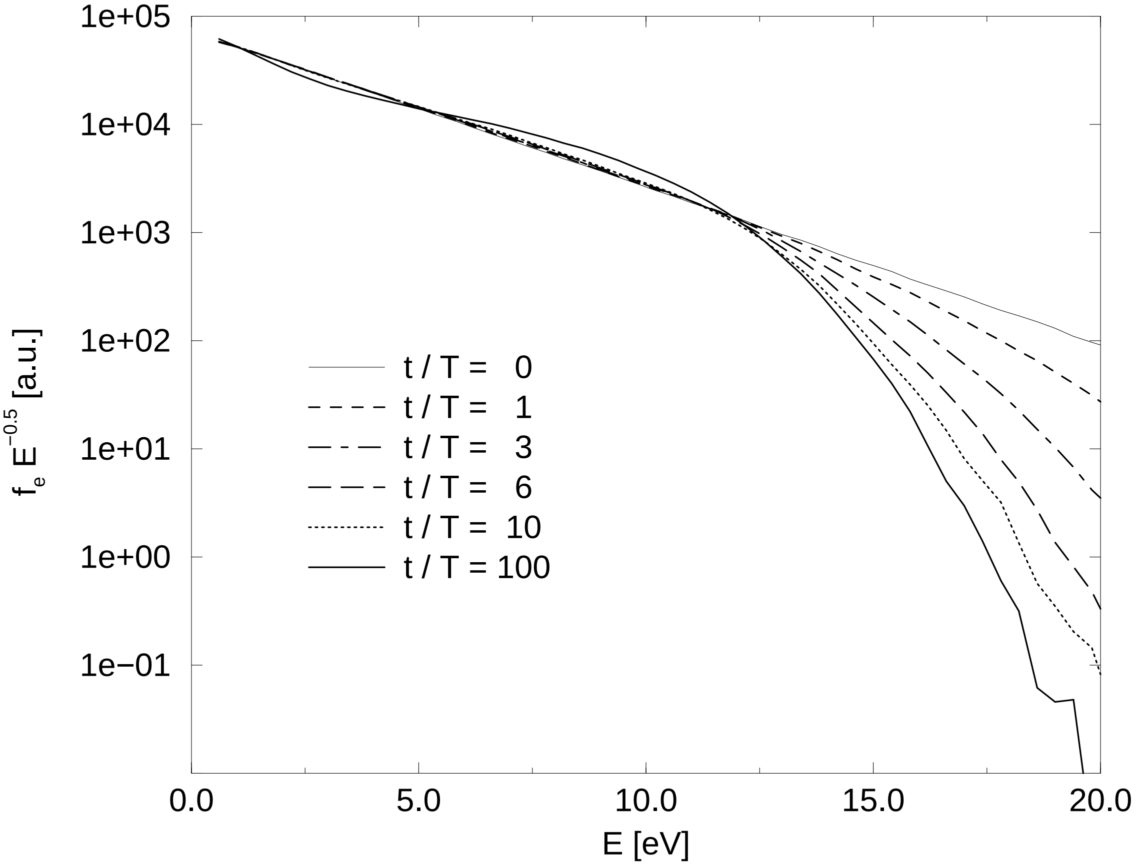

Figure 1.4: EEDFs for various simulation times.

is finished after ten RF-cycles, the whole system is not yet in equilibrium. A calculation over several hundred RF-cycles shows that a stable state is finally reached after approximately 100 cycles.

The overpopulation in the low energy region of the EEDF is characteristic for this final solution is ($E < 2\,\mathrm{eV}$). This overpopulation is caused by inelastic collisions (excitation, ionisation) which scatter fast electrons in a region of low energy. Measurements as well as calculations based on a numerical solution of the Boltzmann equation [51] show the same behaviour. Due to the pronounced Ramsauer minimum in the elastic scattering cross section of argon (c.f. Fig 4.4), a scattering of low-energy electrons is a rare process which means that slow electrons are trapped in the low-energy region, which corresponds with an overpopulation of the EEDF.

1.4.3 Discussion

The computationally simple approach to describe the movement of electrons in an alternating electric field by integrating the equation of motion for each particle revealed a surprising amount of results. Let us summarise the most important points:

- A relatively low peak amplitude of $E = 50\,\mathrm{V/m}$ ensures the heating of the ensemble.
- The drift of the electrons is almost negligible compared with the random movement.
- The most significant energy loss is caused by excitations. Elastic collisions and ionisation play a minor role.
- Starting from an idealised (Maxwellian) distribution, the EEDF is subjected to a rapid change during the first few RF-cycles, but it takes a number of several hundred RF-cycles to obtain a converged solution.
- The shape of the final EEDF with its characteristic depletion in the high-energy region and overpopulation in the low-energy region agrees qualitatively well with experimental data.
- To resolve statistically rare events like ionisation, a large number of simulation particles is necessary. Only a few electrons exist, which have sufficient energy to perform an ionisation. This correlates with the noise in high-energy regions of the EEDF which is typical for MC.
- The minority of highly energetic electrons does not have a significant influence on the average velocity of the whole ensemble. The conductivity of the ensemble is insensitive with respect to changes in the high energy region.
- This result can be generalised: Phenomena like drift or diffusion are dominated by the majority of particles with low energy, the so-called bulk of the EEDF. A bulk temperature might be introduced to provide a measure of the mean energy of those electrons.

On the other hand, the limitations of this simple approach have also become clear. An ensemble of $2 \cdot 10^6$ particles was necessary in order to get a reasonable resolution of the high-energy part of the EEDF and to get rid of excessive noise on all extracted signals. To reach a converged state, several hundred RF-cycles were necessary, each cycle had to be resolved by 100 steps which means that for the whole simulation 10^{10} times the equation of motion had to be solved.

The suggested model does not provide any spatial information, it is zero-dimensional. This approach might be justified for relatively large regions with a uniform electric field, but in order to understand real world applications, it would be desirable to have a two-dimensional model. As the computational effort for a zero dimensional case is already remarkably high, a generalisation to one or two dimensions will require an increase in the efficiency of the algorithm. However, during the last decades, users of Monte Carlo models have developed tools to increase the efficiency like the nullcollison method [96] or the particle splitting [37] in order to enhance the resolution in the high-energy regions of the EEDF.

Another problem is the noise caused by the underlying statistic processes like collisions. In the presented case, noisy signals are just a disfigurement, while in more complicated applications noise in distribution functions can cause real problems like self oscillations [13].

Sophisticated numerical techniques, like filtering in the frequency domain are then required to avoid such artefacts.

Chapter 2

Theory

The main advantages of Monte Carlo models are the comparably low effort for coding and the close relationship to the physical reality. On the other hand they have certain disadvantages. As they try to describe transport processes by directly solving the equation of motion for each single particle, it might take too long for calculating a converged solution, even for simple problems. In addition to the great demand for computing power, the statistical noise which is characteristic for MC calculations, can cause problems especially when coupled systems including Poisson's equation have to be solved. These are the main reasons why many authors dealing with plasma transport problems have chosen an approach based on partial differential equations rather than on a single kinetic description of particles.

In this chapter a model class based on the Boltzmann equation and its moments, the so-called hydrodynamic models will be derived and explained. Those models are also known in the literature as fluid dynamic models.

2.1 Hydrodynamic models

As the derivation of hydrodynamic or fluid models is always based on a number of simplifying assumptions, a great variety of similar, but nevertheless slightly different models exists which have been used in order to simulate transport processes in low pressure discharges. In most publications dealing with the application of hydrodynamic models the used equations are assumed to be valid without further explanation. Textbooks in which a thorough discussion and derivation of the model equations is performed like [95], [33] do not show results for realistic discharges.

It is the intention of the section to give a brief overview of the theoretical background of fluid dynamic models and the necessary assumptions. Starting from a very general approach, the main simplifications will be discussed especially with the aim to find an appropriate model system for low pressure plasmas.

2.1.1 The Boltzmann equation and its moments

Transport problems (including accelerating forces and collisions) can be treated by solving the fundamental equation dating back to Ludwig Boltzmann:

$$\frac{\partial f}{\partial t} + \vec{w} \cdot \frac{\partial f}{\partial \vec{r}} + \frac{q}{m} \left(\vec{E} + \vec{w} \times \vec{B} \right) \cdot \frac{\partial f}{\partial \vec{w}} = \left. \frac{\delta f}{\delta t} \right|_c \tag{2.1}$$

It describes the time evolution of the particle density $f(\vec{r}, \vec{w}, t)$ in the 6-dimensional configuration-velocity (phase) space. The particles are assumed to have the mass m and the charge q. Acceleration of charged particles by electric ($\vec{E}$) or magnetic ($\vec{B}$) fields is then given by $q/m \left(\vec{E} + \vec{w} \times \vec{B} \right)$. Generation or destruction of particles (by impact ionisation, recombination or chemical reactions) as well as collision processes are included in the collision operator $\left. \frac{\delta f}{\delta t} \right|_c$. For a detailed discussion and derivation of this equation see [18], for example.

A combination of the Boltzmann equation for each particle species with the Poisson's equation leads to the most rigorous description of low pressure plasmas from a physical point of view.

Unfortunately, finding a solution for the resulting system is only possible for simple test examples. The numerical effort for more general cases is too high to get solutions in an acceptable time using state of the art computers.

A way to reduce the six degrees of freedom is to multiply (2.1) with a set of test functions and to integrate over the velocity space. This operation leads to conservation equations known as the moments of the Boltzmann equation. A detailed discussion can be found in various textbooks [99], [33], [95], [63].

The advantage of this procedure is that in the most general case, there remain only the three spatial degrees of freedom. A solution of the so-called hydrodynamic equations can be calculated using an appropriate discretisation scheme. From the field of computational fluid dynamics various techniques (upwinding schemes) are known which are specially designed for hyperbolic transport equations [77], [55], [78].

While the use of a set of conservation equations makes it possible to get an approximated solution of the Boltzmann equation in an acceptable time, the method has certain disadvantages:

- A finite number of moment equations must be used. At some point the series has to be truncated. In order to do this, some assumptions about the distribution function in the velocity space must be made.
- A combination of the moment equations for a variety of different particle species can result in a system which is numerically stiff. It might be impossible or could take an unacceptable amount of time to find a solution.

In contrast to the technical problem to find a numerical solution, from a scientific point of view, the fact that assumptions about the distribution function have to be made, are the most serious drawback. Since collision cross sections for ionisation and excitation of heavy particles in the plasma have discrete threshold energies, they tend to influence the electron energy distribution (EEDF) strongly in energy regions close to the threshold energy.

The depletion in the high-energy tail of the distribution is qualitatively demonstrated in Sect. 1.4.1. A variety of theoretical as well as experimental works exists [109], [52], [17], [51], [8], where the deviation from a Maxwellian distribution is discussed for low pressure applications.

A typical Langmuir probe measurement demonstrating the non Maxwellian shape of an EEDF is shown in Fig. 2.1. The measurement was carried out in an argon discharge operating at a pressure of $0.1\,\mathrm{Pa}$. The figure shows the second derivative of the measured current-voltage characteristic. This quantity is directly proportional to the electron energy distribution function [105].

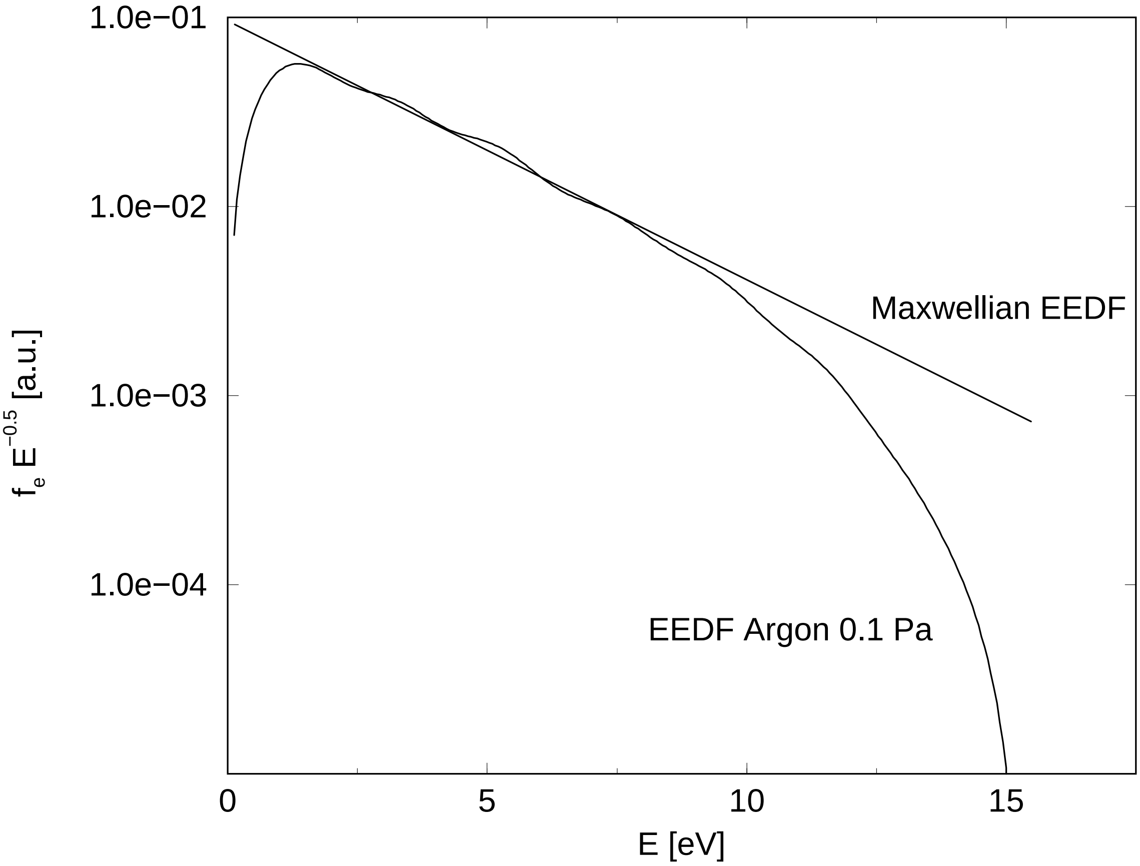

Figure 2.1: Electron energy distribution function measured by a Langmuir probe in a low pressure (0.1 Pa) argon discharge. For low energies the distribution function can be approximated by a Maxwellian (exponential) EEDF while for energies higher than 10 eV the measurement shows significant differences compared with the Maxwellian EEDF. This is due to a depletion of the tail of the EEDF caused by excitation and ionisation cross sections.

The obviously visible depletion in the high energy region demonstrates the limited range in which a Maxwellian energy distribution is an acceptable assumption. This illustrates an important point of criticism which might be raised against fluid dynamic models. Ionisation processes which are essential for the existence of the plasma only depend on the energy distribution of electrons over the ionisation threshold. On the other hand, the number of those energetic electrons is influenced by ionisation and excitation processes.

A common simplification is to neglect the depletion and to assume an Maxwellian energy distribution and a local electron temperature $T_e(\vec{r})$. This electron temperature can be calculated using an energy conservation equation. The effects of such a simplifying assumption will be discussed in the experimental section of this work.

Another approach to attack the problem of the unknown shape of EEDFs is the use of hybrid models, i.e. a combination of a fluid model with a Monte Carlo model [98], [28], [116]. As has been demonstrated in Sect. 1.4.1, the conductivity of the ensemble is dominated by the large number of low energy electrons. Generally, this is also valid for transport processes like diffusion or heat conduction. In order to describe these transport processes, the assumption of a Maxwellian EEDF might be sufficiently accurate. On the other hand, the rates for ionisation and excitation processes are crucially influenced by the typical depletion of the high energy tail of the EEDF. Information about this part can be obtained by Monte Carlo calculations or the approximate direct solution of the Boltzmann equation.

Conservation equations for mass and momentum have already been used in pioneering publications dealing with gaseous electronics, like [92] and [107]. The conservation laws, which can be derived from the Boltzmann equation by multiplying it with appropriate functions and integrating over the velocity space, have been known for many decades [19]. An application for charged species was demonstrated in [99]. Driven by technological advance and increasing computing power, a rapid development took part in the last decade where many calculations have been carried out in order to understand or optimise applications of industrial relevance. A general overview of the historic evolution of plasma models can be found in [56].

Models based on the moments of the Boltzmann equation are called fluid dynamic models. As the series of conservation equations can (theoretically) consist of an arbitrary number of equations for each species in the plasma, the question should be answered: How many equations are necessary? Furthermore, one has to decide how to close the series with an appropriate assumption of the energy distribution function. While the use of higher order approximations should lead to a more precise approximation of the physical reality, this has certain drawbacks.

The resulting system could be numerically unstable or it might be difficult to find an assumption of the distribution function to close the series of equations. Besides, for each equation an integral over the collision term has to be evaluated. This change of mass, momentum, energy etc must be known for each species.

For most applications, a reasonable compromise between effort and accuracy is a model consisting of not more than three conservation equations. Comparative studies of glow discharges are given in [43], [62] or [74], for example.

2.1.2 Conservation of mass

The integration of (2.1) over the velocity space without a weighting function leads directly to the conservation of mass:

$$\frac{\partial n}{\partial t} + \nabla \cdot (n\vec{v}) = G - R. \tag{2.2}$$

Here $n = n(\vec{r}, t)$ denotes the particle density per volume which can be obtained from $f(\vec{r}, \vec{w}, t)$ by integration over the velocity space:

$$n(\vec{r}, t) = \iiint\limits_{-\infty}^{+\infty} f(\vec{r}, \vec{w}, t)\, dw_x dw_y dw_z. \tag{2.3}$$

The average drift velocity of the particles $v(\vec{r}, t)$ can be calculated by multiplying f with $\vec{w}$ and integrating over the whole velocity space:

$$v(\vec{r}, t) = \frac{1}{n(\vec{r}, t)} \iiint\limits_{-\infty}^{+\infty} \vec{w}\, f(\vec{r}, \vec{w}, t)\, dw_x dw_y dw_z. \tag{2.4}$$

The generation or destruction of particles by impact ionisation, recombination or chemical reactions are given by $G - R$. Here G represents all the processes that lead to a generation while R is the particle loss.

2.1.3 Conservation of momentum

In a similar way, a conservation equation for momentum can be derived. Again (2.1) is multiplied with a weight function, in this case a product of the particle mass m and the velocity vector $\vec{w}$. In the following, the influence of magnetic fields will be neglected. The integration over the whole velocity space then gives:

$$\frac{\partial}{\partial t}\,(nm\vec{v}) + \nabla \cdot \mathbf{\Psi} - qn\vec{E} = \iiint\limits_{-\infty}^{+\infty} m\vec{w}\, \left.\frac{\delta f}{\delta t}\right|_c dw_x dw_y dw_z. \tag{2.5}$$

A change in momentum is caused either by diffusion processes given by the divergence of the pressure tensor $\mathbf{\Psi}$, by the acceleration in the electric field $\vec{E}$ or by collision processes. The components of the pressure tensor $\mathbf{\Psi}$ might be calculated carrying out the following integration over the whole velocity space:

$$\Psi_{ij} = \iiint\limits_{-\infty}^{+\infty} m f w_i w_j\, dw_x dw_y dw_z. \tag{2.6}$$

In this general form the drift of the particles with the mean velocity $\vec{v}$ is considered as well as their random movement. In order to separate the drift from the random movement, the velocity $\vec{w}$ might be divided into a sum of average velocity $\vec{v}$ and thermal velocity $\vec{u}$:

$$\vec{w} = \vec{v} + \vec{u},$$

and the components of $\mathbf{\Psi}$ take the form

$$\Psi_{ij} = mnv_iv_j + m \iiint\limits_{-\infty}^{+\infty} f(\vec{u}+\vec{v})u_iu_j \, du_xdu_ydu_z. \tag{2.7}$$

In cases in which the distribution function is isotropic, in (2.7) the integral over the random velocity has only non vanishing values in its trace. If the ensemble of particles has a non-zero drift velocity $\vec{v}$, an isotropic distribution function can be used, which is is centred around $\vec{v}$:

$$f(\vec{r},\vec{w},t) = f_0(\vec{r},|\vec{w}-\vec{v}|,t) = f_0(\vec{r},|\vec{u}|,t). \tag{2.8}$$

Due to symmetry considerations the off-trace components vanish and all the components on the trace take the same value. A local particle temperature $T(\vec{r},t)$ can be defined so that the mean random kinetic energy of all particles at the same location can be expressed by T:

$$\frac{1}{n}\iiint\limits_{-\infty}^{+\infty} \frac{m\,|\vec{u}|^2}{2} f_0(\vec{r},|\vec{u}|,t) \, du_xdu_ydu_z =: \frac{3}{2}kT(\vec{r},t). \tag{2.9}$$

With this definition the integral expression in (2.7) takes the form:

$$\Psi_{ij} = mnv_iv_j + \delta_{ij}nkT, \tag{2.10}$$

where δ_{ij} is the Kronecker symbol. In addition, a scalar partial pressure p can be defined by

$$p = nkT, \tag{2.11}$$

which leads us finally to the following form of the conservation of momentum:

$$\frac{\partial}{\partial t}\left(nm\vec{v}\right) + \nabla\cdot\left(nm\vec{v}\vec{v}\right) + \nabla p - qn\vec{E} = \iiint\limits_{-\infty}^{+\infty} m\vec{w} \left.\frac{\delta f}{\delta t}\right|_c dw_xdw_ydw_z. \tag{2.12}$$

At this point, it should be emphasised that the time derivative of the momentum $\partial mn\vec{v}/\partial t$ depends on the particle density n. It might be useful to eliminate the particle density in order to get an equation to describe the time evolution of the velocity $\vec{v}$ independently of the density n.

This can be achieved by some algebraic operations and the use of the conservation of mass, which leads to the following formulation:

$$nm\left(\frac{\partial\vec{v}}{\partial t} + \vec{v}\cdot\nabla\vec{v}\right) = qn\vec{E} - \nabla\left(nkT\right) - mn\vec{v}\left(G-R\right) - \iiint\limits_{-\infty}^{+\infty} m\vec{w} \left.\frac{\delta f}{\delta t}\right|_c dw_xdw_ydw_z. \tag{2.13}$$

2.1.4 Conservation of energy

The average kinetic energy ϵ of the particles is a scalar quantity and given by

$$\epsilon = \frac{1}{n} \iiint\limits_{-\infty}^{+\infty} \frac{m\,|\vec{w}|^2}{2} f(\vec{w})\, dw_x dw_y dw_z. \tag{2.14}$$

Using ϵ as a weight function and carrying out the integration of (2.1) over the whole velocity space, we can derive a conservation equation for the particle energy:

$$\frac{\partial(n\epsilon)}{\partial t} + \nabla \cdot \vec{\Gamma} = qn\vec{E}\vec{v} + P_h - P_c. \tag{2.15}$$

The time derivative of the energy per volume is given by the divergence of the energy flux $\vec{\Gamma}$ and the acceleration in the electric field $\vec{E}$. Heating terms are considered by P_h, the energy loss because of collisions by P_c.

In this formulation ϵ includes kinetic energy caused by the drift of the particles as well as by the random movement. A separation of energy ϵ_d associated with the drift of the particles and energy ϵ_r given by random movement might be useful:

$$\epsilon = \epsilon_d + \epsilon_r \quad \text{with} \quad \epsilon_d = \frac{m}{2}\,|\vec{v}|^2 \quad \text{and} \quad \epsilon_r = \frac{3}{2}kT. \tag{2.16}$$

The total energy flux vector $\vec{\Gamma}$ can then be expressed by

$$\vec{\Gamma} = \vec{q} + n\vec{v}\,(\epsilon_d + \epsilon_r) + m\psi\vec{v}, \tag{2.17}$$

where the vector $\vec{q}$ represents the heat flux given by

$$\vec{q} = \iiint\limits_{-\infty}^{+\infty} f(\vec{u})\vec{u}\ |\vec{u}|^2\ du_x du_y du_z, \tag{2.18}$$

and the pressure tensor ψ is defined by

$$\psi_{ij} = m \iiint\limits_{-\infty}^{+\infty} f(\vec{u} + \vec{v}) u_i u_j\ du_x du_y du_z. \tag{2.19}$$

In the case of an isotropic distribution function f, the pressure tensor ψ has only diagonal components which all have the same value nkT, and the heat flux vector $\vec{q}$ vanishes. Therefore the energy flux vector $\vec{\Gamma}$ finally takes the form:

$$\vec{\Gamma} = \frac{5}{2}nkT\vec{v} + n\epsilon_d\vec{v} \tag{2.20}$$

2.2 Application of hydrodynamic models for low pressure plasmas

The discussed conservation equations for mass, momentum, and energy are theoretically valid for all species which are present in a plasma discharge (electrons, ions and neutrals). Unfortunately, a direct implementation, especially for more dimensional problems, leads to numerical instabilities and an unacceptably high demand for computational power. Some authors report that discretisation schemes, well known from classical fluid dynamics, are not applicable to plasma simulations [7]. Therefore, it is desireable to find simplifications which reduce the numerical instabilities and/or the complexity of the problem.

One dimensional glow discharge simulations, which use three moments for electrons and two-moments for ions, have already been performed 10 years ago [71], [43]. For two-dimensional setups, it seems to be useful to neglect the momentum balance for electrons. The electron flux is directly calculated from the partial pressure gradient, the electric fields, and the electron mobility (drift diffusion approximation).

In the following part of this section the different possibilities for a complete set of model equations will be discussed. Especially, the case of inductively coupled discharges will be considered. The underlying simplifications and assumptions will be discussed.

2.2.1 General properties of low pressure plasma

The conservation equations for mass, momentum, and energy are valid in a very general sense. To assemble a stable and efficient model for low pressure discharges, it might be useful to consider some typical properties of low pressure plasmas.

Typically, low pressure discharges show a degree of ionisation in the range of 10^{-6} - 10^{-2}. Most particles in the discharge are neutral and only a small amount of charged particles exists. Nevertheless, the properties of this mixture of neutrals, electrons, and ions are crucially influenced by the presence of those charged species. Especially, chemical reactions like the production of free radicals is driven by energetic electrons. Also species can be produced which are chemically not stable. Another key feature is the low temperature of the neutral particles. Electric energy can be transferred to the electrons while the neutral gas remains almost cold. This is a key feature, being exploited in manufacturing microelectronics where substrate materials tend to be temperature sensitive. Last but not least, the anisotropic etching processes should be mentioned which essentially depend on the directed flux of positive ions towards surfaces. Modern integrated circuits containing high aspect ratio features like trench capacitors, as used for DRAM fabrication, are based on this effect.

While the properties of a low pressure plasma are determined by the presence of all kinds of charged carriers (electrons, positive and negative ions), it must be emphasised that the properties of electrons, positive ions, and negative ions are totally different.

When electric or magnetic RF-fields are applied, electrons are the charged species which is heated most effectively. The reason is their large ratio of charge to mass. In the discharge bulk the negative charge of the electrons in the plasma is approximately compensated by an equal amount of positive ions[1]. The ions in the plasma are not in thermal equilibrium with the electrons. Consider the following properties:

The mass ratio of $m_i/m_e = 1840$ for hydrogen ions and $m_i/m_e = 72700$ for argon ions.

---

[1] This is commonly known as quasineutrality. In the presence of negative ions this means that the charge density of positive and negative carriers locally adds to zero.

When we assume an average energy of electrons and ions in the same order of magnitude[2], the mean velocity of electrons is therefore much larger. The mass ratio is also the reason why electrons show a much higher mobility and contribution to the electrical conductivity of the plasma.

Electrons can be heated selectively, because an exchange of energy for the case of an elastic collision of an electron with a neutral atom or an ion is very inefficient due to the mass ratio. Collisions cause a deflection of the scattered electron but do not lead to a significant loss of energy. The opposite happens when the energy of the electron is sufficiently high to cause an excitation or ionisation. In this case the electron loses most of its kinetic energy.

As electrons on average are much faster than ions, statistically more electrons will be absorbed by the walls surrounding the plasma. This actually happens directly after the ignition of the discharge and leads to an accumulation of negative charge on the walls. In a steady state, electron and ion fluxes (time averaged) have to be equal. This is achieved by a coupling of the diffusion processes of fast electrons and slow ions. This mechanism is known as ambipolar diffusion, which means that an electrostatic potential exists which accelerates the diffusion of positive ions and slows down fast electrons in order to match the ion current. Electrons are confined by the potential, positive ions are driven. The potential well in which the electrons are confined causes a reflection of low energetic electrons and acts as an energy selective barrier. Electrons cannot leave the discharge before they acquired sufficient energy to overcome the potential barrier. Those electrons with less energy stay in the discharge and keep being reflected by the sheath regions.

Generally, ions might be considered to be the passive species of the plasma. The electric field in the whole plasma, including the sheath region, drives the transport of positive ions to the walls. Because ion mass is typically in the same order of magnitude as the mass of the corresponding neutral particles, they can very effectively exchange momentum by collision processes with neutrals (c.f. section 4.2).

The active species in the plasma are the electrons. They are responsible for ionisation processes in the bulk of the discharge. They are able to gain energy from externally applied electric and/or magnetic fields and to transfer this energy to the ions by the mechanism of ambipolar diffusion. The greatest part of the plasma's electrical conductivity is caused by the high mobility of the electrons.

The mentioned differences must be considered in an appropriate system of model equations. A physically rigorous model has to reflect the fundamental differences of electrons and ions. In the following, the mathematical and numerical aspects will be discussed.

2.2.2 Conservation of mass

The most fundamental conservation equation derived from (2.1) is the conservation equation of mass (2.2). It is valid for any species in the plasma and expresses the fact that matter cannot be destroyed or generated. However, processes like ionisation, dissociation or recombination force

---

[2] Under typical conditions, ion energy is even much smaller than electron energy as ions thermalize very effectively with the cold neutrals [63].

a particle to undergo transition from one species to another. These generating or destructive processes have to be considered.

In the following, the plasma is assumed to consist of neutrals, electrons, and positive ions. Multiple charged ions will be neglected. In the case of electrons and positive ions the conservation of mass reads:

$$\frac{\partial n_e}{\partial t} + \nabla \cdot (n_e \vec{v_e}) = G - R, \tag{2.21}$$

$$\frac{\partial n_i}{\partial t} + \nabla \cdot (n_i \vec{v_i}) = G - R. \tag{2.22}$$

Here, n_e, n_i denote electron and positive ion density, respectively, and $\vec{v_e}, \vec{v_i}$ the corresponding drift velocities. The generation of particles by impact ionisation produces an ion-electron pair which has to be considered in both of the conservation equations. The generation rate G is defined as the number of generated ion-electron pairs per time. In contrast to generation, recombination leads to a pairwise destruction of electrons and ions. A recombination rate R describes the particle loss per volume and time.

A conservation equation might also be used for neutral particles:

$$\frac{\partial n_N}{\partial t} + \nabla \cdot (n_N \vec{v}_N) = R - G. \tag{2.23}$$

Note that on the right hand side the term $R - G$ has the opposite sign to those in (2.21) and (2.22). Every generation of an ion-electron pair is a destruction and every recombination a production of a neutral particle.

The equations (2.21)-(2.23) describe the time evolution of a particle density. A change of density can be caused by a particle generation or destruction given by R and G and by a particle accumulation or depletion by transport processes given by $\nabla \cdot (n\vec{v})$. It is common to define a vector quantity $\vec{j} := n\vec{v}$ for the particle flux. Using this definition, (2.21), (2.22) read:

$$\frac{\partial n_e}{\partial t} + \nabla \cdot \vec{j_e} = G - R, \tag{2.24}$$

$$\frac{\partial n_i}{\partial t} + \nabla \cdot \vec{j_i} = G - R. \tag{2.25}$$

2.2.3 Conservation of momentum

The conservation equation for mass describes the time evolution of the particle density. It depends on the average particle drift velocity $\vec{v}$ defined in (2.4). The time evolution of this quantity is given by (2.5). Acceleration of charged particles by an electric field as well as diffusion caused by density gradients are considered. Knowledge of a tensor quantity $\mathbf{\Psi}$ describing the momentum flux would be required to evaluate this equation. A common simplification is to assume an isotropic energy distribution which causes the off-diagonal elements of $\mathbf{\Psi}$ to be zero. When we introduce a particle temperature T, the divergence of $\mathbf{\Psi}$ can be expressed as the gradient of the scalar partial pressure p given by $p = nkT$. Under these assumptions, and in the case of positive single charged ions equation (2.5) gives:

$$n_i m_i \left(\frac{\partial \vec{v_i}}{\partial t} + \vec{v_i} \cdot \nabla \vec{v_i} \right) = n_i e \vec{E} - \nabla \left(n_i k T_i \right) - \vec{P}_{mi} - n_i m_i \vec{v_i} (G - R). \tag{2.26}$$

As ions tend to thermalize effectively with neutrals by frequent charge exchange collisions, it might be assumed that the ion temperature is in the order of the neutral gas temperature. Therefore, for low pressure discharges, where the neutral gas temperature, is in the order of room temperature the influence of $\nabla \left(n_i k T_i \right)$ can often be neglected. The mentioned charge exchange collisions with neutrals represent the dominant term in $\vec{P}_{mi}$ which describes a loss of momentum. $\vec{P}_{mi}$ can be expressed as follows, assuming that the momentum loss is proportional to the ion drift velocity:

$$\vec{P}_{mi} = n_i m_i \vec{v_i} \nu_{mi}, \tag{2.27}$$

with ν_{mi} denoting the momentum loss frequency. As collisions become more frequent with increasing ion velocity, ν_{mi} has to be considered as velocity dependent. In Chapter 4 experimental data and approximate analytical expressions will be presented.

As already mentioned in Sect. 2.2.1, the situation for electrons turns out to be fundamentally different. Formally, the conservation of momentum is very similar to (2.26):

$$n_e m_e \left(\frac{\partial \vec{v_e}}{\partial t} + \vec{v_e} \cdot \nabla \vec{v_e} \right) = -n_e e \vec{E} - \nabla \left(n_e k T_e \right) - \vec{P}_{me} - n_e m_e \vec{v_e} (G - R). \tag{2.28}$$

The momentum loss by collisions again might be expressed by a product of mass, velocity and collision frequency:

$$\vec{P}_{me} = n_e m_e \vec{v_e} \nu_{me}. \tag{2.29}$$

Contrary to ions whose drift velocity normally exceeds their thermal velocity, electron drift velocities are typically much smaller than their thermal velocity (c.f Sect. 1.4). The momentum exchange frequency for electrons ν_{me} is an averaged value which generally depends on the density of the neutral particles, the corresponding momentum exchange cross section, and the EEDF. For details see Chapter 4.

Comparing the momentum conservation equations of ions (2.26) and of electrons (2.28), a few but important differences have to be discussed: As the electron mass is at least three orders of magnitude smaller than the ion mass, the left hand side of (2.28) becomes very small and might eventually be neglected. On the other hand, the product of the electron temperature T_e and the Boltzmann constant k is in the order of a few electron volts for typical low pressure discharges. Therefore, the $\nabla \left(n_e k T_e \right)$ term becomes one of the most important contributions to the right hand side. Please note that due to the negative charge of electrons, the sign of the term, which describes the influence of the electric field, is exactly the opposite of that in (2.26). This expresses the fact that electrons are retarded where ions are accelerated or vice versa.

(2.29) shows that the contribution of collisions is small because the collision term is proportional to the electron mass m_e. The discussion of the different contributions in (2.28) revealed the fact that only two terms, namely the gradient of the partial pressure $\nabla\left(n_e k T_e\right)$, and the momentum change in an electric field $-n_e e\vec{E}$ have a significant influence. Neglecting the left hand side as well as the term $n_e m_e \vec{v_e}(G-R)$ and re-arranging the resulting expression, we get:

$$n_e m_e \vec{v_e} \nu_{me} = -n_e e\vec{E} - \nabla\left(n_e k T_e\right), \tag{2.30}$$

wherefrom the electron flux can easily be calculated:

$$\vec{j_e} = n_e \vec{v_e} = \frac{-n_e e\vec{E} - \nabla\left(n_e k T_e\right)}{m_e \nu_{me}}. \tag{2.31}$$

This formula is known as the drift diffusion approximation of the electron flux. The electron flux is driven by an electric field (causing drift) and by a concentration gradient (causing diffusion). The replacment of the general expression (2.26) by (2.31) has numerical advantages. The drift diffusion approximation has been used in the field of semiconductor device simulation for decades and various numerical techniques have been developed to solve the resulting system. For a brief review see [5], [30].

It has to be emphasised that neglecting the left hand side of (2.28) might be an assumption which is not valid in all cases. In (2.31) the current vector is dependent on the local electric field and on the density and temperature gradient. This means that there is a local equilibrium of momentum gain and loss. As a consequence, particles cannot transport the momentum which they gained in one location to another location.

A comparison of both model approaches will be presented in Chapter 5 of this work . The important effects caused by electron inertia will be discussed in more detail there.

Recall that the drift diffusion model was derived by neglecting the inertia term in the momentum conservation equation. For electrons, due to their little mass, this assumption might be valid in a wide range of applications. In the case of ions, this can cause problems. However, many authors like [6], [35], [116], [65], [28] used the drift diffusion approach also for ions. In the plasma bulk drift-diffusion might be a good approximation, in the sheath regions it is definitely not, as especially in high density applications the sheath thickness is many times smaller than the ion mean free path. This means that collisions of ions and neutrals in the sheath are rare and most ions pass the sheath without a collision. The average velocity of ions is therefore mainly determined by the potential drop between the sheath edge and the actual position in the sheath. The use of the drift diffusion approximation would express the actual speed only as a function of the local electric field and the concentration gradient.

In other works a compromise of drift diffusion approximation and a full momentum conservation equation was chosen by the introduction of a so-called effective electric field [84], [65]. This approach considers inertia terms in those cases where the driving electric field shows variations in time, but does not properly describe the transport of momentum.

In the case of negative ions the situation is different. The electric field tends to concentrate negative ions in the bulk of the discharge, and their thermal energy is normally small compared to the voltage drop in sheath regions. A significant amount of negative ions exists only in the bulk of the discharge. The use of a drift diffusion model makes sense because the electric field is low enough in the bulk region.

2.2.4 Conservation of energy

As the discussion of the equation of motion (2.12) showed, the different specific properties of electrons and ions have to be considered in order to set up an appropriate model for low pressure discharges. In the case of energy transport, ions and electrons show fundamentally different behaviour, again.

Ions might be considered as the passive species of plasma, an electric field pointing from the plasma centre towards the walls forces them to leave the discharge. They thermalize effectively with the neutral gas background by charge exchange collisions. Due to their limited thermal energy, they cannot move in opposite direction of the electric field lines. Therefore, the energy as well as the momentum transport are only performed in the direction of the electric field. A good analogy in real life is a waterfall. Water coming from the top of the fall is accelerated by the force of gravity. The molecules are accelerated, but not heated, they eventually thermalize with the ambient air. Finally, at some point the waterfall hits the ground. A transport of matter and energy is only possible from top to bottom. Changing the level where the fall ends does not significantly affect the upper part of the fall.

During the discussion of (2.12) it was already shown that the effect of ion temperature may be neglected as the contribution of the ion temperature given by $\nabla n_i k T_i$ is small. The series of moments can be truncated after the equation of motion. A constant temperature, for example, equal to the neutral gas temperature is a possiblity. Using an energy conservation equation for positive ions in order to calculate a local ion temperature is possible but does not have significant influence on the equation of motion and does therefore not have any influence on the transport. For these reasons, a local ion temperature has not been considered in this work.

The situation is fundamentally different for electrons. They are the active species of the plasma and possess a high thermal velocity. The same potential distribution which accelerates the positive ions towards the walls causes a confinement of electrons. While an electron stays in the plasma, frequent reflections at the potential well occur. The thermal (random) movement exceeds the drift velocity and a transport of momentum is possible in any direction. When electrons are heated locally (for example in a magnetic RF field), they will be able to transfer this energy by heat conduction to other parts of the discharge. This transport of energy can be expressed in a general form using (2.15).

As the thermal (random) energy ϵ_r dominates the kinetic energy ϵ_d (associated with the drift energy) a simplified version of (2.15) can be used:

$$\frac{\partial(n\epsilon_r)}{\partial t} + \nabla \cdot \vec{\Gamma} = q n_e \vec{E} \vec{v} + P_h - P_c. \tag{2.32}$$

The corresponding heat flux vector $\vec{\Gamma}$ can be divided into a convective part and a heat flux which is driven by a temperature gradient:

$$\Gamma_e = \frac{5}{2}\vec{j}_e kT_e - \frac{5n_e kT_e}{2m_e\nu_{ee}}\nabla kT_e. \tag{2.33}$$

The collision frequency ν_{ee} between electrons and neutral particles determines the thermal conductivity and, therefore, the heat flux driven by a temperature gradient. As the underlying theory is beyond the scope of this work, for the derivation of (2.33) is referred to [95], [33].

It should be mentioned that in the case of low pressure, i.e. when the mean free path of electrons is at least in the order of the discharge dimension, the thermal conductivity becomes so large that no significant temperature differences exist in the discharge. In this case it is a good approximation to assume the electron temperature is constant. This does not only simplify the resulting system of coupled equations, but is also a possibility to model low pressure discharges, irrespective of the mode of heating. If the temperature in the plasma can be assumed to be constant, it does not matter where and how the plasma is heated. In this case, the model equation for a DC discharge, a CCP or an ICP are the same. The only remaining task is to find the eigenvalue of this constant electron temperature which corresponds to the geometry of the discharge. In the one-dimensional case this issue as well as the question of boundary conditions have been thoroughly discussed in [110], [112], [114] and [115].

2.3 Energy transfer to the plasma

2.3.1 Heating of the discharge

The existence of a technical plasma depends on the power which is coupled into the discharge. Energy transfer can be achieved by applying static or time varying electric fields. In the case the discharge is inductively driven, energy transfer is caused by an alternating current in a coil producing an induced electric field. Typically, the coil is mounted outside the actual discharge vessel, which means that the plasma does not come into contact with it. The discharge can be considered to be electrodeless.

The time varying magnetic field, resulting from a current in the antenna coil, causes induction of an electric field. Assuming an azimuthal symmetry of the setup, the field lines of this electric field are ring shaped and parallel to all the surfaces. This means that no RF-driven acceleration towards the boundaries of the discharge occurs like in capacitively coupled discharges. Therefore, the RF-current causes a heating of the plasma but does not attract charged particles towards the electrodes. Inductive discharges do not show self bias voltages and drastic acceleration of ions in the sheath regions as capacitive discharges do.

In direct comparison with CCPs, the concept of inductive coupling leads to electron densities which can be more than one order of magnitude higher for an equal input power and neutral gas pressure. However, the energy transfer to the plasma is limited when the plasma's electrical conductivity exceeds a certain level. The resulting eddy currents in the plasma will then induce a magnetic field in the opposite direction to the field of the coil. This limits the energy transfer to the plasma and is known as the skin effect.

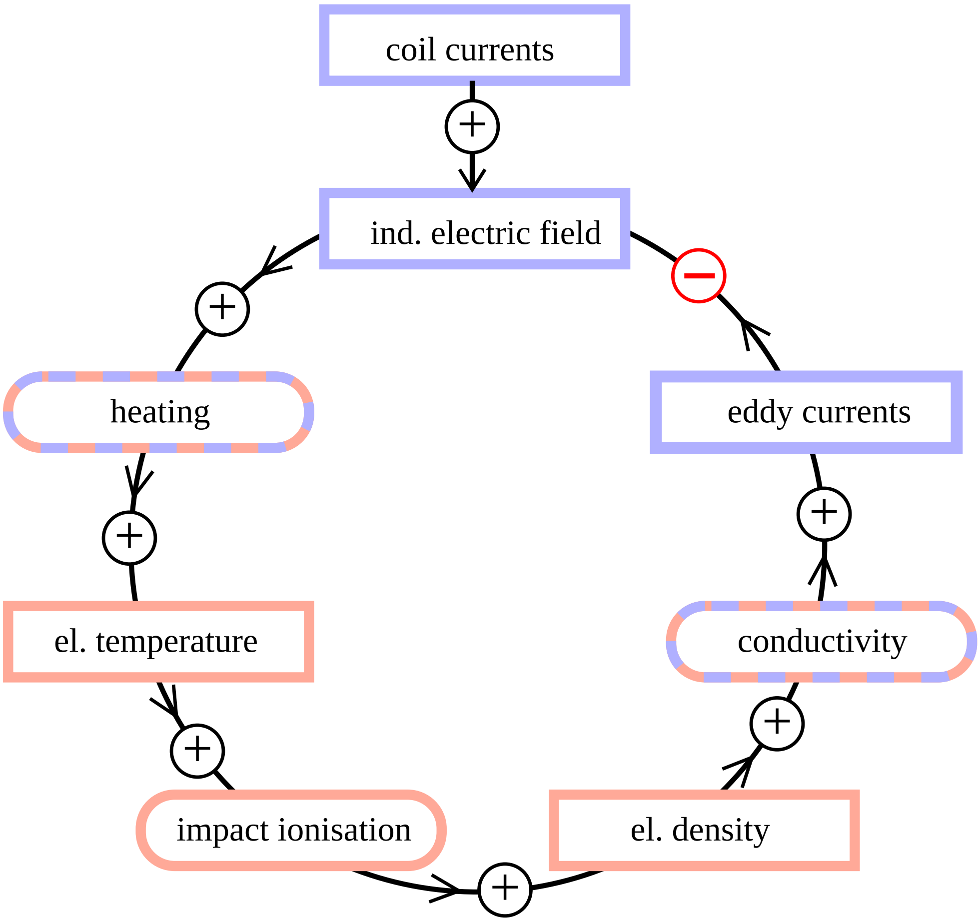

Figure 2.2: Energy flux diagram of ICPs.

The mentioned mechanism is shown in Fig. 2.2 in a schematic way. Power is transferred to the plasma by a coil current which induces an electric field. The electric field causes a heating of the electrons in the discharge and an increase of the electron temperature. This enhances the production of electron-ion pairs by impact ionisation. The electron density rises and leads to a higher electrical conductivity. The eddy currents increase and this finally causes a reduction of the net induced electric field in the discharge. At this point the loop is closed, the energy transfer to the plasma is reduced. Finally, the discharge reaches an equilibrium in which density and temperature remain constant.

Another important detail can be understood by the application of this very general model: Experimental evidence indicates, that under typical process conditions, the density distribution in ICP discharges remains constant once the discharge has reached a stable state [3]. A constant

---

[3] Long time probe measurements prove that electron density can keep changing during the first minutes of the discharge operation. This indicates that thermal time constants can have significant influence on discharge parameters. It is also known[45] that in the presence of negative ions and under certain operating conditions, discharges can show a permanently unstable behaviour. For further considerations such cases are going to be neglected.

electron density distribution only can exist when the generation of electron-ion pairs by electron impact ionisation is exactly balanced by the transport processes, which transfer the charged particles to the walls[4]. The assumption of stability, i.e. a not time varying state, implicitly determines the volume generation of electron-ion pairs and therefore the electron temperature. Under idealised conditions one might assume the existence of one eigenvalue of the electron temperature. This problem will be discussed in detail in Sect. 5.1.2.

2.3.2 Electrodynamic model

While the previous chapter dealt with the heating in a very general way, an appropriate electrodynamic model for inductively coupled discharges must express the heating of the plasma in dependence of the geometry parameters and the coil currents. Fig. 2.3 shows a schematic sectional drawing of an inductively coupled discharge.

The ICP discharge consists of a reactor chamber, in this example made of stainless steel (D), a dielectric window (B), and a set of coils (E). To prevent radiation of RF to the environment, a shielding (F) is mounted above the coils. This shielding can be assumed to be perfectly conducting, and it serves as the outer boundary of a simulation domain. The permeability of all materials can be assumed to be that of the free space μ_0.

An alternating current $\vec{j}_{ext}$ in the coils which is driven by an external RF-generator induces a time varying magnetic field in the discharge chamber. The resulting induced electric field heats the plasma. In order to calculate the value of the electric field, the conductivity of the different materials has to be considered. The calculation of the field distribution can be significantly simplified when the whole setup is considered to be rotational symmetric. We therefore neglect the influence of the connections between the ring-shaped coils and the RF-power supply.

An electrodynamic model can be derived from Maxwell's equations. The starting point are Ampere's law and Faraday's law:

$$\nabla \times \vec{E} = -\frac{\partial \vec{B}}{\partial t}, \tag{2.34}$$

$$\nabla \times \vec{H} = \vec{j} + \frac{\partial \vec{D}}{\partial t}. \tag{2.35}$$

Assuming time-harmonic dependence for all quantities of the form $\exp(i\omega t)$, the time derivatives can be replaced by multiplication with a factor of $i\omega$. Using the constitutive relations $\vec{D} = \epsilon_r \epsilon_0 \vec{E}$ and $\vec{B} = \mu_0 \vec{H}$, one gets from the equations (2.34), (2.35):

$$\nabla \times \underline{\vec{E}} = -i\omega \underline{\vec{B}}, \tag{2.36}$$

$$\nabla \times \frac{1}{\mu_0} \underline{\vec{B}} = \underline{\vec{j}} + i\omega \epsilon_r \epsilon_0 \underline{\vec{E}}. \tag{2.37}$$

---

[4] For typical low pressure plasmas volume recombination of positive ions and electrons can be neglected.

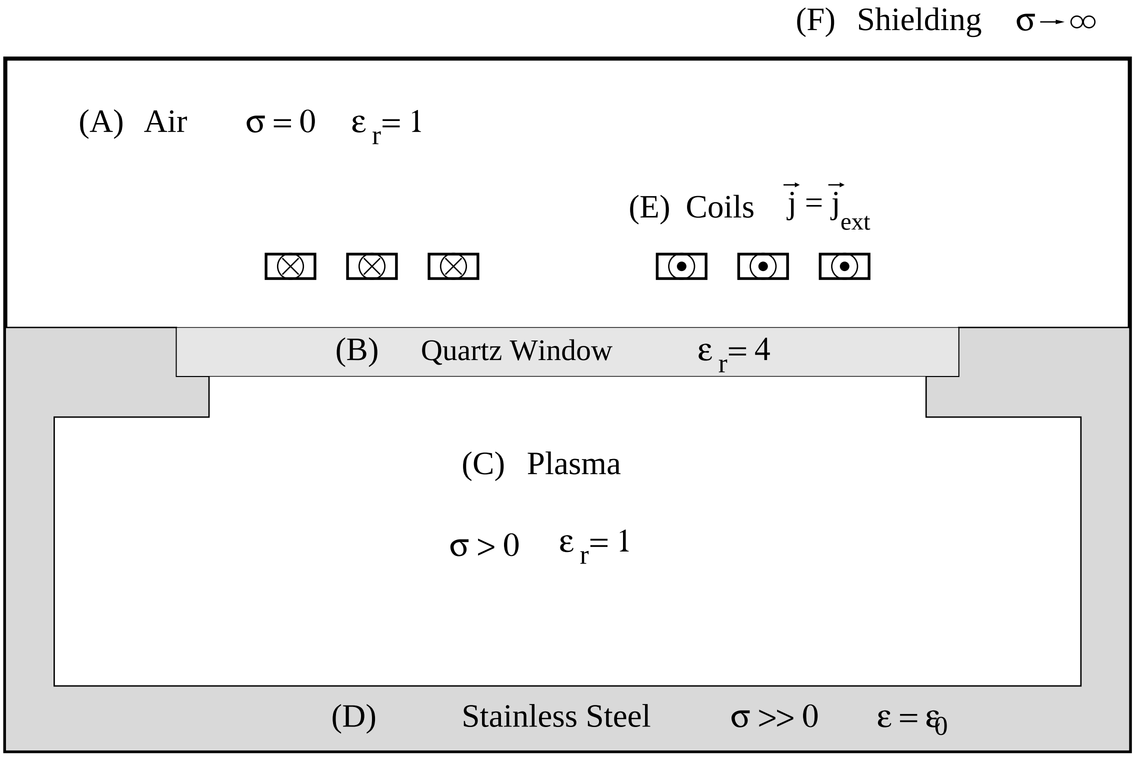

Figure 2.3: Simplified sectional drawing of an ICP discharge. The simulation domain can be divided into areas with different properties: (A) region outside the discharge, $\sigma = 0$. (B) dielectric window made of quartz glass, nonconducting $\epsilon_r \approx 4$, $\sigma = 0$. (C) discharge volume filled with plasma. $\epsilon_r = 1$, $\sigma > 0$. (D) discharge chamber made of stainless steel, $\epsilon_r = 1$, $\sigma \gg 0$. (E) coils, $\vec{j} = \vec{j}_{ext}$. (F) Shielding $\sigma \longrightarrow \infty$

By some algebraic operations, a differential equation for the electric field $\underline{\vec{E}}$ can be derived, combining (2.36) and (2.37):

$$\nabla\nabla \cdot \underline{\vec{E}} - \Delta\underline{\vec{E}} = -i\omega\mu_0 \left(\underline{\vec{j}} + i\omega\epsilon_r\epsilon_0\underline{\vec{E}}\right). \tag{2.38}$$

If no space charge exists, Coulomb's law reads:

$$\nabla \cdot \underline{\vec{E}} = 0. \tag{2.39}$$

The plasma might be considered as quasi neutral, therefore the term $\nabla\nabla \cdot \underline{\vec{E}}$ vanishes. Using the vacuum speed of light $c_0 = (\epsilon_0\mu_0)^{-1/2}$, (2.38) takes the form:

$$\Delta\underline{\vec{E}} + \frac{\epsilon_r\omega^2}{c_0^2} = i\omega\mu_0\underline{\vec{j}}. \tag{2.40}$$

So far, no simplifying assumptions were made except that the existence of space charge was neglected, and that all the time dependent quantities vary with the frequency ω. The case of sheath regions, where a space charge exists, will be discussed in Sect. 2.3.3.

Before an actual solution of (2.40) can be calculated, a few more manipulations are necessary. It is a common approach to introduce a complex conductivity $\underline{\sigma}$ in order to express the current density $\underline{\vec{j}}$ by the electric field $\underline{\vec{E}}$:

$$\underline{\vec{j}} = \underline{\sigma}\underline{\vec{E}}. \tag{2.41}$$

In the plasma the electrons' inertia causes a phase shift between the electric field and the electron current. The phase shift depends on the RF-frequency and on the number of collisions, which cause a deflection of the electrons. Various textbooks describe this in detail, e.g. [95]. In the plasma region a complex conductivity

$$\underline{\sigma} = \frac{n_e e^2}{m_e\left(\nu_{me} + i\omega\right)} \tag{2.42}$$

can be defined, which includes the phase shift caused by an elastic electronic-neutral collision rate ν_{me}. Different authors describing the heating of inductive discharges [44] used this approximation for the plasma conductivity while in other works it was pointed out that in a certain range of parameters more effort has to be spent [64]. A more sophisticated conductivity model will be discussed in Sect. 4.3.1 in detail.

Using equation (2.41), for most parts of the simulation domain an equation can be derived from (2.40), which only contains $\underline{\vec{E}}$. Only the coil region is problematic. However, this problem can be solved by introducing an externally driven coil current. Therefore, $\underline{\sigma}$ is set to zero in the coil region and a source term $\underline{\vec{j}}_{ext}$ for externally driven currents is included. This finally leads to:

$$\Delta\underline{\vec{E}} + \left(\frac{\epsilon_r\omega^2}{c_0^2} - i\omega\mu_0\underline{\sigma}\right)\underline{\vec{E}} = i\omega\mu_0\underline{\vec{j}}_{ext}. \tag{2.43}$$

This differential equation for the electric field $\underline{\vec{E}}$ might be interpreted as a wave equation

$$\Delta\underline{\vec{E}} + \underline{k}^2\underline{\vec{E}} = i\omega\mu_0\underline{\vec{j}}_{ext} \tag{2.44}$$

with

$$\underline{k}^2 = \varepsilon_r\frac{\omega^2}{c_0^2} - i\omega\mu_0\underline{\sigma}. \tag{2.45}$$

In order to solve it, appropriate boundary conditions are required. We have to consider regions (see Fig. 2.3) with different material properties:

- (A) air: $\sigma = 0$, $\epsilon_r = 1$.
- (B) quartz window: $\sigma = 0$, $\epsilon_r \approx 4$.
- (C) plasma: $|\underline{\sigma}| > 0$, $\epsilon_r = 1$.

- (D) conducting wall: $\sigma >> 0$, $\epsilon_r = 1$.
- (E) coils: $\vec{j} = \vec{j}_{ext}$.
- (F) shielding: $\sigma \longrightarrow \infty$.

Assuming an azimuthal symmetry of the problem, only the azimuthal component E_Θ of the electric RF-field has a nonzero value. The resulting scalar differential equation for the RF-field then reads:

$$\Delta \underline{E}_\Theta + \underline{k}^2 \underline{E}_\Theta = i\omega\mu_0 \underline{j}_\Theta. \tag{2.46}$$

The main reason for developing an electrodynamic model of the plasma was to calculate the power transferred to the plasma by ohmic heating. The power P_h per volume transferred from the electric field is then given by:

$$P_h = \Re\left\{\underline{\sigma}\right\} \left|\underline{E}_\Theta\right|^2. \tag{2.47}$$

2.3.3 RF-fields versus electrostatic fields

At this point a few summarising remarks can be helpful. Assuming azimuthal symmetry and sinusoidal time variations (angular frequency ω), a scalar equation (2.46) could be derived from which the azimuthal electric field $\underline{E}_\Theta$ can be calculated. The source for this electric field is an externally driven coil current distribution $\underline{j}_\Theta$. This current distribution has to be known and will in general be determined by the conductivity of the coils, the frequency ω, and the size of the coils (skin effect). However, in a sufficient distance from the coils the integral value has significant a influence rather than the distribution of the current. For example, a homogeneous current distribution might be used for the coil regions.

The reduction of the general wave equation (2.43) to a scalar equation (2.46) was based on the assumption of rotational symmetry. For real applications this is in many cases a good approximation and has obvious advantages. As mentioned before, the coil current $\underline{j}_\Theta$ as well as the resulting electric field $\underline{E}_\Theta$ are parallel to the walls of the discharge chamber. This means that acceleration of the electrons (or ions) in the RF-field is always parallel to the walls, too. This is a key feature of inductively driven (electrodeless) discharges. The RF-field causes no acceleration towards any electrode. Therefore, a decoupling of the RF-heating and the transport processes becomes possible.

While the time varying electric RF-field $\underline{E}_\Theta$ causes a periodic acceleration of charged particles in the Θ-direction, space charges will cause an (electrostatic) field in the r- and z-direction. In order to calculate this field, Poisson's equation can be used:

$$\Delta\Phi = \frac{e}{\varepsilon_0}(n_e - n_i). \tag{2.48}$$

The electrostatic field $\vec{E}$, which is related to the potential Φ, is given by:

$$\vec{E} = -\nabla\Phi. \tag{2.49}$$

Please note that $\vec{E}$ has real components and is in any case perpendicular to the RF induced complex electric field denoted by $\underline{E}_\Theta$. In a system model both fields can be calculated totally independently.

Chapter 3

Implementation

In the previous chapter, a system of equations describing the general time evolution of particle densities and velocities in a low pressure discharge was presented. For actually obtaining numerical solutions of this system, a discretisation strategy as well as the boundary conditions have to be known.

Furthermore, all collision processes leading to particle generation, recombination, change of particle momentum or energy have been discussed on a very general level, so far. In this chapter a discretisation strategy, especially designed for the conservative nature of the transport equations, will be presented. Also, important collision processes including ionisation, and elastic scattering of electrons, will be discussed in detail.

3.1 Application of hydrodynamic models

The applicability of conservation equations on low pressure plasma transport processes has already been recongnised in the pioneering works of Schottky [92] or Tonks and Langmuir [107]. But particularly since the numerical treatment of differential equations had become possible, numerous authors published works about low pressure plasmas. One of the early examples is the publication of Allen, Boyd, and Reynolds [1] which deals with the collection of positive ions by a negatively biased Langmuir probe. Many of the early works dealt especially with the development of theories describing electrical probes, in order to have an instrument with which quantitative plasma diagnostic could be performed. So Bernstein and Rabinowitz [11], who presented a more generalised ion collection theory assuming monoenergetic ions. Due to a further increase in available computing power in 1966, Laframboise [58] could calculate ion and electron currents under the assumption of a Maxwellian energy distribution. The reader who is interested in the development of probe models and their evolution is referred to the book of Swift and Schwar [105].

Parallel to the development of probe models, conservation equations were used to describe general transport processes in low pressure discharges. One of the early examples is the work of Self [94], published in 1967. This work and alter ones like [110] presented steady state results for electron and ion densities in positive columns of glow discharges.

The interest in hydrodynamic models increased with the industrial use of RF-discharges for semiconductor etching processes. Examples are the works of Graves [35], Boeuf [14] or Barnes, Colter and Elta [6]. The step from a steady state solution towards a dynamic problem did not only cause a higher demand of computational power. The question of numerical stability became important. Stable numerical techniques, well known from simulation of fluids, turned out not to be applicable for low pressure discharges [7]. Other approaches like staggered mesh discretisations [77] had to be developed. Another example is the use of discretisation techniques, as they are known from semiconductor device simulation [71]. For similarities and differences of the transport processes in semiconductor and low pressure plasma see Sect. 3.2.1.

In the case of dynamic models, the question of boundary conditions is not a trivial problem. The great variety of different possibilites proposed by different authors shows that no obvious optimum set of boundary conditions exists. For a more detailed discussion see Sect. 3.3.

The next step was the introduction of two-dimensional models in the early 1990s. Authors presenting calculations for capacitively driven RF-discharges were confronted with an enormous increase in the required computing time as well as with a number of additional problems:

- Sheath regions contribute significantly to the heating of the discharge. In order to understand the energy transfer to the plasma, these regions have to be resolved by the model.
- Electrons produced by secondary emission processes at electrodes are accelerated by sheath voltages of several ten volts. Due to their energy above the ionisation threshold, they cause a overproportionally high number of impact ionisations. A fluid description based on an average electron temperature might not be appropriate to describe this ability [104].

These problems led to the development of hybrid models, which combine a fluid description with Monte Carlo models for electron kinetics [117], [28], [70].

Parallel to more sophisticated models for capacitively driven discharges, high density plasma sources like ICPs were developed. Theoretical models were presented in the early 1990s in [117], [116], [102], [103]. Other publications focussed on heating mechanisms of the discharge, like [121], [41], [44], rather than on modelling the transport processes.

Due to the high electron and ion density in ICP sources, the sheath dimension is more than one order of magnitude smaller than in comparable CCP discharges. In none of the mentioned works the sheath region was actually resolved by the discretisation. Stewart et. al [102] were aware of this fact, but deliberately avoided a resolution of the sheath region. A possible workaround is the combination of an (analytic) sheath model [69] with a bulk model for the discharge [75]. The problem of plasma sheath transition is closely related to the discretisation strategy. Most of the authors who presented calculated results for ICP discharges used drift-diffusion models in order to describe the ion transport in the discharge. This is not surprising as a drift-diffusion approach is typically more stable and easier to implement than a combination of the mass and the momentum conservation equations. On the other hand, a reliable calculation of ion densities and energies in sheath regions has to consider the inertia of the ions. Comparing the development which took part in the 1980s with the advance in modelling of discharges in the 1990s it is remarkable that the authors who describe one-dimensional models like [6], [111], and [71] were very concerned about the validity of the used equations and an appropriate discretisation schemes. The authors of the 1990s who studied two-dimensional models appear to be less careful.

Parallel to the increasing complexity of the plasma transport models, the interest in plasma chemical processes increased. As technical applications typically use a mixture of different reactive or noble gases, it would be desirable to combine models describing the chemical reactions in the discharge with transport models for charged particles. A review of articles about plasma chemical models and possible combinations with particle transport models is given in [50]. In the recent years a large number of works was published dealing with modelling of plasma chemical processes. A few selected examples are [98] [68], [24], [20], [15]. With the increased computing power, the complexity caused by a large number of species is a minor problem compared with the question of the reliability of the used reaction rates as well as collision cross sections. An experimental validation of the (absolute) species concentrations in the discharge turns out to be a very demanding task [9], [3]. This is the reason why many publications only present theoretical results which remain without validation. The lack of experimental results is the reason for the fact that the state of the art in plasma modelling keeps changing rapidly. Frequently, effects which had not been considered so far turn out to be of crucial importance. Examples are the concentrations of the excited species [66], [73], the heating of the neutral gas at the discharge surfaces [61] or kinetic effects with influence on the discharge heating [93], [108].

3.2 Discretisation

3.2.1 Semiconductor models

Generally, the transport processes in a plasma, the drift and the diffusion of different charges are very similar to the transport processes in a semiconductor. As semiconductor device simulation is meanwhile a well-established tool, numerous methods have been investigated in order to find numerical solutions of the model equations. The equations used in semiconductor device simulation are also derived from the Boltzmann equation (2.1) and are almost identical to the conservation equations presented in Sect. 2.1.1. This similarity was recognised in works like [71], [14] or [76], where numerical techniques from device simulations were used to perform calculations for low pressure discharges. In this work, a discretisation is used which has been proposed and used for semiconductor device simulation. Algorithms developed for device simulation may also be applicable for low pressure discharges, but a few important differences between plasma and semiconductor should be underlined:

- In semiconductors only two charged species, electrons and holes exist. In plasmas numerous species of charged particles can exist.

- Electrons and holes in a semiconductor have effective masses which are in the same order of magnitude. In plasmas the mass of ions is at least three orders of magnitude larger than the electron mass.

- In semiconductors collisions with substrate atoms are very frequent due to the high density of the substrate material. This leads to a very short mean path length. In a plasma the collision rate depends on the pressure of the neutral gas background and might be as large as or even lager than the discharge geometry.
- The typical charge density in a semiconductor is much higher than in a plasma. Therefore, the space charge regions have very small geometric extensions (in the order of several microns). In capacitively coupled plasmas, the thickness of a space charge region can be in the order of centimetres.
- In semiconductors a recombination of carriers takes place also inside the device while in a low pressure plasma the process of volume recombination can often be neglected.

Due to these essential differences, especially, the resulting system of differential equations is much more stiff in the case of plasma simulation. The main reason is the mass ratio of electrons and ions, which causes the electron processes to be several orders of magnitudes faster than the ion processes. The used numerical schemes must be able to cope with this problem.

3.2.2 Finite box schemes

In order to perform a simulation of the transport processes (in computational fluid dynamics or semiconductor simulation), discretisation schemes known as finite volume schemes have widely been used. They are based on an integral formulation of the conservation equations which can easily be derived by applying the theorem of Gauss to the conservation equations [77]. As a result, the time variation of the conserved quantity in a control volume can be expressed by the flux across the surface of the control volume. A practical problem is to calculate the flux across the boundaries when the densities or the velocities are only known at discrete locations. The so-called finite box approach [30], which will be described in the following provides an elegant solution for this problem.

The simulation domain is divided into several volumes which are called finite boxes. A node is associated with each volume, and for each node quantities like the electron and the ion density, the velocities or the electric potential are considered to be known. The flux across the boundary of these boxes has to be calculated from the values of the physical quantities at the nodes. Fig. 3.1 illustrates how appropriate boxes can be constructed.

As each node is associated exactly with one box, the number of conservation equations equals the number of unknown variables. For boundary boxes the flux of the conserved quantity across the boundary has to be known. The question of boundary conditions will be discussed in detail, in the following section.

In order to illustrate the numerical scheme in detail let us consider the conservation of ion mass (2.22):

$$\frac{\partial n_i}{\partial t} + \nabla \cdot (n_i \vec{v_i}) = G - R. \tag{3.1}$$

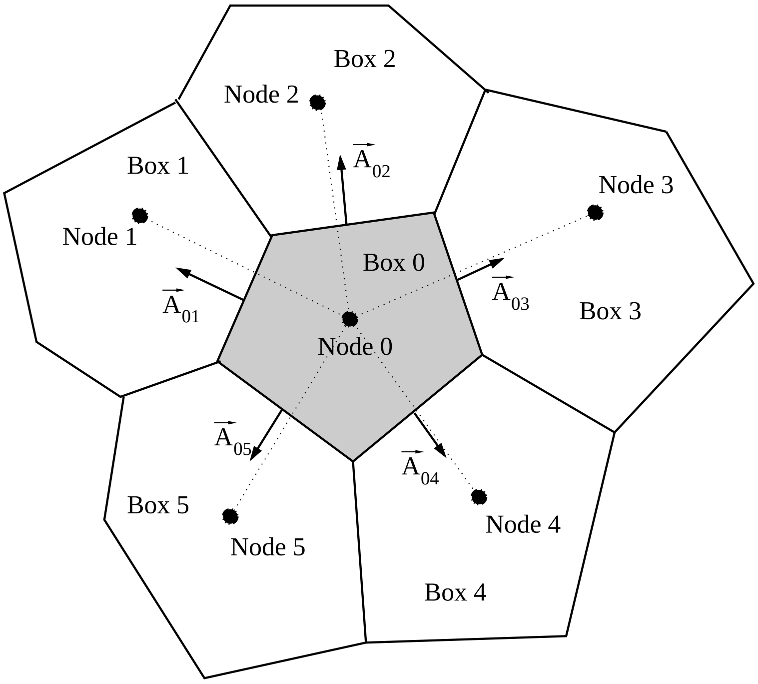

Figure 3.1: Finite box discretisation: The shaded area ”Box 0” represents a volume whose boundaries are defined by the normal bisectors to lines connecting the different nodes. The box is surrounded by its neighbouring boxes ”Box 1”-”Box 5”, whose geometry is defined by the same principle. The whole simulation domain can be decomposed into non overlapping boxes, by choosing appropriate locations for the nodes. Fluxes across boundaries can be approximated by the use of the physical quantities at the two nodes which are associated with every boundary of the box. For calculating fluxes vectors $\vec{A}_{01}$ - $\vec{A}_{05}$ are introduced, which are normal to the boundaries of ”Box 0” and represent the area of each boundary.

This equation is integrated over the volume of a finite box denoted as ”Box 0” as shown in Fig. 3.1. Using the theorem of Gauss, one obtains the weak formulation of the conservation equation:

$$\iiint\limits_{V_0} \frac{\partial n_i}{\partial t}\, dV + \iint\limits_{A_0} n_i \vec{v}_i \cdot d\vec{A} = \iiint\limits_{V_0} (G - R)\, dV. \tag{3.2}$$

Here V_0 is the volume of ”Box 0” and A_0 its surface. So far the differential form of (2.22) was only transformed to a weak formulation. To get a discretised version, we have to express the integrals by the node values of the physical quantities. The central node of the box is assumed to represent the average of all quantities inside the box, therefore the following approximations are used:

$$\iiint\limits_{V_0} \frac{\partial n_i}{\partial t}\, dV \approx V_0 \cdot \frac{\partial n_{i0}}{\partial t}, \tag{3.3}$$

$$\iiint\limits_{V_0} (G - R)\, dV \approx V_0\, (G_0 - R_0). \tag{3.4}$$

Note that all the quantities with index 0 represent the quantities located at ”Node 0”. To complete the discrete formulation, the surface integral of the particle flux has to be discretised. A set of surface vectors $\vec{A}_{01}$ - $\vec{A}_{05}$ is introduced (see Fig. 3.1).

These vectors are the outward pointing normals to all boundaries of ”Box 0”. The length of each vector is given by the area of each boundary. When we introduce the averaged fluxes $\vec{j}_{01}$ - $\vec{j}_{05}$ for all boundaries, the integral flux over all boundaries of ”Box 0” is:

$$\iint\limits_{A_0} n_i \vec{v}_i \cdot d\vec{A} = \sum_{k=1}^{5} \vec{A}_{0k} \cdot \vec{j}_{0k} \tag{3.5}$$

In a last step, the averaged fluxes across the different boundaries of a cell have to be expressed by the node values of n_i and $\vec{v}_i$. A simple possibility is to express the flux as the linear average of the flux at two neighbouring nodes:

$$\begin{aligned} \vec{j}_{01} &\approx \frac{1}{2} \left(\vec{v}_{i0} \cdot n_{i0} + \vec{v}_{i1} \cdot n_{i1} \right), \\ &\vdots \\ \vec{j}_{05} &\approx \frac{1}{2} \left(\vec{v}_{i0} \cdot n_{i0} + \vec{v}_{i5} \cdot n_{i5} \right). \end{aligned} \tag{3.6}$$

The advantage of the presented scheme is its easy implementation. Only the node values of all the variables, the neighbour nodes and the vectors representing the surface normals for each box boundary have to be known. Very general geometries and local refinement can be realised by this approach. On the other hand, the computational effort to calculate the appropriate locations for the different nodes (grid generation) may be significant.

In the case the grid is regular, the boxes have rectangular shape. With each box four neighbouring nodes are associated and the finite box scheme exactly provides the same approximation for the differential operators as a finite difference scheme does.

3.2.3 Upwind schemes

It has been known for decades that in the field of classical fluid dynamics numerical representations of hyperbolic systems tend to show numerical instabilities if they are not discretised in a proper way [77], [78], [55].

A common method to overcome these problems are the so-called “upwind schemes” [81] which use a discretisation (one sided spatial differences) in the opposite direction to the fluid flow. A mathematical analysis explaining the stability of upwind schemes e.g. can be found in

[100]. In order to apply the method to a finite volume discretisation, slight modifications are necessary. In the following, the basic idea of flux splitting algorithms will be explained and used to derive an efficient implementation for a finite volume discretisation.

A basic stability analysis for conservation equations is based on a vectorial notation of the system of equations. Let us assume that we want to carry out the analysis for the conservation of mass and momentum. Only one particle species shall be considered whose temperature is known. In a planar, one-dimensional case, the conservation equations for mass (2.2) and momentum (2.5) can be written in a vector notation:

$$\frac{\partial \mathbf{U}}{\partial t} + \frac{\partial \mathbf{F}}{\partial x} = \mathbf{S}. \tag{3.7}$$

Let us now introduce a density vector $\mathbf{U}$ and a flux vector $\mathbf{F}$, given by

$$\mathbf{U} = \begin{pmatrix} n \\ nv \end{pmatrix}, \quad \mathbf{F} = \begin{pmatrix} nv \\ nv^2 + nkT/m \end{pmatrix}, \tag{3.8}$$

as well as a vector $\mathbf{S}$, which includes the source terms for the mass and the momentum

$$\mathbf{S} = \begin{pmatrix} G - R \\ \frac{q}{m} nE - nv\nu \end{pmatrix}. \tag{3.9}$$

The partial pressure gradient which is on the right hand side of (2.5) is included in this formulation as part of the left hand side in the flux vector $\mathbf{F}$. In order to express the spatial derivative of the flux vector $\mathbf{F}$ by the spatial derivative of the density vector $\mathbf{U}$, a matrix $\mathbf{A}$ with the following property is introduced:

$$\frac{\partial \mathbf{F}}{\partial x} = \mathbf{A} \frac{\partial \mathbf{U}}{\partial x}. \tag{3.10}$$

In general, $\mathbf{A}$ will depend on $\mathbf{U}$ and can be calculated for the given example by taking the Jacobian of $\mathbf{F}$ with respect to $\mathbf{U}$:

$$\mathbf{A} = \frac{\partial \mathbf{F}}{\partial \mathbf{U}} = \begin{pmatrix} 0 & 1 \\ (kT/m - v^2) & 2v \end{pmatrix}. \tag{3.11}$$

The whole system now can be rewritten by

$$\frac{\partial \mathbf{U}}{\partial t} + \mathbf{A} \frac{\partial \mathbf{U}}{\partial x} = \mathbf{S}. \tag{3.12}$$

$\mathbf{A}$ might be diagonalised by means of it's eigenvalues and eigenvectors:

$$\mathbf{A} = \mathbf{Q \Lambda Q}^{-1} = \begin{pmatrix} 1 & 1 \\ (v + v_c) & (v - v_c) \end{pmatrix} \cdot \begin{pmatrix} v + v_c & 0 \\ 0 & v - v_c \end{pmatrix} \cdot \frac{1}{2v_c} \begin{pmatrix} (v_c - v) & 1 \\ (v + v_c) & -1 \end{pmatrix}, \tag{3.13}$$

where v_c represents the sound velocity given by

$$v_c = \sqrt{\frac{kT}{m}} \tag{3.14}$$

An elementary stability analysis as given in [100] shows that a corresponding finite difference representation is only stable when the direction of the one-sided spatial differences is chosen in dependence of the sign of the eigenvalues. For example, if we consider a region of supersonic flow ($v > v_c$), both eigenvalues $v + v_c$ as well as $v - v_c$ are positive. This means a finite difference scheme is stable if backward differences are used.

Assuming subsonic flow ($0 \leq v < v_c$), the matrix $\mathbf{\Lambda}$ contains one positive and one negative eigenvalue. In order to obtain a stable finite difference representation, a mixture of backward and forward differences is required. In [100] Steger and Warming propose to carry out a splitting of $\mathbf{\Lambda}$ into a matrix $\mathbf{\Lambda}^+$ which contains the positive eigenvalues and $\mathbf{\Lambda}^-$ which contains the negative eigenvalues. Unfortunately, such an approach tends to create numerical instabilities when a subsonic region and a supersonic region meet. That is the case, for example, in the sheath region of a capacitively driven plasma.

This problem can be overcome by a more general approach, i.e. a splitting of $\mathbf{\Lambda}$ into a sum of matrices which contain only positive and only negative values. Such a splitting is then described by:

$$\mathbf{\Lambda} = \mathbf{\Lambda}^+ + \mathbf{\Lambda}^- = \begin{pmatrix} \frac{1}{2}(v+v_c)+v_0 & 0 \\ 0 & \frac{1}{2}(v-v_c)+v_0 \end{pmatrix} + \begin{pmatrix} \frac{1}{2}(v+v_c)-v_0 & 0 \\ 0 & \frac{1}{2}(v-v_c)-v_0 \end{pmatrix}, \tag{3.15}$$

having introduced a parameter v_0, which has to satisfy the inequality

$$v_0 > \frac{1}{2}(|v| + v_c). \tag{3.16}$$

After inserting the splitting in (3.13), one is able to define the matrices $\mathbf{A}^+$ and $\mathbf{A}^-$, which are associated with $\mathbf{\Lambda}^+$ and $\mathbf{\Lambda}^-$:

$$\mathbf{A} = \mathbf{Q}\mathbf{\Lambda}\mathbf{Q}^{-1} = \mathbf{A} = \mathbf{Q}\left(\mathbf{\Lambda}^+ + \mathbf{\Lambda}^-\right)\mathbf{Q}^{-1} = \mathbf{A}^+ + \mathbf{A}^-. \tag{3.17}$$

Based on the splitting proposed in (3.15), this leads to

$$\mathbf{A}^+ = \begin{pmatrix} v_0 & \frac{1}{2} \\ \frac{1}{2}(v_c^2 - v^2) & v + v_0 \end{pmatrix} \quad \text{and} \quad \mathbf{A}^- = \begin{pmatrix} -v_0 & \frac{1}{2} \\ \frac{1}{2}(v_c^2 - v^2) & v - v_0 \end{pmatrix}. \tag{3.18}$$

A numerically stable scheme is now obtained when forward and backward differences are used in combination with the splitting of $\mathbf{A}$ in $\mathbf{A}^+$ and $\mathbf{A}^-$. For simplicity, let us assume a discretisation by equally spaced values which are located Δx from each other. When we use a fully implicit time discretisation and a time step Δt, the discretised version of (3.12) then takes the form:

$$\frac{1}{\Delta t}\left(\mathbf{U}_j^{n+1}-\mathbf{U}_j^n\right)+\frac{1}{\Delta x}\mathbf{A}^+\left(\mathbf{U}_j^{n+1}-\mathbf{U}_{j-1}^{n+1}\right)+\frac{1}{\Delta x}\mathbf{A}^-\left(\mathbf{U}_{j+1}^{n+1}-\mathbf{U}_j^{n+1}\right)=\mathbf{S}. \tag{3.19}$$

Here, j is the index denoting the position in space and n the index for the discretised time. The actual consequences of the splitting can be seen when the explicit expression for $\mathbf{U}$, $\mathbf{A}^+$ and $\mathbf{A}^-$ are used. Recall that the density vector $\mathbf{U}$ was defined by

$$\mathbf{U}=\left(\begin{array}{c} n \\ nv \end{array}\right)=:\left(\begin{array}{c} n \\ j \end{array}\right), \tag{3.20}$$

where $j=nv$ represents the particle flux. The splitting of (3.19) into two scalar equations leads to:

$$\begin{aligned}&\frac{1}{\Delta t}\left(n_j^{n+1}-n_j^n\right)+\frac{1}{\Delta x}\left(v_0\left(n_j^{n+1}-n_{j-1}^{n+1}\right)+\frac{1}{2}\left(j_j^{n+1}-j_{j-1}^{n+1}\right)\right)\\ &\quad+\frac{1}{\Delta x}\left(-v_0\left(n_{j+1}^{n+1}-n_j^{n+1}\right)+\frac{1}{2}\left(j_{j+1}^{n+1}-j_j^{n+1}\right)\right)=G-R,\end{aligned} \tag{3.21}$$

$$\begin{aligned}&\frac{1}{\Delta t}\left(j_j^{n+1}-j_j^n\right)\\ &+\frac{1}{\Delta x}\left(\frac{1}{2}\left(v_c^2-\left(v_j^{n+1}\right)^2\right)\left(n_j^{n+1}-n_{j-1}^{n+1}\right)+\left(v_j^{n+1}+v_0\right)\left(j_j^{n+1}-j_{j-1}^{n+1}\right)\right)\\ &+\frac{1}{\Delta x}\left(\frac{1}{2}\left(v_c^2-\left(v_j^{n+1}\right)^2\right)\left(n_{j+1}^{n+1}-n_j^{n+1}\right)+\left(v_j^{n+1}-v_0\right)\left(j_{j+1}^{n+1}-j_j^{n+1}\right)\right)\\ &=\frac{q}{m}nE-nv_j^{n+1}\nu.\end{aligned} \tag{3.22}$$

After the rearrangement of the terms in (3.21), the direct effect of the flux splitting becomes visible. The discrete form of the conservation of mass leads to:

$$\frac{1}{\Delta t}\left(n_j^{n+1}-n_j^n\right)+\frac{1}{2\Delta x}\left(j_{j+1}^{n+1}-j_{j-1}^{n+1}\right)-\frac{v_0}{\Delta x}\left(n_{j+1}^{n+1}-2n_j^{n+1}+n_{j-1}^{n+1}\right)=G-R. \tag{3.23}$$

While the second term on the left hand side represents a centred difference approximation of the spatial flux derivative, $-v_0/\Delta x\left(n_{j+1}^{n+1}-2n_j^{n+1}+n_{j-1}^{n+1}\right)$ could be understood as a finite difference approximation of the second derivative of the density, weighted with a factor of $-v_0\Delta x$. The quantity v_0, which had been introduced in order to guarantee the numerical stability of the algorithm, directly controls the influence of the second derivative. This represents the divergence of a diffusion driven flux with a diffusion constant of $v_0\Delta x$. This knowledge is useful, when a finite volume discretisation is discussed.

The effect that second derivatives can be used to stabilise numerical schemes for first order equations is well known and has been discussed thoroughly in the literature [55]. However, the underlying stability analysis in case of finite differences gives an indication how much numerical damping is necessary. The choice of an appropriate control parameter v_0 will be discussed later.

In a similar way the conservation of momentum (3.22) can be simplified:

$$\begin{aligned}
\frac{1}{\Delta t}\left(j_j^{n+1} - j_j^n\right) &+ \left(v_c^2 - \left(v_j^{n+1}\right)^2\right)\frac{1}{2\Delta x}\left(n_{j+1}^{n+1} - n_{j-1}^{n+1}\right) \\
&+ \frac{2v_j^{n+1}}{2\Delta x}\left(j_{j+1}^{n+1} - j_{j-1}^{n+1}\right) \\
&- \frac{v_0}{\Delta x}\left(j_{j-1}^{n+1} - 2j_j^{n+1} - j_{j-1}^{n+1}\right) = \frac{q}{m}nE - nv\nu. \qquad (3.24)
\end{aligned}$$

Like the conservation equation of mass (3.23), the conservation of momentum (3.24) contains the centred difference approximations of density and particle flux gradients corresponding to the differential form given in (2.5). Numerical viscosity or damping is introduced by a second derivative of the particle flux weighted with $-v_0\Delta x$.

The presented derivation was based on a finite difference discretisation, but the results given by (3.23) and (3.24) can easily be applied to finite volume schemes.

The question has to be answered, what value of v_0 will have to be chosen to achieve a compromise between numerical stability and the introduced numerical viscosity. The condition which limits the range from which v_0 can be chosen is given in (3.16). A possible choice for v_0 is:

$$v_0 = \sqrt{v_c^2 + v^2}. \qquad (3.25)$$

This is also the value of v_0 used for all the results presented in the following.

3.3 Boundary conditions

In order to find a unique solution for a complete system of hydrodynamic and electrodynamic equations, correct boundary conditions have to be stated. For the electrostatic potential and electric field boundary conditions are obvious. The situation for particle densities and velocities is more complicated. In this section the physical principles from which boundary conditions can be derived are discussed, as well as an overview which boundary conditions have been used by other authors is presented. Finally, a set of the conditions adapted to the chosen finite volume discretisation, which is used in this work will be proposed. Furthermore, a short review of the boundary conditions used by other authors in dependence of applied discretisations completes this section.

3.3.1 Electrodynamic model, Poisson equation

It is a relatively easy task to find the conditions for Poisson's equation and for the electrodynamic conservation equation, which describes the induced electric field in an ICP discharge. Good conductors are known to cause the induced electric field to vanish at their surface. Typically, ICP reactor chambers are built of conducting material or the whole setup is surrounded by a conducting outer shielding in order to prevent the radiation of RF. As a consequence for the electrodynamic model the condition $\underline{E}_\Theta = 0$ can be used implying that the simulation domain is bounded by a perfectly conducting surface.

Dirichlet boundary conditions can be used for the electrostatic potential Φ if the surface is electrically conducting. The potential on the whole surface is either set to zero for grounded walls or to the corresponding bias voltage in the case of an applied DC-bias voltage. A mixed boundary condition combining the surface charge and the potential and the local electric field is commonly used for insulating surfaces. For the electrostatic field $\vec{E}$ no boundary conditions are required because $\vec{E} = -\nabla\Phi$ is not an independent variable and can be calculated by differentiation from Φ.

3.3.2 A "simple" test problem

Generally, boundary conditions are required to select one and only one possibility from an infinite variety of correct solutions in the simulation domain. The criteria of this choice should reflect the physical reality. In typical low pressure discharges, most charged particles produced by ionisation (electrons or positive ions) after e certain time hit the wall, are absorbed by the surface and neutralised. Volume recombination as a particle sink often can be neglected. Wall recombination is the only process leading to a destruction of charged particles. Therefore, boundary conditions have to express the perfect absorption of incident particles.

The following "simple" test problem shows that the choice of physically meaningful boundary conditions in the case of transport problems is not necessarily a trivial task:

In a sheath region the potential drop repels almost all electrons. The only charges which are present are positive ions. Furthermore, the generation of charges in the sheath region shall be neglected, and only the stationary case is considered. The ion flux through the sheath can then be considered as constant and position independent i.e. $n_i(x)v_i(x) \equiv J_0$. The ions shall undergo no collisions, neither elastic nor inelastic, while passing the sheath. The ions are assumed to be monoenergetic and the local ion velocity is expressed directly by the local electric potential Φ:

$$v_i = \sqrt{-\frac{2e\Phi}{m_i}}. \tag{3.26}$$

These are the basic assumptions from which the well known Child-Langmuir law can be derived [63]. In the sheath region the electric potential has to fulfill the Poisson equation. This means in a one-dimensional case:

$$\frac{d^2\Phi}{dx^2} = -\frac{e}{\epsilon_0} n_i = \frac{J_0}{\sqrt{-\frac{2e\Phi}{m_i}}}. \tag{3.27}$$

An obvious solution for the potential Φ is proportional to $x^{\frac{4}{3}}$ which gives for the ion velocity and density in the sheath region:

$$v_i \sim x^{\frac{2}{3}}, \tag{3.28}$$

$$n_i \sim x^{-\frac{2}{3}}. \tag{3.29}$$

The assumptions under which this result was derived are obviously a drastic simplification of a realistic setup. Ion friction, for example, caused by charge exchange collisions was neglected. An ion velocity which is only determined by the local potential Φ is not realistic in any case. For time varying problems the assumption of a constant, time independent J_0 is also not acceptable. However, the space dependence of n_i and v_i reveals some interesting details:

The ion density decreases with increasing x, depending on the voltage drop in the sheath region. Even if the density drop might be quite large for large voltages across the sheath the density drops never down to zero, neither does the density gradient vanish. This result shows that at the location of the boundary the classical boundary condition types, like von Neumann or Dirichlet conditions, are not applicable. Nevertheless, a large number of authors who dealt with transport problems in low pressure plasmas used these boundary conditions.

3.3.3 Transport equations for ions

The simple example in the previous section illustrates the basic difficulty one is confronted with looking for physically meaningful boundary conditions for ions leaving the discharge. A simple choice like the assumption of a vanishing density or density gradient is obviously incorrect. The speed and the density at the location of the boundary are rather determined by the acceleration and the ion generation in the discharge volume than by the boundary itself which does hardly affect the volume processes. This is a typical situation for supersonic flow, i.e. when the ion drift velocity exceeds the sound speed given by $v_c = \sqrt{kT_i/m_i}$. Therefore, the question of boundary conditions is strongly related to the stability analysis of the transport equations discussed in the last section. Typically, in a large part of the discharge, thermal energies of ions are low in comparison with their large drift velocities. Subsonic parts exist in the discharge center where the ions have not yet been accelerated sufficiently. In most applications[1] ions hit the discharge boundaries with supersonic speed. The fact that in supersonic regions only an upwind discretisation ensures numerical stability means that for a supersonic outflow of particles no boundary conditions must be stated. The particle density and velocity are completely determined by the acceleration of particles in the discharge volume. This approach is well known in the field of fluid dynamics [78], [55], but one should be aware that the underlying analysis is based on the conservation equations for mass as well for momentum.

It is in accordance with previous works in the field of plasma physics that for ions leaving the plasma no boundary conditions at the border of the simulation domain must be stated.

---

[1] An example where ions do not hit the surface with supersonic speed is a small electrical (Langmuir) probe, which is positively biased and therefore repels positive ions.

Performing a rigorous analysis for the one-dimensional, stationary case as performed by Valentini [111] it can be shown that the coupled system of the conservation equations of mass and momentum contains an internal singularity at the point where the particles travel exactly with their accoustic speed. Removing this internal singularity delivers an additional constraint which guarantees a unique solution. An implementation is everything but trivial as the spatial position of the internal singularity is unknown. The application of shooting algorithms [81] is a possible workaround. Unfortunately, the whole analysis was carried out for static situations, the results cannot be directly exploited for the dynamic case.

In the literature, a great variety of possible approaches has been discussed. A large number of works have been published treating dynamic simulations of low pressure RF-discharges, and a selection of boundary conditions has been proposed. The situation is complicated because there are various possibilities to discretise the system of equations. Some authors like [7] and [119] used staggered meshes, which means that velocities and densities are only known at different points. Other authors like Passchier [76] used weak formulations obtained by integration of the conservation equations. Another important difference is the variety of the underlying models. In a minority of publications like [71], [103] conservation equations for mass as well as for momentum were used, while the majority applies a drift diffusion approximation. For the latter, the effect of supersonic outflow cannot be exploited so that boundary conditions have to be stated which express the fact that ion density drops significantly in the proximity of the boundaries. Very popular is to set the ion density zero at the boundary [84], [28], another common possiblity is to use v. Neumann boundary conditions i. e. to set the normal derivative of ion density zero [7], [76],[35].

However, the use of a zero ion density at the boundary does not necessarily produce vanishing ion densities in the proximity of the walls: The fact that wrong boundary conditions have almost no influence on the solution is proudly presented in [84].

3.3.4 Transport equations for electrons

The situation turns out to be even more complicated in the case of electrons. Under most conditions they remain in the subsonic region even if leaving the discharge. In this case mass as well as momentum conservation equation have to be used. Boundary conditions must be stated for density as well as for velocity.

In case of extreme acceleration, for example in the proximity of a small capacitively driven electrode, the electrons might reach supersonic speed. Finding a boundary condition which covers both regimes turns out to be a difficult task.

As almost all authors used the drift diffusion approximation for electrons [2], only a boundary condition for the electron density is required. Typically, the drop of electron density in the sheath region is much more pronounced[3] than the drop of ion density. An obvious approximation would be a boundary condition which assumes a vanishing electron density at the

---

[2] In this case the electron density is the only independent variable. The electron flux can be expressed by the density (gradient) and the local electric filed.

[3] several orders of magnitude

boundary.

On the other hand, in capacitively driven discharges the retarding potential in the sheath vanishes for a short part of the RF-cycle, so electrons can reach the boundary. During this time a non negligible electron density must exist at the boundary. A simple approach to consider the electron transport towards the wall is to perform a simple kinetic analysis. The assumption of an electron velocity distribution which is zero in one half of the phase space, provides a relation between electron density and flux (velocity):

$$\left|\vec{j}_e\right| = n_e \cdot \sqrt{\frac{kT_e}{2\pi m_e}}. \tag{3.30}$$

This approach can serve as a boundary condition as it provides a relation between the electron flux and the electron density at the boundary. This combination of the absolute value of electron density with its gradient can be used as a natural boundary condition for a drift diffusion model.

Another possibility to use (3.30) is the derivation of an outflow velocity with which the electrons hit the surface. This velocity can be used for the conservation of momentum in an electron model using conservation of mass as well as conservation of momentum. While this approach was used in [74], many authors preferred to set the electron density zero at the boundary.

For the electron energy conservation v. Neumann boundary conditions can be used for electron temperature, as most electrons can be assumed to be reflected in the sheath regions of the discharge and electronic heat conduction to the wall can therefore be neglected.

3.3.5 Boundary conditions for finite volume schemes

In the previous sections the boundary condition used by other authors have been discussed. The boundary conditions used for all calculations in this work will be discussed in the following. In many of the cited publications rather a finite difference approach had been chosen than a finite volume scheme. For the case of a finite volume discretisation two possibilities exist how the boundary region is discretised. They are shown in Fig. 3.2. In the first case a) the boundary cell consists of a half cell where the corresponding node is located on the cell boundary in the second case b) boundary cells and volume cells are identical, the corresponding node is located in the center of the cell.

Finite volume schemes are based on the fact that for each node (i. e. point where physical quantities are assumed to be known) a corresponding volume exists in which for each physical quantity a conservation equation is fulfilled. In case a) an obvious choice is to replace the conservation equation for the boundary volume by an explicit assignment for the boundary node value, i.e. a Dirichlet boundary condition. An alternative possibility is to use a conservation equation also for the boundary cell and to neglect the fact that the corresponding node is not located in the cell center. In this case, the flux across the boundary has to be expressed explicitely by the variables of the boundary node.

In case b) the boundary node is not exactly located on the boundary. For Dirichlet conditions it might be a disadvantage that location of the node and the boundary are different. For example,

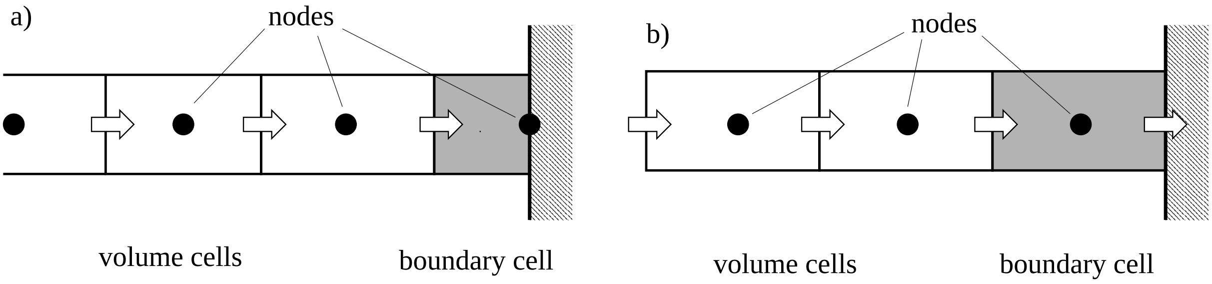

Figure 3.2: Finite volume/box discretisation: Two possibilities to discretise the boundary region. Filled circles denote nodes, i.e. points where the physical quantitities are assumed to be known, the rectangles surrounding the nodes are the corresponding boxes.

the potential Φ of the boundary might be known, but there exists no node on the boundary. For conservation equations of mass and momentum a volume integrated form might be used. For this purpose, particle as well as momentum flux across the outer boundary are required.

For all the calculations presented in this work, the discretisation scheme according to a) has been chosen.

3.3.5.1 Electron boundary conditions

With regard to the electron transport, two cases have to be distinguished:

In the drift diffusion model the only variable is the electron density. A simple kinetic approach provides an equation (3.30),which expresses the electron flux at the boundary as a function of electron temperature and density. For the boundary cell, in analogy to the volume cells, a conservation equation for mass is used with the only difference that the outflux towards the walls is given by (3.30).

In the case of a two-moment model, (3.30) is used to derive a velocity

$$v_{eB} = \sqrt{\frac{kT_e}{2\pi m_e}}, \tag{3.31}$$

which is used as a Dirichlet boundary condition for the electron velocity. As in the sheath region generation of ions and electron pairs by impact ionisation can be neglected, it might be assumed that the particle flux is constant in the sheath. From the assumption of a vanishing flux derivative, a mixed boundary condition for the electron density can be derived:

$$\frac{d}{dx} n_e v_e = 0 \quad \Rightarrow \quad n_e' v_e + n_e v_e' = 0 \quad \Rightarrow \quad n_e' + n_e \frac{v_e'}{v_e} = 0, \tag{3.32}$$

where v_{eB} denotes the component normal to the boundary of the electron velocity $\vec{v}_e$. The primes indicate a spatial derivative in the direction normal to the boundary.

3.3.5.2 Ion boundary conditions

Using the assumption of a flux conservation in the sheath region, a boundary condition for ion density can be formulated, in complete analogy:

$$\frac{d}{dx} n_i v_i = 0 \quad \Rightarrow \quad n_i' v_i + n_i v_i' = 0 \quad \Rightarrow \quad n_i' + n_i \frac{v_i'}{v_i} = 0 \tag{3.33}$$

In case of the ion velocity, one is confronted with the problem that the ion outflow takes place with supersonic velocity. The speed with which the ions leave the discharge depends on the (time dependent) potential drop in the sheath region, on the number of charge exchange collisions in the sheath, as well as on the ion mass. Most authors, who realised the existence of this difficulty, used an extrapolation from the interior to determine the outflow velocity [103], [76]. This may be understood as setting the second derivative of the density to zero. An alternative approach which has been succesfully tested in this work is the use of a mixed boundary condition:

$$v_{iB} - \alpha(v_{iB}') v_{iB}' = 0. \tag{3.34}$$

Here v_{iB} is the normal component of the ion velocity directed to the surface, and v_{iB}' its spatial derviative. The choice of a nonlinear function $\alpha(v_{iB}')$ is a quite “technical” problem. A possible choice is the following function:

$$\alpha(v_{iB}') = v_c + \gamma \exp(\delta v_{iB}'), \tag{3.35}$$

where v_c denotes the ion accoustic speed. Values of $\gamma = 1\,\mathrm{m/s}$ and $\delta = 10^{-5}\,\mathrm{s}$ lead to meaningful results in a wide range of parameters.

Chapter 4

Input data

So far collision processes have been treated on a very general level, i.e. as a contribution to the right hand sides of the conservation equations for mass, momentum and energy. In order to describe the change of mass, momentum or energy, effective collision frequencies or rates were introduced. In this section, a more detailed discussion of these terms will follow. As already discussed in Sect. 2.2, the behaviour of electrons and ions is fundamentally different, with the consequence that different types of collision processes have a dominant influence on the transport properties.

In the case of ions especially the charge exchange with neutral particles causes a significant loss of momentum and slows down the ambipolar diffusion process. For the electrons, a variety of different collision mechanisms is of importance:

Elastic collisions are responsible for momentum loss and limit the electric as well as the heat conductivity. Inelastic collisions cause a significant energy loss in the plasma volume and are responsible for impact ionisation, excitation and dissociation of neutrals.

In this chapter, the various types of collisions will be discussed, and the effective rates needed to assemble the right hand side of the conservation equations, will be derived. References to the underlying experimental data will be given.

4.1 Impact ionisation

In the conservation equations for mass (2.2), (2.21), (2.22) the right hand side is given by the difference of the generation and recombination of particles per time $G - R$. While the recombination given by R in the plasma volume can often be neglected[1], the generation or impact ionisation rate G is the dominant term.

As the generation of ion-electron pairs is caused by energetic electrons, the total number of generated charged particles is proportional to the number density of electrons n_e. Furthermore, the generation rate is proportional to n_N, the number density of the neutral particles which can be ionised.

---

[1] Due to a degree of ionisation in the order of 10^{-3}, electron-ion collisions resulting in recombination are rare in the low pressure regime.

The energy distribution of electrons is of crucial importance. As impact ionisation requires a threshold energy in the order of some electron volts, only electrons with sufficient energy can cause ionisation. In a general form, the generation of ion electron pairs is given by:

$$G = n_N \int\limits_{E=E_{iz}}^{\infty} \sigma\left(E\right) \sqrt{\frac{2E}{m_e}}\, f(E)\, dE \tag{4.1}$$

Here $\sigma(E)$ denotes the energy dependent ionisation cross section, E_{iz} is the minimum kinetic energy an electron needs to cause an ionisation. As the electron energy distributions tend to decrease significantly with increasing energy (exponentially in case of Maxwellian distributions), the energy region close to the ionisation threshold energy E_{iz} dominates the generation by impact ionisation.

A commonly used simplification to avoid the integration over the exact energy dependent ionisation cross section is the use of a step function for the cross section:

$$\sigma\left(E\right) = \begin{cases} 0 & E < E_{iz} \\ \sigma_T & E \geq E_{iz} \end{cases} \tag{4.2}$$

For a Maxwellian EEDF the integration can now be carried out analytically and the ionisation rate G is then given by:

$$G = n_e\, n_N \sigma_T \sqrt{\frac{8}{\pi}} \sqrt{\frac{kT_e}{m_e}} \left(1 + \frac{E_{iz}}{kT_e}\right) \exp\left(-\frac{E_{iz}}{kT_e}\right). \tag{4.3}$$

A further simplification is to neglect the temperature dependence of $E_{iz}/(kT_e)$ and to modify σ_T. This approach was, for example, chosen in [102] and leads to

$$G = n_N n_e \sigma_T \sqrt{\frac{8}{\pi}} \sqrt{\frac{kT_e}{m_e}} \exp\left(-\frac{E_{iz}}{kT_e}\right). \tag{4.4}$$

In Fig. 4.1 ionisation rates were calculated, using data given by different authors. In case of an argon plasma with a neutral gas pressure of $1\,\mathrm{Pa}$ and a neutral gas temperature of $300\,\mathrm{K}$, ionisation rates were determined for an electron temperature in the range of $10000 - 100000\,\mathrm{K}$. The full line shows the ionisation rate obtained by carrying out the integration over a Maxwellian distribution and using an energy dependent ionisation cross section given by [60]. The dashed curve is the corresponding approximation, calculated from (4.4), with the ionisation cross section $\sigma_T = 3.0 \cdot 10^{-20}\,\mathrm{m}^2$ as given in [102]. The correlation of both curves shows that (4.4) is an excellent approximation of the form given by (4.1). The dot-dashed curve is based on (4.3), with $\sigma_T = 2.0 \cdot 10^{-20}\,\mathrm{m}^2$ as used in [71], the dotted curve is based on the data given in [76].

Generally, the ionisation rate shows a rapid increase over several decades in regions of low electron temperatures $(T_e < 40000\,\mathrm{K})$. This is the region of main interest, as for many low pressure applications electron temperature is in this range. At higher electron temperatures $(T_e > 60000\,\mathrm{K})$ the ionisation rates tend to saturate, also the differences between the different approximations decrease, too.

As already was pointed out by Schottky in 1924, the geometry of a low pressure discharge and the ambipolar diffusion coefficient determine the value of the ionisation rate [92]. His

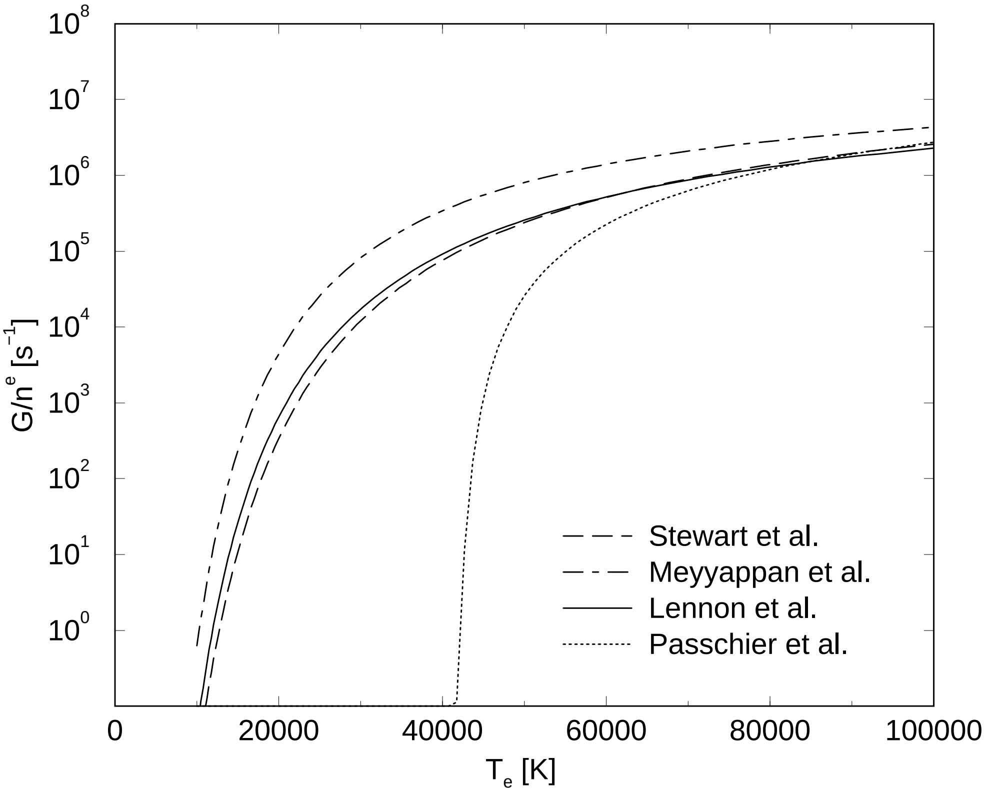

Figure 4.1: Ionisation rate for argon at $1\,\mathrm{Pa}$, $300\,\mathrm{K}$ in dependence of the electron temperature T_e. The results were calculated using cross sections or approximations given in [60], [102], [76] and [71]

calculations were based on a simplified diffusion model, neglecting the ion momentum and assuming particle density to vanish at the discharge walls.

The steep increase of the ionisation rate with the electron temperature is the reason why also a more sophisticated system model including conservation equation for mass, momentum and energy will be insensitive to the choice of σ_T. Regardless, whether the data from [60], [102], or [71] are used, the corresponding simulation result for the electron temperature will be similar.

Only the approach used by Passchier and Goedheer differs significantly, as it is based on the assumption that a minimum mean electron energy of $5.3\,\mathrm{eV}$ is required for impact ionisation processes. This means that electron temperature for any discharge has to be higher than $41000\,\mathrm{K}$, an assumption that will not be used in this work.

In Fig. 4.2 ionisation cross sections for helium, neon, argon, krypton, and xenon are shown for the energy range from $10 - 50\,\mathrm{eV}$. While for argon and helium the integration over a Maxwellian energy distribution can be approximated with sufficient accuracy by using (4.4) or (4.3), for other noble gases a more sophisticated approximation has to be chosen. According to [10], an approximation of the electron dependent ionisation rate by a power series provides

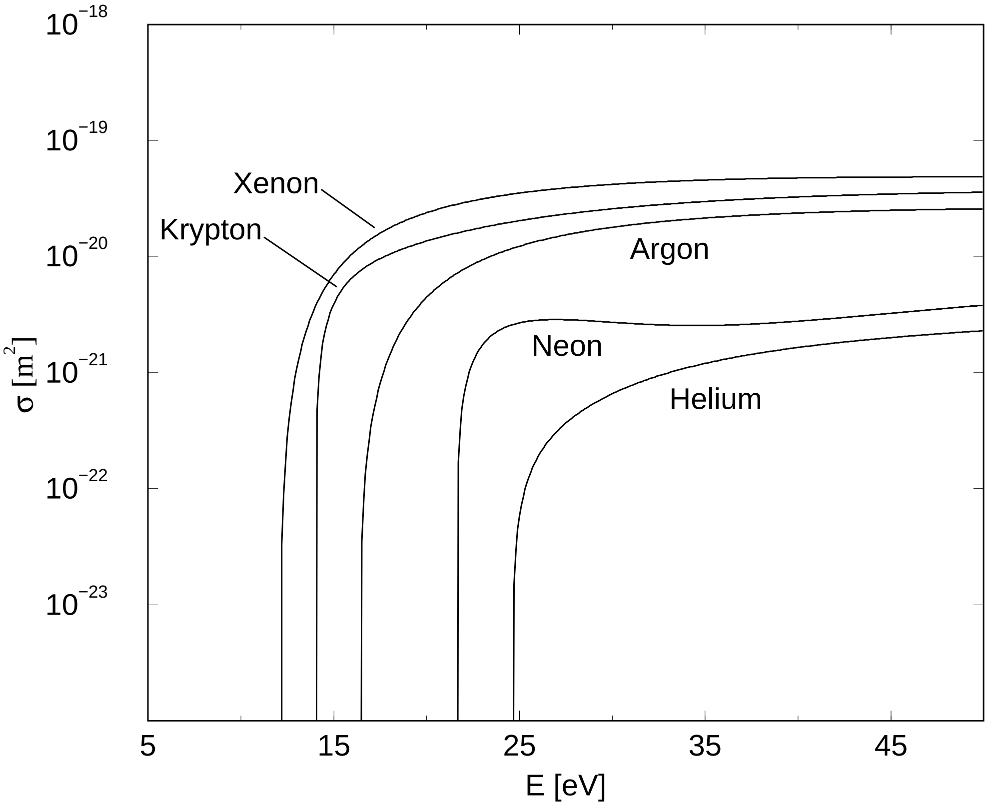

Figure 4.2: Ionisation cross sections for noble gases calculated from approximations given in [10], [60], [39]

.

sufficiently accurate results:

$$G\left(T_e\right) = n_e\, n_N\, \exp\left(-\frac{E_{iz}}{kT_e}\right)\sqrt{\frac{kT_e}{E_{iz}}}\sum_{n=0}^{5} a_n\left(\log_{10}\left(\frac{kT_e}{E_{iz}}\right)\right)^n \tag{4.5}$$

The corresponding coefficients for various noble gases are given in Tbl. 4.1.

	E_{iz}[eV]	$a_0\,[s^{-1}]$	$a_1\,[s^{-1}]$	$a_2\,[s^{-1}]$	$a_3\,[s^{-1}]$	$a_4\,[s^{-1}]$	$a_5\,[s^{-1}]$
Helium	24.6	1.464E-14	-2.301E-15	-1.574E-14	-2.099E-14	-1.439E-14	-4.395E-15
Neon	21.6	2.343E-14	-1.787E-14	-6.509E-14	-1.881E-13	-1.368E-13	-3.296E-14
Argon	15.8	9.472E-14	1.491E-15	-5.929E-14	1.797E-14	1.296E-14	-9.720E-15
Krypton	14.0	1.202E-13	-8.174E-15	-4.906E-14	-5.803E-14	1.748E-14	2.430E-14
Xenon	12.1	1.472E-13	-9.180E-16	-1.098E-13	3.231E-14	9.499E-14	3.237E-14

Table 4.1: Coefficients to calculate the ionisation rate for noble gases using (4.5). The underlying ionisation cross sections are given in [10], [60] and [39].

4.2 Ion momentum loss

Ions tend to very effectively lose momentum by collisions with neutral particles, particularly with their parent gas. The dominant mechanism is a charge exchange process resulting in a fast neutral particle and an ion, which keeps the thermal velocity of the initially neutral particle. The momentum loss of the ions has a crucial influence on the transport processes in the discharge and will be discussed in detail in Chapter 5.

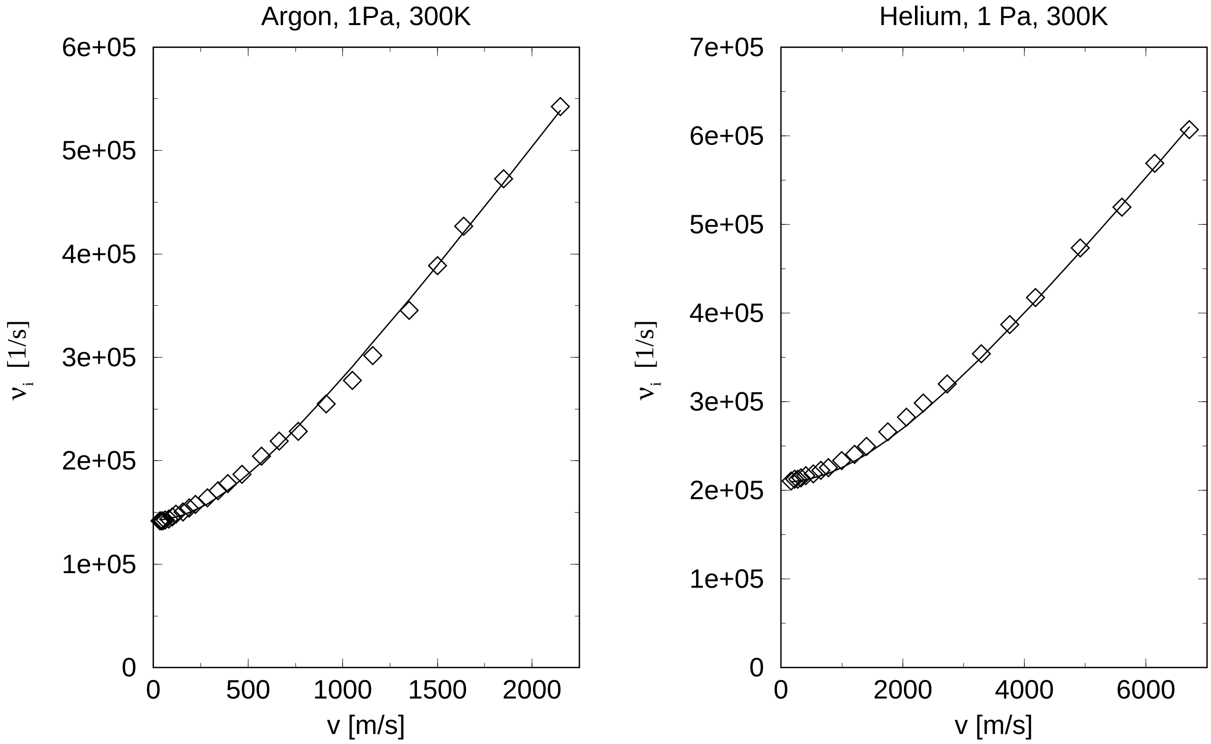

Figure 4.3: Ion momentum loss rate ν_i versus ion drift velocity for argon and helium at $1\,\mathrm{Pa}$, $300\,\mathrm{K}$. The diamonds represent experimental data shown in [27], the full lines a semiempirical fit (4.6).

Various authors presented data from which the momentum loss rate ν_i, used in (2.26), can be calculated. A collection of data for a great variety of ions and background gases is given in [27]. The experimental data generally show a velocity dependence of the momentum loss rate which should be considered by an accurate transport model. For this purpose, a velocity dependent momentum loss rate $\nu_i(v)$ is used for all following calculations. Experimental data generally show an increase in the ion-neutral collision rate with an increasing drift velocity. At higher velocity, the measurements indicate a direct proportionality of drift velocity and collision frequency[2]. Deviations from this proportionality become visible only in the region of very low

---

[2] This indicates that the charge exchange cross section is velocity independent. The number of collisions for this case is proportional to the travelled distance which is proportional to the drift velocity.

velocity. An empirical approach to express this velocity dependence in a parameterised form:

$$\nu_i(v) = n_N \cdot \sqrt{a_0 + a_1 v^2} \tag{4.6}$$

In Fig. 4.3 experimental data [27] and a polynomial fit are shown for the case of argon and helium. Polynomial approximation fit the experimental values with similar accuracy for other noble gases. The corresponding values of the coefficients are given in Tbl. 4.2.

	$a_0\ [m^6\ s^{-2}]$	$a_1\ [m^4]$
Helium	$7.5\,10^{-31}$	$1.25\,10^{-37}$
Neon	$2.0\,10^{-31}$	$1.9\,10^{-37}$
Argon	$3.5\,10^{-31}$	$1.0\,10^{-36}$
Krypton	$2.6\,10^{-31}$	$1.1\,10^{-36}$
Xenon	$2.4\,10^{-31}$	$2.5\,10^{-36}$

Table 4.2: Coefficients to express the velocity dependent momentum loss frequency of noble gas ions in their parent gases by (4.6). Underlying experimental data are given in [27],[26]

Unfortunately, the ion velocities occurring in low pressure discharges can exceed the range, for which mobilities have been measured, by one order of magnitude. This means that for sheath regions the ion friction can only be derived from extrapolated data. In Chapter 5 a sensitivity analysis will be presented which demonstrates how sensitive hydrodynamic transport models depend on the parameters of Tbl. 4.2. However, the ion velocities in the discharge bulk are normally in the experimental range and can be considered as reliable.

4.3 Elastic electron-neutral collisions

The most dominant mechanism, causing a loss of electron momentum, are elastic electron-neutral collisions. Please note that an elastic electron-neutral collision does only cause a very small change of the electron's energy while a significant part of the momentum might be lost. From an experimental point of view, the momentum exchange cross sections can be directly determined with various methods [95], and a great variety of data was published especially for noble gases. A compilation of sources for cross section data is given in Tbl. 4.3.

Electron-neutral collisions have influence on the right hand side of the equations the electron momentum conservation (2.28), the heat flux (2.33). Also the plasma's electrical conductivity (2.42), (4.7) is influenced.

Please note that electron neutral collisions in the aforementioned equations were represented by effective electron neutral frequencies ν_{me} and ν_{ee}, which in a more general form will depend on the electron energy distribution and the energy dependence of the corresponding collision cross section. In the following the source terms for the different equations will be discussed separately. The momentum exchange cross section shows a strong dependence on the energy of the incident electron for some gases.

	total momentum exchange	differential
Helium	[90], [89], [31], [21]	[57], [83], [34]
Neon	[88], [31]	[83], [36]
Argon	[79], [80], [72], [31]	[32], [83], [36], [79], [80]
Krypton	[59], [42], [80], [31], [29], [23]	[83], [36], [80], [22], [29]
Xenon	[59], [42], [67], [31]	[83], [36]

Table 4.3: Electron-neutral momentum exchange cross sections for elastic scattering of electrons in noble gases.

A prominent example is argon with a very pronounced Ramsauer minimum at an energy of 0.15 eV and a variation over two decades for higher energies. Krypton and xenon show this behaviour, too. For helium and neon, no Ramsauer minimum exists, the momentum exchange cross section rises monotonically until a maximum is reached (at 2 eV for helium, at 20 eV for neon). This maximum and the decrease of the cross section with higher energies is a characteristic behaviour for argon, krypton, and xenon, too. This decrease of the momentum exchange cross section with increasing electron energy has consequences for the transport properties in the corresponding gas and will be discussed in detail in the following.

4.3.1 Electric RF-conductivity

The plasma's electrical conductivity is of interest in order to understand the mechanism of collisional heating in the discharge. As the power transferred to the electrons is proportional to the real part of the complex conductivity $\underline{\sigma}$, it is desirable to understand how $\underline{\sigma}$ depends on parameters like electron temperature and neutral gas density. Unfortunately, a simple approach (2.42) based on a scalar effective collision frequency ν_{me} does not provide a sufficiently accurate value for the conductivity in the whole parameter range of interest.

It is well known [64] that influence of electron temperature, neutral gas density, and the EEDF have to be considered for neutral gases which show a energy dependent momentum exchange cross section. An example is the noble gas argon for which the collision rate is known to be strongly energy dependent. A general form of the plasma's conductivity considering the energy dependence for electron-neutral momentum exchange, can be derived from a two term expansion of the Boltzmann equation [95], [33]. Then the conductivity is given by

$$\underline{\sigma} = -\frac{4\pi}{3}\frac{n_e e^2}{m_e}\int\limits_{v=0}^{\infty}\left(\frac{\nu(v)v^3}{\omega^2+\nu^2(v)} - i\frac{\omega v^3}{\omega^2+\nu^2(v)}\right)\frac{\partial f_0}{\partial v}\,dv, \tag{4.7}$$

where $\nu(v) = \sigma(v) n_N v$ denotes the velocity dependent momentum exchange frequency for electron neutral collisions and $f_0(v)$ the normalised isotropic part of the electron energy distribution function EEDF. For any value of the angular RF-frequency ω, two independent scalar parameters (real and imaginary part) are needed in order to express $\underline{\sigma}$.

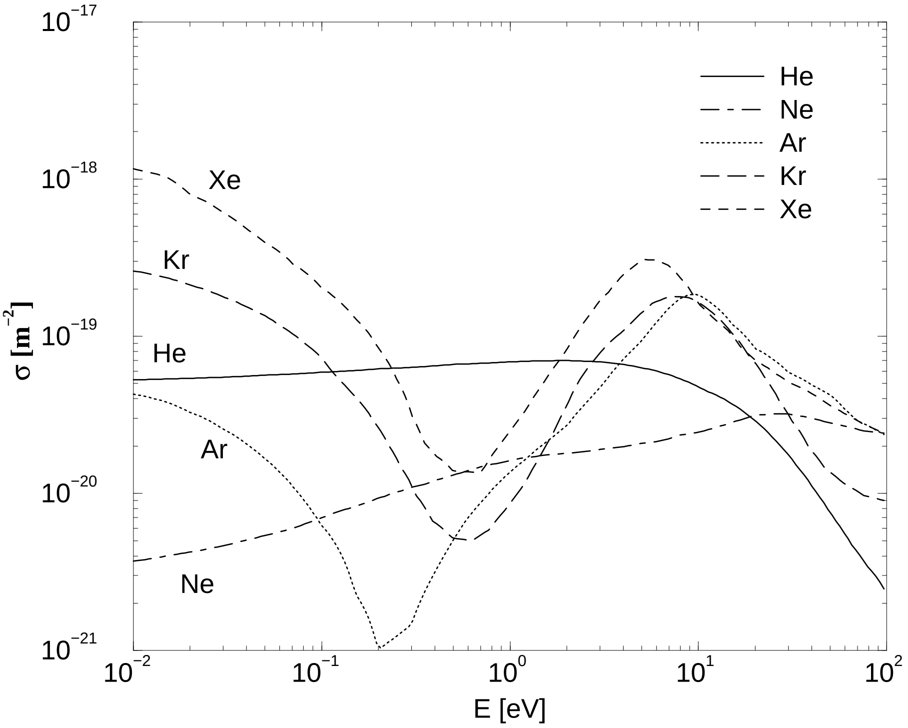

Figure 4.4: Momentum exchange cross sections for various noble gases in dependence of electron energy. Data for He from [21], for Ne from [88], for Ar from [31], for Kr from [59], [23] and for Xe from [31]

As in some cases the deviations from the simple expression of conductivity (2.42) may be small, in [64] a correction, which suggests the introduction of an effective RF-frequency ω_{eff} and of an effective collision frequency ν_{eff} was proposed:

$$\underline{\sigma} = \frac{n_e e^2}{m_e \left(\nu_{eff} + i\omega_{eff}\right)} \tag{4.8}$$

With the two independent variables ω_{eff} and ν_{eff}, the real and imaginary part of $\underline{\sigma}$ can take arbitrary, independent values. However, in case of small deviations from (2.42) it can be expected that ω_{eff} almost equals the angular frequency ω_{RF}, and ν_{eff} is a measure for the mean electron neutral collision frequency.

Especially for argon, the energy dependence of the momentum cross section is responsible for the fact that ω_{eff} and ν_{eff} vary significantly with the mean electron temperature and the neutral particle density.

In Figs. 4.5, 4.6 the dependence of ω_{eff}/ω_{RF} and ν_{eff}/ω_{RF} are shown for a wide range of parameters. A numerical compilation of the same data is given in Appendix A in Tbl. A.1 and Tbl. A.2. The results have been calculated by carrying out the integration in (4.7) under the assumption of a Maxwellian distribution. For all calculations a neutral gas temperature of

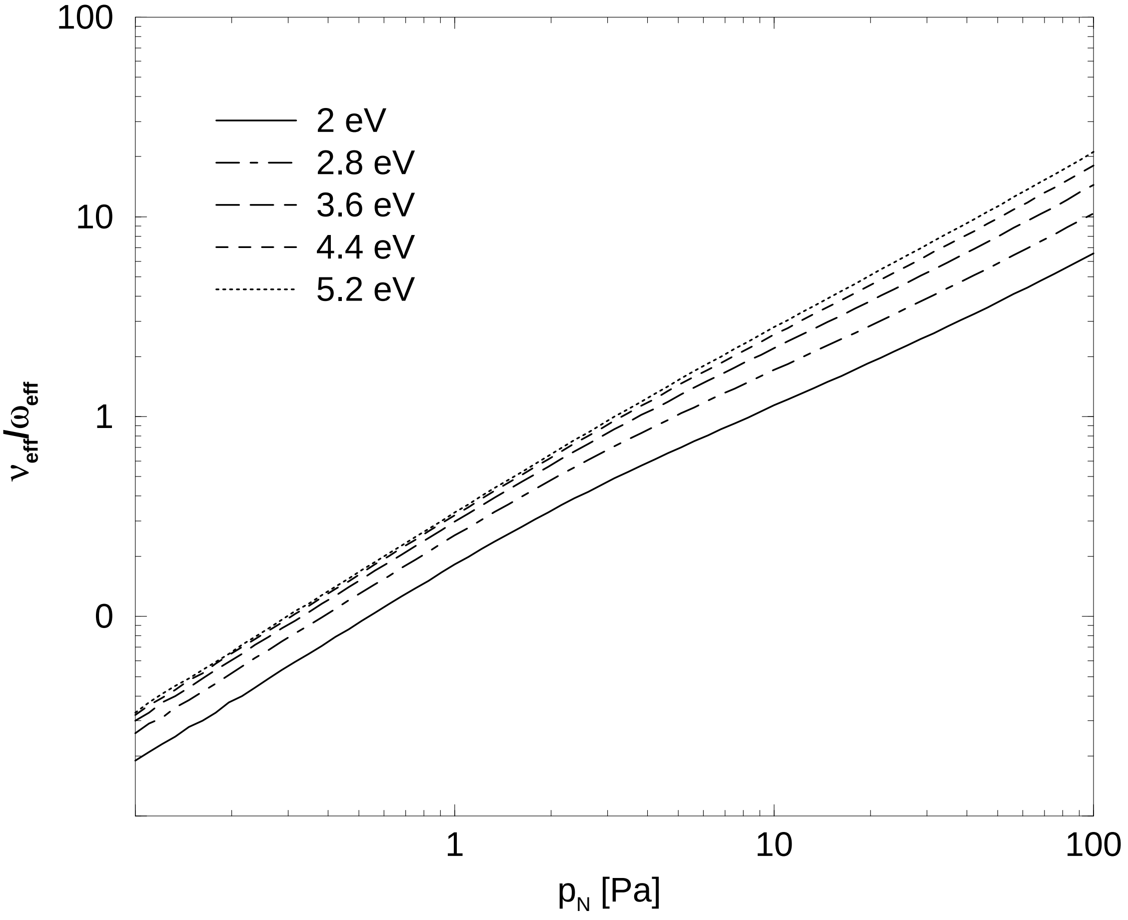

Figure 4.5: Normalised effective momentum transfer frequency ν_{eff}/ω_{RF} for argon for a pressure range from 0.1 Pa to 100 Pa and an electron temperature from $2-5.2$ eV. A neutral gas temperature of $T_N = 300\,\mathrm{K}$, $\omega_{RF} = 2\pi \cdot 27\,\mathrm{MHz}$ was assumed.

$T_N = 300\,\mathrm{K}$ was assumed.

The behaviour of the effective collision frequency ν_{eff} is characterised by a general increase with neutral gas pressure. This corresponds to an increasing number of collisions. However, a proportionality is only observed for neutral gas pressures below 1 Pa. Deviations from a direct proportionality become visible especially in the pressure regime over 20 Pa in case of low electron temperature (2 eV). The general dependence of ν_{eff} on the mean electron temperature T_e can be explained by a higher average velocity with increasing temperature. For higher temperatures, collision events become more frequent, which results in an increase of ν_{eff}.

The dependence of the effective RF-frequency ω_{eff} is more complicated (see Fig. 4.6). In the region of low pressure ($p_N < 1\,\mathrm{Pa}$), ω_{eff}/ω_{RF} equals almost unity. In combination with an approximately direct proportionality of ν_{eff} to the neutral gas pressure, this indicates that

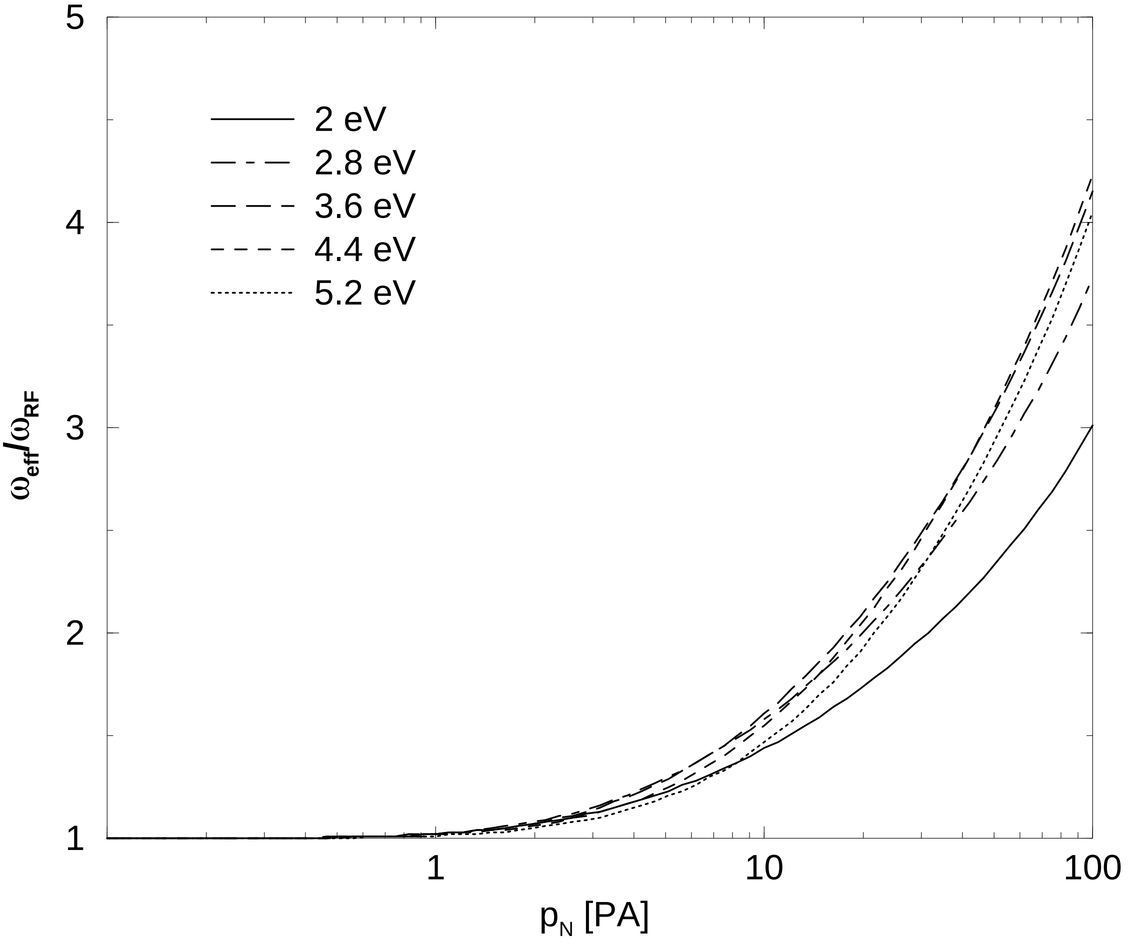

Figure 4.6: Normalised effective RF frequency ω_{eff}/ω_{RF} for argon for a pressure range from 0.1 Pa to 100 Pa and an electron temperature from $2 - 5.2$ eV. A neutral gas temperature of $T_N = 300\,\mathrm{K}$, $\omega_{RF} = 2\pi \cdot 27\,\mathrm{MHz}$ was assumed.

the simple conductivity formula (2.42) is applicable in that range. However, with increasing pressure, ω_{eff}/ω_{RF} increases significantly. At a pressure of $P_N = 10\,\mathrm{Pa}$, a correction factor of approximately 1.5 has to be used. The temperature behaviour of ω_{eff}/ω_{RF} shows intersecting curves in Fig. 4.6 for various electron temperatures. This is caused by the complicated shape of the underlying electron-neutral momentum exchange cross section. Generally, with an increasing neutral gas pressure, the ratio ω_{eff}/ω_{RF} increases, but the curvature appears to depend on the assumed electron temperature. For details see Tbl. A.2.

The fact that ω_{eff} almost equals ω for pressure values lower than 1 Pa, indicates that (2.42) is a suitable approximation in this range. However, it is not obvious what the direct consequences are, when (2.42) is not applicable.

In order to interpret the influence on discharge heating for higher pressure values, the real part of the corresponding conductivity $\underline{\sigma}$ must be examined. From (4.8) follows directly:

$$\underline{\sigma} = \nu_{eff} \frac{n_e e^2}{m_e \left(\nu_{eff}^2 + \omega_{eff}^2\right)} - i\omega \frac{n_e e^2}{m_e \left(\nu_{eff}^2 + \omega_{eff}^2\right)}, \tag{4.9}$$

and therefore for the real part of the conductivity

$$\Re\{\underline{\sigma}\} \sim \frac{\nu_{eff}}{\nu_{eff}^2 + \omega_{eff}^2} \sim \frac{\nu_{eff}/\omega_{RF}}{(\nu_{eff}/\omega_{RF})^2 + (\omega_{eff}/\omega_{RF})^2}. \tag{4.10}$$

Please note that for $\nu_{eff} < \omega_{RF}$, i.e. low pressure values, a direct proportionality can be expected, while for high pressure i.e. $\nu_{eff} > \omega_{eff}$ an indirect proportionality to ν_{eff} can be expected.

The dependence of the normalised real part of the conductivity is shown in Fig 4.7 as well as in Tbl. A.3 for different values of the neutral gas pressure and the electron temperature. The corresponding variation of ν_{eff} and ω_{eff} is considered according to the data in Tbl. A.1 and Tbl. A.2.

For low pressure values ($p_N < 1\,\mathrm{Pa}$) the real part of the conductivity shows in fact the expected almost linear increase with the pressure, reaches a maximum and finally decreases. At low electron energies, the position of the maximum moves towards higher neutral gas pressures and is, for the whole parameter range, located between $3\,\mathrm{Pa}$ and $5\,\mathrm{Pa}$. This means that in case of argon, in this pressure range energy, can be most effectively transferred to the plasma by an alternating field. The dependence on the electron temperature appears to be weak.

4.3.2 Electron momentum loss

In the electron momentum conservation (2.28), the momentum loss caused by elastic collisions turns out to have minor influence compared to the dominant terms which are the partial pressure gradient $\nabla n_e k T_e$ and the momentum change in the electric field $n_e e \vec{E}$. A coupled system of hydrodynamic conservation equations shows the tendency to react almost not on changes in the electron's momentum loss term. The physical reason for that is the random velocity of the electrons, which greatly exceeds the directed (drift) velocity.

However, an effective momentum loss frequency can be derived in dependence of the electron temperature. For this purpose (4.7) might be evaluated for the limiting case of $\omega \longrightarrow 0$. The DC conductivity of the plasma is then given by:

$$\sigma_{DC} = -\frac{4\pi}{3} \frac{n_e e^2}{m_e} \int\limits_{v=0}^{\infty} \frac{v^3}{\nu(v)} \frac{\partial f_0}{\partial v}\, dv. \tag{4.11}$$

Using $\nu(v) = n_N \sigma(v) v$ and the conservation equation of the momentum (2.28) for the stationary case under the assumption of a vanishing partial pressure gradient, we can derive the electron-neutral momentum loss frequency ν_{me}:

$$\frac{1}{\nu_{me}} = -\frac{4\pi}{3} \int\limits_{v=0}^{\infty} \frac{v^2}{\sigma(v)\, n_N} \frac{\partial f_0}{\partial v}\, dv. \tag{4.12}$$

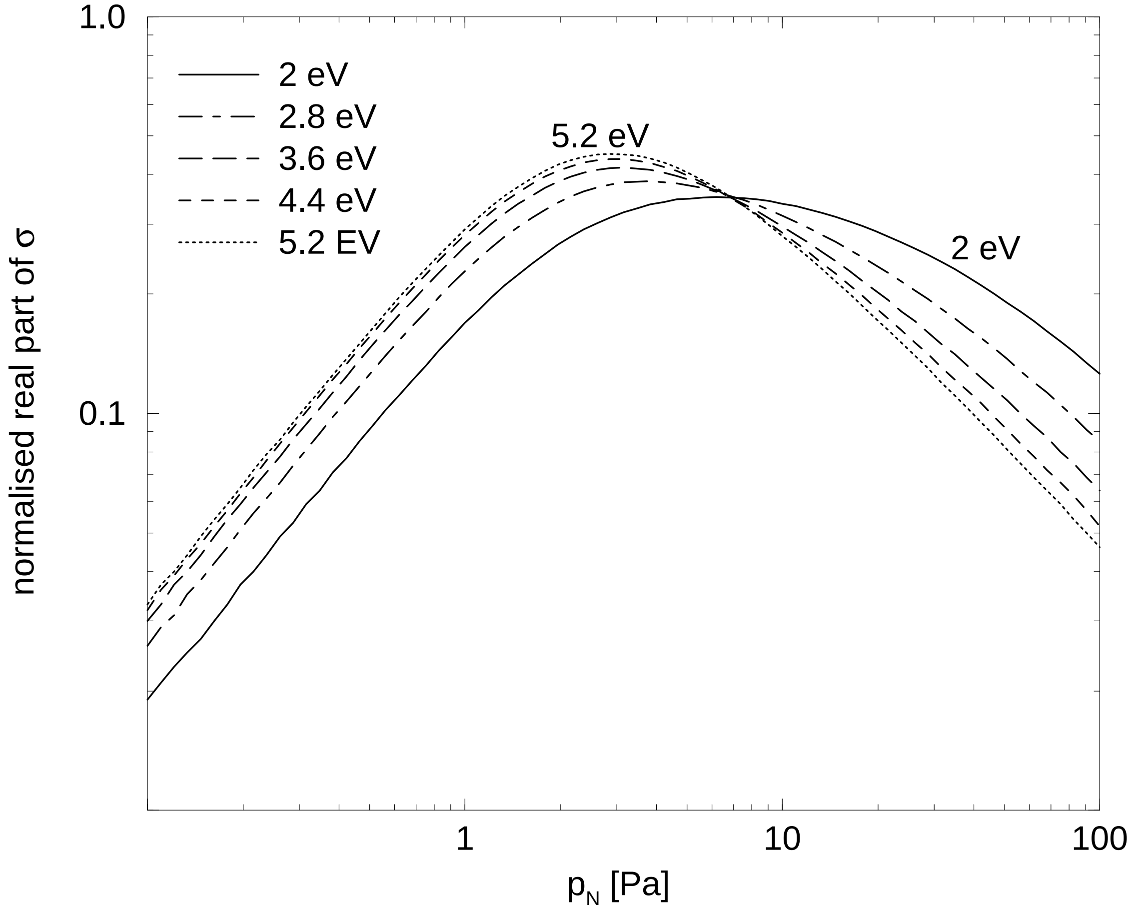

Figure 4.7: Normalised real part of the complex conductivity, defined in (4.10) for argon, in a pressure range from 0.1 Pa to 100 Pa and at an electron temperature from 2 eV to 5.2 eV. A neutral gas temperature of $T_N = 300\,\mathrm{K}$, $\omega_{RF} = 2\pi \cdot 27\,\mathrm{Mhz}$ was assumed.

The value of the momentum loss frequency ν_{me} therefore depends on the momentum exchange cross section $\sigma(v)$ and on the electron energy distribution function. Under the assumption of a Maxwellian EEDF,[3] the momentum loss frequency can then be calculated in dependence of electron temperature. The density of the neutral particles determines the velocity dependent collision frequency $\nu(v)$, therefore the averaged momentum loss frequency ν_{me} is directly proportional to the neutral particle's density. The results normalised to the neutral particle density are shown in Fig. 4.8.

The shape of the elastic electron-neutral momentum exchange cross section, in combina-

---

[3] As the integral is dominated by low energy electrons in the bulk of the EEDF, the assumption of a Maxwellian EEDF is a good approximation. As the number of energetic electrons is generally very low, the well known depletion of the high energy tail has minor influence on the momentum loss frequency.

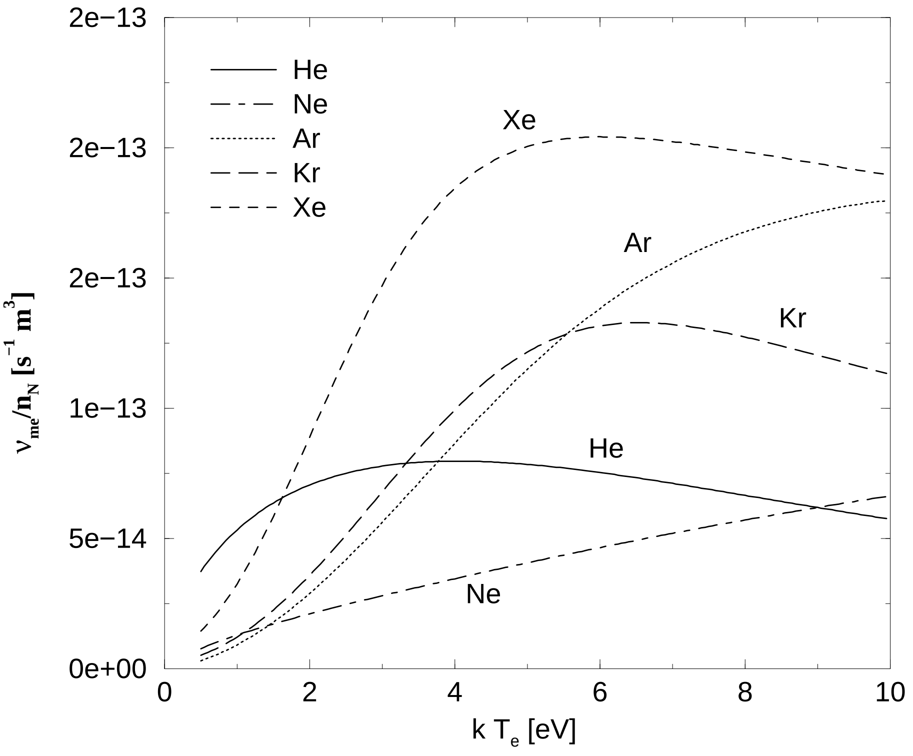

Figure 4.8: Normalised momentum loss frequency ν_{me}/n_N for various noble gases in dependence of the electron temperature T_e.

tion with the increasing number of electron neutral collisions at higher electron temperatures, leads to an increasing momentum loss frequency for all considered gases in the low energy regime. The decrease of the electron-neutral momentum exchange cross section for energies higher than 10 eV is especially pronounced for He and Xe, which means that the momentum loss frequency shows a maximum and a decrease at higher electron temperatures. The only noble gas which shows a monotonical increase in the momentum loss frequency is neon. This behaviour is caused by an electron-neutral momentum exchange cross section which increases monotonically in the energy range between 0 and 20 eV.

4.3.3 Heat conduction

While the momentum loss caused by electron-neutral collisions has minor influence on the momentum conservation, the situation is fundamentally different for the heat flux equation which describes the transport of thermal energy driven by temperature gradients. The thermal conductivity is indirectly proportional to the frequency of electron-neutral collisions ν_{ee}. In a general form ν_{ee} can be derived from a two-term expansion of Boltzmann's equation [33]:

$$\frac{1}{\nu_{ee}} = \frac{T_e}{m_e}\frac{4\pi}{3}\int\limits_{v=0}^{\infty} \frac{v^4}{\sigma(v)\, n_N} f_0 \, dv. \tag{4.13}$$

However, in case of a Maxwellian energy distribution, the collision frequencies for momentum loss and energy transport are equal [33], i.e.

$$\nu_{ee} = \nu_{em}. \tag{4.14}$$

Chapter 5

1-D Results

In order to compare the different model systems and to perform a sensitivity analysis for various model parameters, in this section one-dimensional calculations will be presented. The restriction to only one spatial dimension has the advantage that the influence of each model parameter can be identified more easily than this in case of a more-dimensional model. Also, a quantitative comparison of different model approaches can be easily performed and delivers meaningful results.

In this chapter, especially the question will be discussed how the simplifications proposed in Sect. 2.2 influence simulation results. Different possible model systems will also be discussed and compared.

5.1 Static solutions of the hydrodynamic equations

To understand the basic correlations between the model parameters and the simulation results, the simple case of static solutions is going to be discussed, in this section. In the following section, the more complicated case of time-varying problems will be treated.

5.1.1 Drift diffusion approximation versus momentum conservation equation

Based on the conservation equations for mass and momentum in Sect. 2.2, two possibilities have been proposed for describing the electron transport in low pressure plasmas: The more general approach is based on a system of mass and momentum conservation, while in a simplified version the momentum conservation is neglected and the electron flux is directly expressed by the electron density gradient and by the electric field (drift diffusion approximation). For the one-dimensional (planar) case, the corresponding equations take the form:

Two-moment model for electrons:

$$\frac{\partial n_e}{\partial t} + \frac{\partial}{\partial x}(n_e v_e) = G - R, \tag{5.1}$$

$$\frac{\partial}{\partial t}(n_e v_e) + \frac{\partial}{\partial x}\left(n_e v_e^2 + n_e k T_e\right) = -\frac{e n_e E}{m_e} - n_e v_e \nu_{me}. \tag{5.2}$$

one-moment model for electrons (drift-diffusion approximation):

$$\frac{\partial n_e}{\partial t} + \frac{\partial j_e}{\partial x} = G - R, \tag{5.3}$$

with

$$j_e = -\frac{e n_e E}{m_e \nu_{me}} - \frac{1}{m_e \nu_{me}} \frac{\partial}{\partial x}(n_e k T_e). \tag{5.4}$$

In order to obtain a complete model, the transport processes of ions have to be considered, too. As discussed in Sect. 2.2, in case of positive ions, a two-moment model is a good choice in the discharge bulk as well as in the sheath regions:

Two-moment model for positive ions:

$$\frac{\partial n_i}{\partial t} + \frac{\partial}{\partial x}(n_i v_i) = G - R, \tag{5.5}$$

$$\frac{\partial}{\partial t}(n_i v_i) + \frac{\partial}{\partial x}\left(n_i v_i^2 + n_i k T_i\right) = \frac{q n_i E}{m_i} - n_i v_i \nu_{mi}(v_i), \tag{5.6}$$

where q_i denotes the charge per ion.

One-moment model for negative ions (drift diffusion approximation):

Negative ions are repelled by the ambipolar electric field and can therefore be expected to accumulate in the bulk of the discharge. This means that their behaviour is fundamentally different from these of the positive ions, which are driven towards the wall by the ambipolar electric field. The concentration in the bulk, i.e. in a region with electric fields which are small compared with the field in the sheath, means that inertia plays a minor role for neagtive ions. Therefore, the conservation of mass in combination with a drift diffusion approximation might be a sufficiently accurate description:

$$\frac{\partial n_i}{\partial t} + \frac{\partial j_i}{\partial x} = G - R, \tag{5.7}$$

with

$$j_i = \frac{q_i n_i E}{m_i \nu_{mi}} - \frac{1}{m_i \nu_{mi}} \frac{\partial}{\partial x}(n_i k T_i). \tag{5.8}$$

To complete the system, the electric interaction of the different charged particles has to be considered. It proves to be useful to introduce a scalar potential Φ, which can be calculated from Poisson's equation. In a general formulation including N_i different ion species, the potential can be calculated from

Poisson's equation:

$$\frac{d^2\Phi}{dx^2} = \frac{1}{\epsilon_0}\left(en_e - \sum_{i=1}^{N_i} q_i n_i\right). \tag{5.9}$$

The electric field is given by the spatial derivative of Φ:

$$E = -\frac{d\Phi}{dx}. \tag{5.10}$$

5.1.2 The eigenvalue of the electron temperature

Using the equations (5.1), (5.2), (5.5), (5.6) and (5.9), (5.10) a self-consistent system of equations is given which can be solved numerically. Please keep in mind that for this purpose not only values like m_i, ν_{mi}, and T_i have to be provided, but that also the important electron temperature T_e has to be known.

Many authors solved this problem by adding a conservation equation for the electron energy (2.32) to the system. In case of low pressure (electron mean free path in the order of discharge dimension or even larger), this additional equation does not provide much surprising information. The good heat conductivity of the plasma (inversely proportional to the electron-neutral collision frequency) is the reason why the electron temperature profile in the whole discharge is very flat and almost constant, even if the heating of the discharge takes place only locally.

In this case it makes sense to replace the flat temperature profile by a constant value and to abstain from the use of an energy conservation. But which value for the electron temperature should be chosen? The electron temperature does not only influence the transport properties of the electrons, but is also a crucial parameter determining the generation of electrons and positive ions by impact ionisation[1].

The choice of a value for T_e, which is too high, will result in a permanent increase of the electron and ion density, a value which is too low, will result in a decrease of the electron and ion density. In a general way, this question had already been discussed for the heating of inductively driven discharges in Sect. 2.3. If we assume a spatially constant electron temperature profile, for a given geometry only one value for T_e results in a stable (not time-varying) density distribution.

This fact was already recognised in 1924 by Walter Schottky, who calculated the volume production of charged particles in a positive column [92], using a simple diffusion equation to describe the particle transport. However, even with more sophisticated models like a set of hydrodynamic equations the underlying principle remains valid: If the discharge dimension and parameters like collision frequencies are given, there exists one and only one[2] eigenvalue for the electron temperature, which guarantees a constant electron and ion density in the discharge. The eigenvalue represents the ability of the discharge to transport particles (generated in the volume) to the walls.

---

[1] Under the assumption of a Maxwellian energy distribution, the temperature dependence of the impact ionisation rate is dominated by an exponential term. An approximation is given in (4.3).

[2] A mathematically rigorous proof for the existence and uniqueness of an eigenvalue is possible in case of a diffusion driven transport with Dirichlet boundary conditions [92]. For more sophisticated model systems including different charged species, only experimental mathematics indicate that a unique solution might exist.

This fact must not be underestimated, please recall the discussion about particle generation in Sect. 4.1. Simplified models for impact ionisation in dependence of the electron temperature show a rapid increase of particle production in a small temperature range. As discharges typically operate in this region, the eigenvalue for the electron temperature is dominated by the particle production term G rather than by the $\nabla n_e k T_e$ term, which represents the transport by diffusion.

A point of criticism commonly raised against hydrodynamic models is the underlying assumption of a Maxwellian energy distribution. Experimental as well as theoretical works indicate that such an assumption is more or less wrong for the high energy region of EEDFs (c.f Sect. 2.1). The use of a hydrodynamic model in combination with a generation rate based on a Maxwellian EEDF, would therefore lead to wrong simulation results. On the other hand, the existence of a unique eigenvalue for the particle generation in a fixed discharge geometry relativates this point of criticism.

In order to deliver a steady state solution, the simulator has to calculate an electron temperature. This eigenvalue is determined by the discharge geometry and the ability of the ions to be driven to the walls. The generation rate $G(T_e)$ has minor influence as long as the generation in the region of interest is a steep function (c.f. Fig. 4.1). This is the case for all noble gases.

The use of a constant electron temperature instead of an electron energy conservation equation has an additional advantage: The average or peak electron density in the discharge represents a degree of freedom which can be chosen arbitrarily. In a numerical representation this means that one equation, determining the average or peak electron density, has to be added to the system. The global electron temperature T_e is calculated from this equation. Please note that independent of the number of discretisation points, only one equation is needed to perform a control of T_e, while in case of an energy conservation for each discretisation point the energy transport equation has to be solved.

A final consequence of the assumption of a distict electron temperature eigenvalue should be mentioned: The restriction to one eigenvalue for the electron temperature, instead of a temperature profile, has the advantage that the overall particle generation in the discharge is directly correlated with this eigenvalue. The general (volume averaged) ability of a discharge to produce charged particles can be estimated using the electron temperature eigenvalue as an indicator.

5.1.3 The most simple demonstration example

To illustrate the typical properties of a hydrodynamic model, the most simple setup is going to be discussed. In Fig. 5.1 the results of a one-dimensional, planar noble gas discharge are presented. The results might be understood as a cross section of a planar low pressure inductively coupled discharge. The limiting boundaries of the discharge had a distance of 5 cm.

Only one species of ions (positive argon ions) was considered, for ions as well as for electrons a two-moment model, i.e. the conservation equations for mass and momentum, was used. Volume recombination was neglected (R = 0) while for the generation of electron-ion pairs by impact ionisation the approximation (4.3) was used. A neutral gas pressure of 1 Pa and a neutral gas temperature of 300 K were assumed. For the average electron density a value of

$10^{15}\,\mathrm{m}^{-3}$ was chosen, the corresponding eigenvalue for the electron temperature had the value of $T_e = 35516\,\mathrm{K}$.

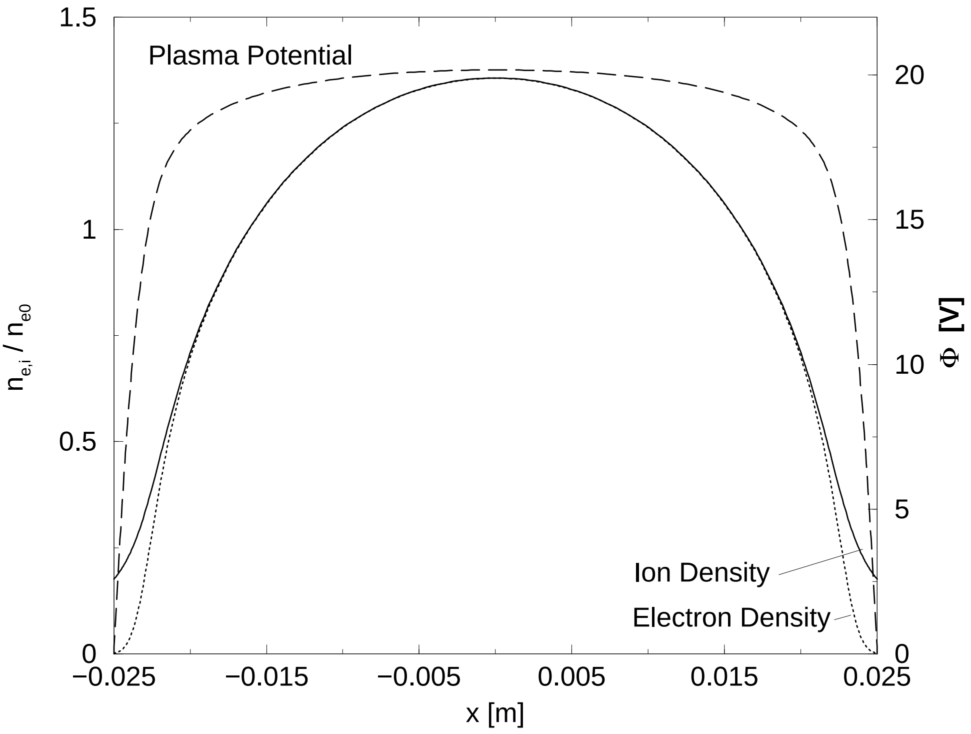

Figure 5.1: Electron density (dotted line, left scale), ion density (full line, left scale) and plasma potential (dashed line, right scale) in a planar argon discharge, $P_N = 1\,\mathrm{Pa}$. The eigenvalue for the electron temperature had the value $T_e = 35516\,\mathrm{K}$. Densities were normalised to the average electron density of $n_{e0} = 10^{15}\,\mathrm{m}^{-3}$.

The results of a numerical solution under the given conditions show axisymmetric profiles for the electron density, the ion density, and for the plasma potential. The relative low average electron density of $n_{e0} = 10^{15}\,\mathrm{m}^{-3} = 10^{9}\,\mathrm{cm}^{-3}$ is the reason why both sheath regions are clearly visible and why they have an extension of approximately 5 mm. The sheath regions are characterised by a rapid drop of the plasma potential and a significant difference between the electron and the ion density. The transition from sheath to bulk is continuous, so it is hard to identify a position which could be defined as sheath edge[3].

The plasma potential shows a peak value of 20 V, about 3 V are needed to ensure the ambipolar transport of ions through the bulk, the remaining 17 V drop in the sheath region. In the bulk region the densities of electrons and ions decrease monotonically towards the walls and

---

[3] Various publications exist [87], [85], [86] which deal with plasma sheaths. In the field of sheath theory it is common to define the position of the sheath edge at the point, where the ion velocity equals the so-called Bohm velocity i.e. $v_i = \sqrt{kT_e/m_i}$. This definition is valid in a wide range of parameters but becomes meaningless in the case of extremely high ion friction, where the ions do not reach the Bohm velocity [113].

are almost equal. In the sheath regions a significant difference between the carrier densities is visible. The electron density drops almost down to zero while the ion density at the location of the wall equals approximately 15% of the value in the discharge centre.

In the following sections, parameter variations of this demonstration example will be shown. All the results will assume the same geometry and argon as the operating gas.

5.1.4 Influence of average electron density

In the demonstration example of the previous section, a quite low value of $n_{e0} = 10^{15}\,\mathrm{m}^{-3}$ was chosen deliberately for the average electron density in order to make the transition of sheath and bulk visible. From basic theory of plasmas it is known that the so-called Debye length l_D, for single charged plasmas defined by

$$l_D = \sqrt{\frac{\epsilon_0 k T_e}{n_e e^2}}, \tag{5.11}$$

is a measure of the extension of the sheath.

Using the eigenvalue of $T_e = 35516\,\mathrm{K}$ and the average electron density of $n_e = 10^{15}\,\mathrm{m}^{-3}$ one obtains a value of $l_D = 0.41\,\mathrm{mm}$ for the Debye length. The regions where the electron and ion density differ significantly, i.e. the sheath regions, have an extension of 4-5 mm (see. Fig. 5.1). This means that in the chosen example the sheath thickness is approximately 10 Debye lengths.

Especially, for inductively driven high density sources, the assumed value of the electron density is unrealisticly low, and therefore, in this section, more realistic values will be discussed. As the Debye length is indirectly proportional to the square root of the electron density, one might assume that the sheath thickness shows the same behaviour.

In fact the sheath thickness is approximately inversely proportional to the square root of the average electron density. Sheath region for average electron densities in the range of $n_{e0} = 10^{15} - 10^{17}\,\mathrm{m}^{-3}$ are shown in Fig. 5.2. As an experimental background one might assume a variation in discharge power which causes this density variation. In order to make the results comparable, the densities were normalised to the average electron density, denoted n_{e0}. With an increasing n_{e0} the sheath size shrinks as expected. The percentage of the discharge volume, which is occupied by the two sheath layers, slightly affects the transport properties of the discharge. This can be seen by comparing the corresponding eigenvalues for the electron temperature which are a good measure for the overall particle production: In case of $n_{e0} = 10^{15}\,\mathrm{m}^{-3}$, where the sheath regions cover approximately 20% of the discharge volume, an electron temperature of $T_e = 35516\,\mathrm{K}$ had been calculated, while in case of $n_{e0} = 10^{17}\,\mathrm{m}^{-3}$ a value of $T_e = 34236\,\mathrm{K}$ is obtained. This reflects the fact that for $n_{e0} = 10^{17}\,\mathrm{m}^{-3}$ the bulk region of the discharge is about 20% larger. However, for most technical applications the influence of the average electron density on the effective discharge volume might be neglected.

A last result corresponding with the various sheath extensions should be discussed: With the sheath thickness also the value of the ion density at the outer boundary of the simulation domain decreases. This can be understood by comparing the outflow velocities with which the

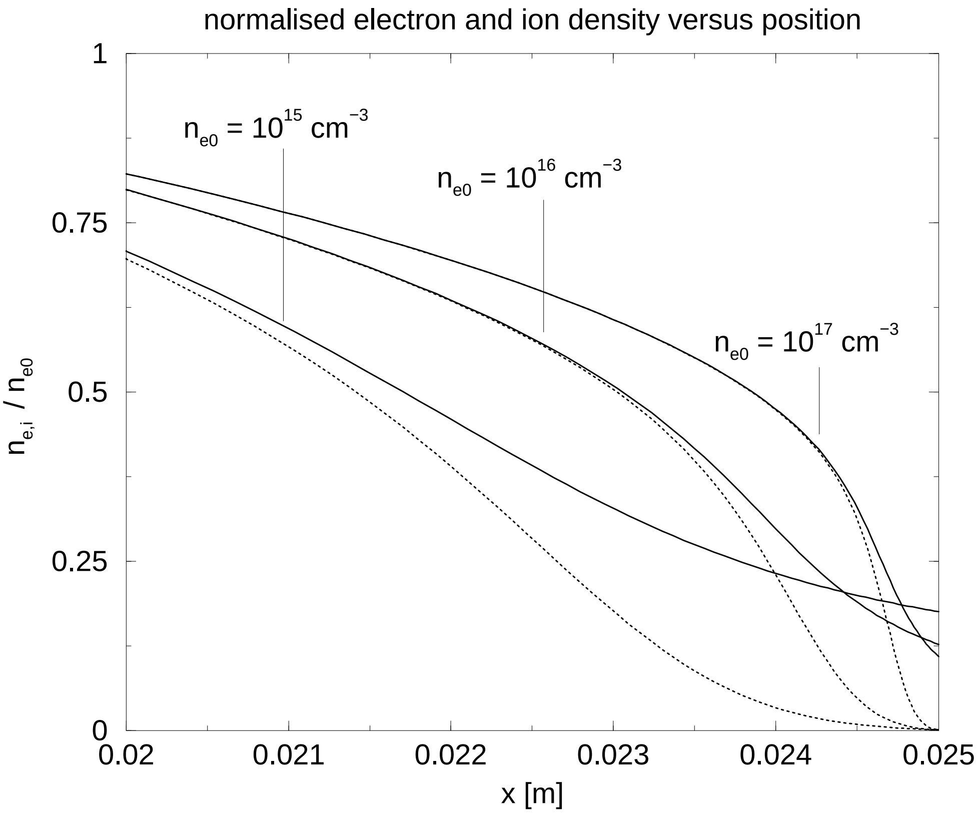

Figure 5.2: Electron (dashed lines) and ion (full lines) density normalised to the average electron density n_{e0} for various values of n_{e0}. Calculations were carried out for argon $P_N = 1\,\mathrm{Pa}$, $T_N = 300\,\mathrm{K}$.

ions leave the discharge. For the most extended sheath ($n_{e0} = 10^{15}\,\mathrm{m}^{-3}$), the ion velocity v_i has a value of $7100\,\mathrm{m/s}$, while for the sheath which is ten times thinner ($n_{e0} = 10^{17}\,\mathrm{m}^{-3}$), v_i takes a value of $9100\,\mathrm{m/s}$.

Obviously, the reason for this significant difference is the momentum loss, caused by ion-neutral collisions in the sheath region. This might surprise as the neutral gas background pressure of $p_N = 1\,\mathrm{Pa}$ can be considered as low, i.e. the electron mean free path for elastic collisions is significantly bigger than the discharge extension of $5\,\mathrm{cm}$.

5.1.5 Influence of neutral gas pressure

As the previous section already indicated, ion neutral collisions have a significant influence even in a low pressure regime. To obtain quantitative information about the importance of ion-neutral collisions, the effect of neutral gas pressure will be discussed in this section. The influence of the neutral gas pressure on the simulation result is caused by three different effects. As the impact ionisation rate is directly proportional to the density of the neutral particles, at higher pressure a lower electron temperature is required to cause the same amount of ion-electron pair production. Furthermore, with an increasing neutral particle density, the ion-neutral collisions become more frequent and slow down the ambipolar diffusion process. These are the reasons why at a higher pressure a lower electron temperature can be expected. As the ambipolar diffusion process is driven by the electron partial pressure given by $\nabla n_e k T_e$, the electron temperature has also an influence on the overall transport properties of the discharge.

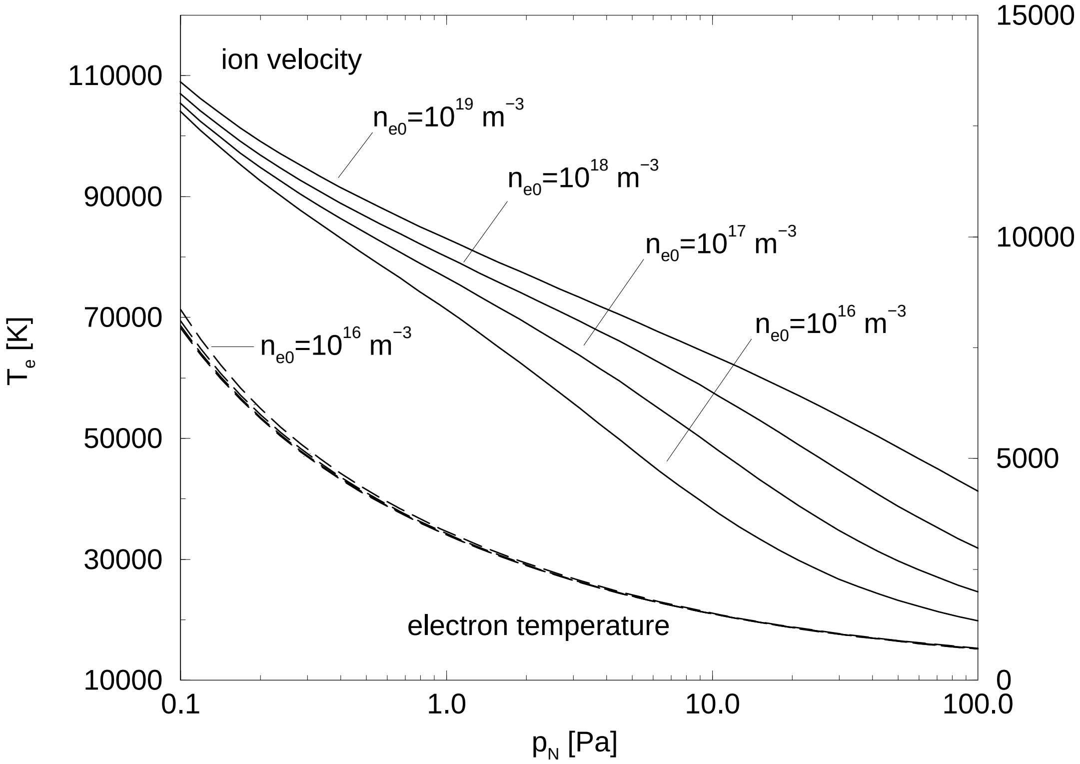

Figure 5.3: Pressure dependence of the electron temperature eigenvalue (dashed lines, left axis) and the ion velocity at the boundary (full lines, right axis). The results are shown for average electron densities n_{e0} in the range from $n_{e0} = 10^{16} - 10^{19}\,\mathrm{m}^{-3}$

These effects are illustrated in Fig. 5.3. A pressure variation over three decades causes a significant variation of the electron temperature eigenvalue from 15550 K to 77955 K. With increasing pressure, the eigenvalue of the electron temperature decreases monotonically. This correlates with a decrease in velocity with which ions reach the walls. At all the considered values of the average electron density ($n_{e0} = 10^{15} - 10^{19}\,\mathrm{m}^{-3}$), the electron temperature eigenvalue shows only slight variations. A significant influence of the average electron density on the speed with which the ions leave the discharge can be observed. The results are also shown in Fig. 5.3. The velocity shows the expected decrease with an increasing neutral gas pressure, and also a strong dependence on the average electron density n_{e0}. For a low neutral gas pressure ($p_N = 0.1\,\mathrm{Pa}$), the dependence of the ion speed on the average electron density appears to be weak. The reason is the low number of ion-neutral collisions in the sheath. With an increasing neutral gas pressure, collisions become more frequent, too. The momentum loss in the sheath region is also proportional to the sheath extension which depends on the average electron density n_{e0}. In case of the highest considered average electron density ($n_{e0} = 10^{19}\,\mathrm{m}^{-3}$), the smallest amount of momentum is lost in the sheath. Remarkably, the strongest dependence of the ion velocity on the average electron density occurs in an intermediate pressure range around 20 Pa.

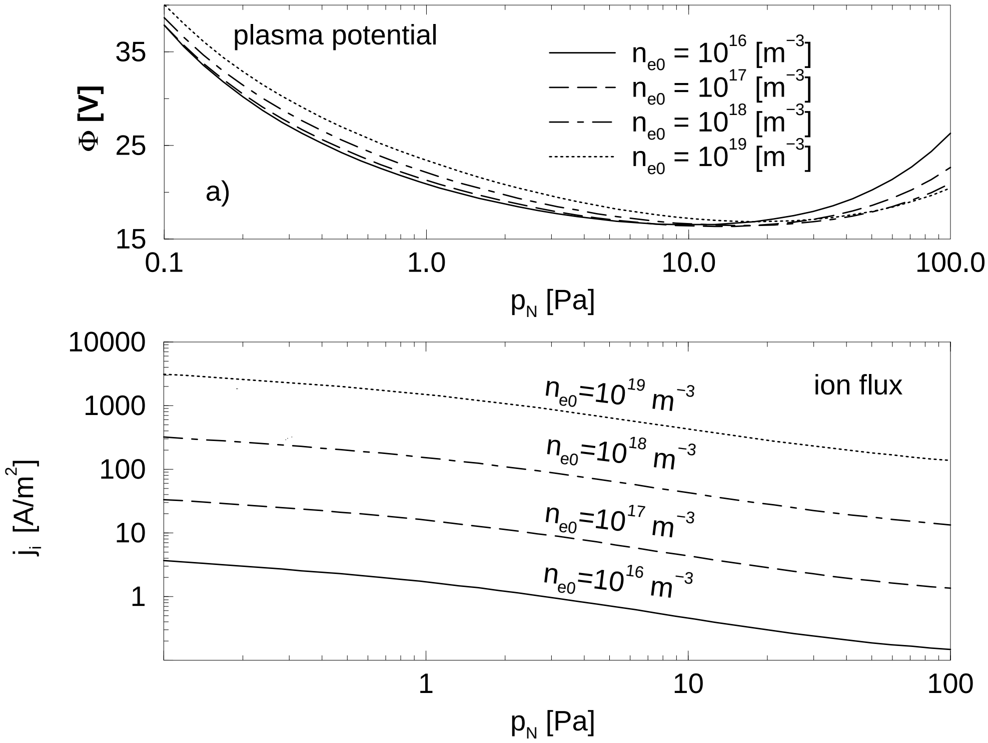

Figure 5.4: Plasma potential in the discharge centre and ion flux to the walls in a pressure range $p_N = 0.1 - 100\,\mathrm{Pa}$ at an average electron density of $n_{e0} = 10^{16} - 10^{19}\,\mathrm{m}^{-3}$.

The general decrease of the ion velocity with increasing neutral gas pressure correlates with a decreasing ion flux as shown in Fig. 5.4. At all the considered average electron densities the pressure dependent ion flux to the walls of the discharge shows identical behaviour, i.e. a monotonic decrease with increasing neutral gas pressure. Comparing the ion fluxes at a neutral gas pressure of $p_N = 0.1\,\mathrm{Pa}$ and $p_N = 100\,\mathrm{Pa}$, one can see that they differ more than one order of magnitude. An important consequence for the general energy conservation of the discharge can be derived from this result: For the case of low pressures, most of the RF-power is used for the production of ions, while for high pressure, the ion friction predominantly transfers energy to the neutral gas. This is in accordance with spectroscopic measurements [91] which determine the neutral gas temperature in dependence of neutral gas density.

The situation turns out to be more complicated, when we consider the plasma potential in the centre of the discharge. As expected, the plasma potential decreases as well as the electron temperature in the pressure range $p_N = 0.1 - 10\,\mathrm{Pa}$. At about $p_N = 20\,\mathrm{Pa}$ a minimum is reached, at higher neutral gas pressure the plasma potential rises while the corresponding electron temperature, as shown in Fig. 5.3, decreases. This behaviour can be understood, when we consider the plasma potential shape at neutral gas pressure values of $p_N = 1, 20$ and $100\,\mathrm{Pa}$, as shown in Fig. 5.5 (b).

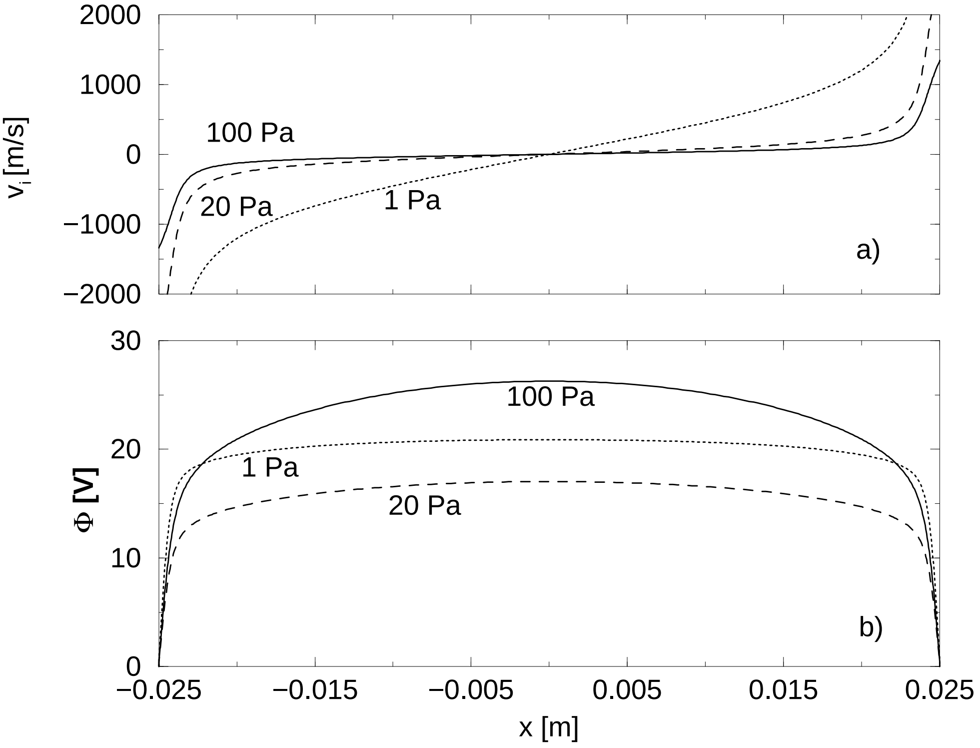

Figure 5.5: Plasma potential and ion drift velocity versus position for neutral gas pressures of $p_N = 1, 20$ and $100\,\mathrm{Pa}$ and an average electron density $n_{e0} = 10^{16}\,\mathrm{m}^{-3}$.

The shape of $\Phi(x)$ is of interest rather than the absolute value in the discharge centre at $x = 0$. For $p_N = 1, 20\,\mathrm{Pa}$ the potential profile shows a flat shape that corresponds to a potential difference of only a few volts between discharge the centre and the sheath edge. This potential difference increases with the pressure, e.g. at $p_N = 100\,\mathrm{Pa}$ a potential difference of almost ten volts is required to ensure ion transport from the discharge centre towards the sheath edge. The increase in the centre potential as shown in Fig. 5.4, can therefore be attributed to a significant ion friction in the discharge bulk which can only be compensated by an extra amount of ambipolar electric field. The losses caused by friction terms are the reason for the significantly different ion velocity profiles, as shown in Fig. 5.5 (a). In case of $p_N = 1\,\mathrm{Pa}$ a significant acceleration towards the walls takes place in the discharge bulk, at higher pressure values the ambipolar diffusion process is slowed down resulting in a very flat velocity profile. It should be mentioned that at pressure values of more than 50 Pa, the assumption of a constant electron temperature in the whole discharge is no longer valid (for the assumed discharge size). The presented results are intended to give an overview what the consequences of pressure variations over a wide range of parameters.

5.1.6 Sensitivity analysis

While in Sect. 5.1.5 the consequences of a variation of the neutral gas pressure were discussed, the question remains which model parameters were the reason for the pressure dependence. The energy with which the ions hit the walls decreases drastically with an increasing pressure. The reason is the momentum loss caused by ion-neutral collisions.

In order to understand the dependence of simulation results on input parameters, a sensitivity analysis was performed. As the strong influence of the neutral gas pressure on the ion flux and velocity indicates, the friction terms for ions are the most interesting parameters. The velocity dependence of the ion-neutral collision rate was considered by using an empirical parametrisation of the collision frequency, as given in (4.6). It can be expected, that the coefficient a_0 has dominant influence in regions of low ion drift velocity, while a_1 dominates in regions of a high drift velocity. To make the influence of the different model input parameters comparable, a set of relative and dimensionless sensitivity variables was defined:

$$S_{T0} = \frac{a_0}{T_e}\frac{\partial T_e}{\partial a_0}, \tag{5.12}$$

$$S_{T1} = \frac{a_1}{T_e}\frac{\partial T_e}{\partial a_1}, \tag{5.13}$$

$$S_{j0} = \frac{a_0}{j_i}\frac{\partial j_i}{\partial a_0}, \tag{5.14}$$

$$S_{j1} = \frac{a_1}{j_i}\frac{\partial j_i}{\partial a_1}, \tag{5.15}$$

where a_0, a_1 are the parameters which determine the velocity dependence of the ion-neutral collision rate, and T_e is the eigenvalue for the electron temperature. The defined sensitivities are a measure how strong the overall impact ionisation[4] of a model discharge depend on the parameters a_0 and a_1.

Results for the discussed argon model discharge are shown in Fig. 5.6 (a). The dimensionless sensitivities S_{T0}, S_{T1}, S_{j0} and S_{j1} have been calculated for a neutral gas pressure in a range from $0.1 - 100\,\mathrm{Pa}$ and for different average electron densities n_{e0}. As already discussed in Sect. 5.1.4, the average electron density determines the extension of the sheath regions, but has generally only little effect on the electron temperature eigenvalue. So, S_{T0} and S_{T1} show also only a slight variation for various average electron density values. However, the pressure variation shows a transition between two different regimes. In case of low pressure (for the chosen

---

[4] Please consider the strong dependence of the particle generation rate on the electron temperature as shown in Fig. 4.1.

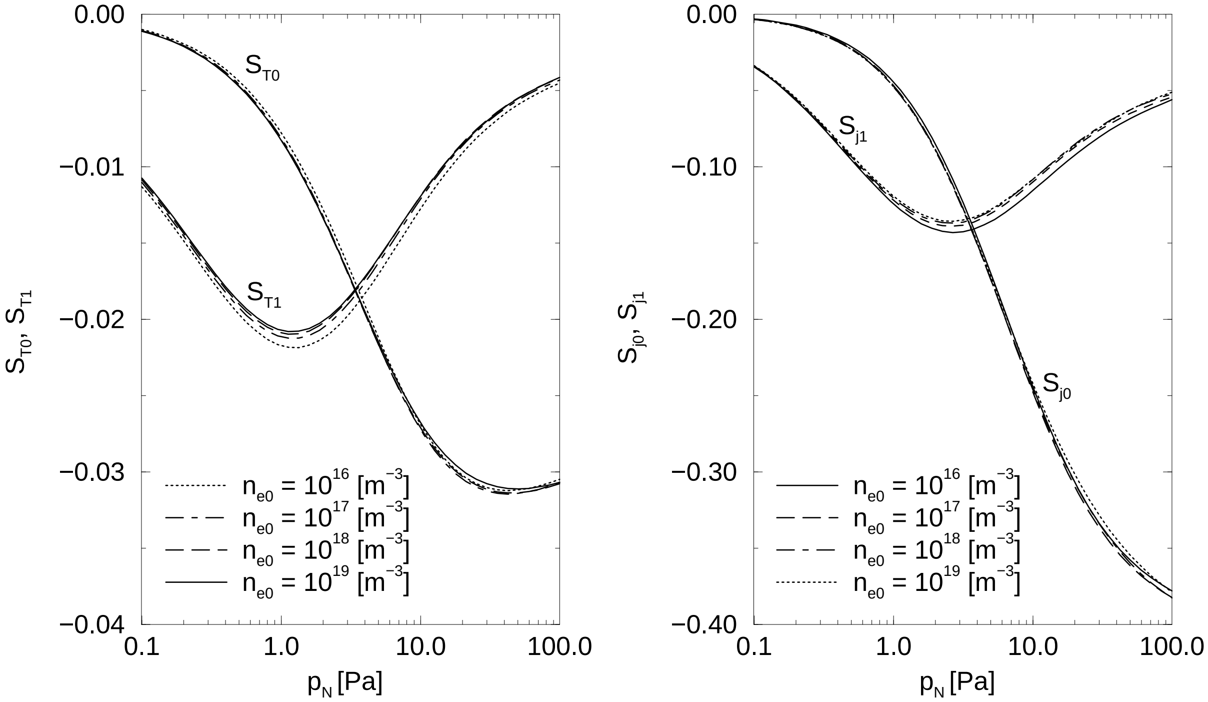

Figure 5.6: Normalised sensitivities S_{T0}, S_{T1}, S_{j0}, S_{j1} for average electron densities in the range $n_{e0} = 10^{16} - 10^{19}\,\mathrm{m}^{-3}$ and in dependence of neutral gas pressure p_N.

discharge geometry of 5 cm in the pressure range $p_N < 3\,\mathrm{Pa}$), S_{T1} is dominating. This is not surprising as the underlying parameter a_1 has influence especially for high ion drift velocities. With increasing neutral gas pressure, the ion drift velocities shrink, so the parameter a_0 becomes dominant for $p_N > 3\,\mathrm{Pa}$. The dependence of the ion flux shows similar behaviour. In Fig. 5.6 (b) the values of S_{j0} and S_{j1} are shown. The influence of the average electron density appears to be small, and for low pressure values the coefficient of a_1 dominates, while at higher neutral gas pressure the coefficient a_0 dominates. While the pressure dependence of S_{j0} and S_{j1} has a qualitatively similar shape like S_{T0} and S_{T1}, the relative sensitivities S_{j0} and S_{j1} are one order of magnitude larger. This expresses the fact that particle production by impact ionisation does react much more sensitive on changes in the ion friction terms than the corresponding electron temperature eigenvalue. This is another aspect of the steep dependence of the impact ionisation rate on electron temperature as shown in Fig. 4.1.

While for the ion flux and the electron temperature the dependence on the average electron density in the discharge is weak, a strong influence on energy and velocity of ions leaving the discharge has already been discussed (c.f. section 5.1.4). In analogy to the (5.12) - (5.15), sensitivities for ion velocity can be defined:

$$S_{v0} = \frac{1}{v_i a_0}\frac{\partial v_i}{\partial a_0}, \tag{5.16}$$

$$S_{v1} = \frac{1}{v_i a_1} \frac{\partial v_i}{\partial a_1}. \tag{5.17}$$

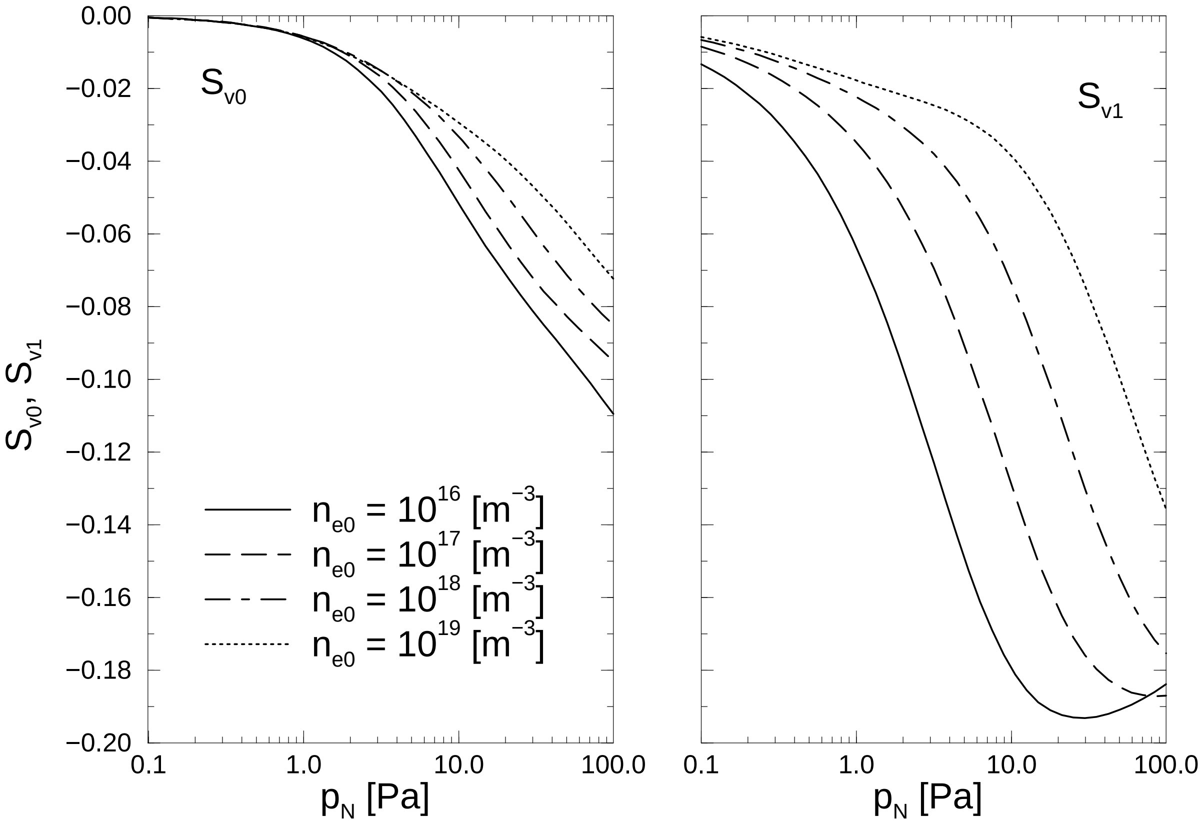

Figure 5.7: Normalised sensitivities S_{v0} and S_{v1} for average electron densities in the range $n_{e0} = 10^{16} - 10^{19}\,\mathrm{m}^{-3}$ and in dependence of the neutral gas pressure p_N.

The varying sheath extensions have strong influence on S_{v0} and S_{v1}, as Fig. 5.7 illustrates. For low pressure and all the considered average electron densities the sensitivity values are low. Over the whole pressure range from $0.1 - 100\,\mathrm{Pa}$, and for all considered average electron densities, a_1 dominates over a_0. The influence of the sheath extension is clearly visible as the sensitivity values are generally larger in case of more extended sheath regions, i.e. lower average electron density n_{e0}.

5.2 Dynamic solutions of the hydrodynamic equations

The previous section has focused on the basics of particle transport, and the idealised case of a quasi static discharge was treated. However, a number of applications exists where such an approach might be sufficiently accurate. Examples are positive columns of glow discharges, microwave or inductively driven discharges if they can be considered as one-dimensional.

However, in many cases of RF-discharges, a capacitive component exists which causes an electron oscillation driven by the RF. In this section, such cases shall be investigated.

In the previous section, ions have turned out to have a dominating influence on the transport properties. The neutral gas pressure starts to become important as soon as the collision term dominates the ion inertia.

Most results obtained for the static case remain valid for the ions in the dynamic case. Ion inertia, especially in the discharge bulk, is so dominating, that no dependence on the driving RF-frequency can be observed[5]. The transport behaviour with its dependence on the neutral gas pressure is almost the same as in the static case.

The species which reacts sensitive to the presence of RF are the electrons. An applied RF-voltage causes them to oscillate in the field, and extended sheath regions develop.

In the previous section, the differences between a model which uses only one and a model which uses two conservation equations, deliberately have not been discussed. In fact, static calculations simulation results are almost identical in case of drift diffusion and a two-moment model based on (5.1), (5.2). Electron neutral collisions included in the model by the parameter ν_{me} have almost no influence on the results for the static case.

The situation turns out to be different in the dynamic case, i.e. when electric fields exist which vary with the RF-frequency of the discharge. Electron inertia can have an influence so that the drift-diffusion approximation and the two-moment model show visible differences. In this section, both model approaches will be compared. While the existence of static solutions depends on static boundary conditions, it was assumed for the following calculations that a sinusoidal voltage is applied to the (conducting) boundaries of the discharge. As a consequence, the corresponding solutions are time dependent but periodical.

The concept of a given average electron density and a corresponding eigenvalue for the electron temperature has to be partially given up as a strict implementation would cause drastic changes in the eigenvalue over one RF-period. However, in a time averaged sense it is still possible to provide an (spatially and over one RF-period) averaged electron density and to calculate a corresponding eigenvalue for electron temperature.

Whether electron inertia has to be considered or whether a drift diffusion approach provides a sufficiently accurate model, depends on the specific application. One example, where electron inertia plays an important role, is the so-called SEERS[6] effect [48], [47]. The nonlinearities of the sheath regions of capacitively coupled plasmas in combination with the electron inertia in the discharge bulk generate oscillations in the plasma. These oscillations might be used for calculating discharge parameters like electron density or collision frequencies. In Sect. 5.2.3 an example will be presented, demonstrating that such an effect can only be understood by using an appropriate model.

---

[5] This is not strictly true in case of sheath regions. Especially for light ions, a modulation of the ion current is possible and has been predicted, for example in [97] and [74].

[6] Self Excited Electron Resonance Spectroscopy

5.2.1 Comparison of drift diffusion and two-moment model

Inertia terms become important in the case of strong alternating fields which force the electrons to oscillate. This is typically the case in capacitively coupled discharges. The average extension of the sheath regions is much larger than in the static case. The sheath thickness is oscillating with the driving RF frequency. However, the discharge bulk remains almost quasi neutral. Typical for RF-discharges is also the high potential drop between the bulk and the walls bounding the discharge. For technological purposes, this is often a desired effect, as the potential difference causes a directed bombardment by positive ions of all the surfaces which are exposed to the plasma.

In order to perform a direct comparison of drift diffusion model and two-moment model, a homogeneous electron temperature is assumed to exist in the whole simulation region. The corresponding eigenvalue for this temperature is determined by the assumption of an invariant period averaged electron density.

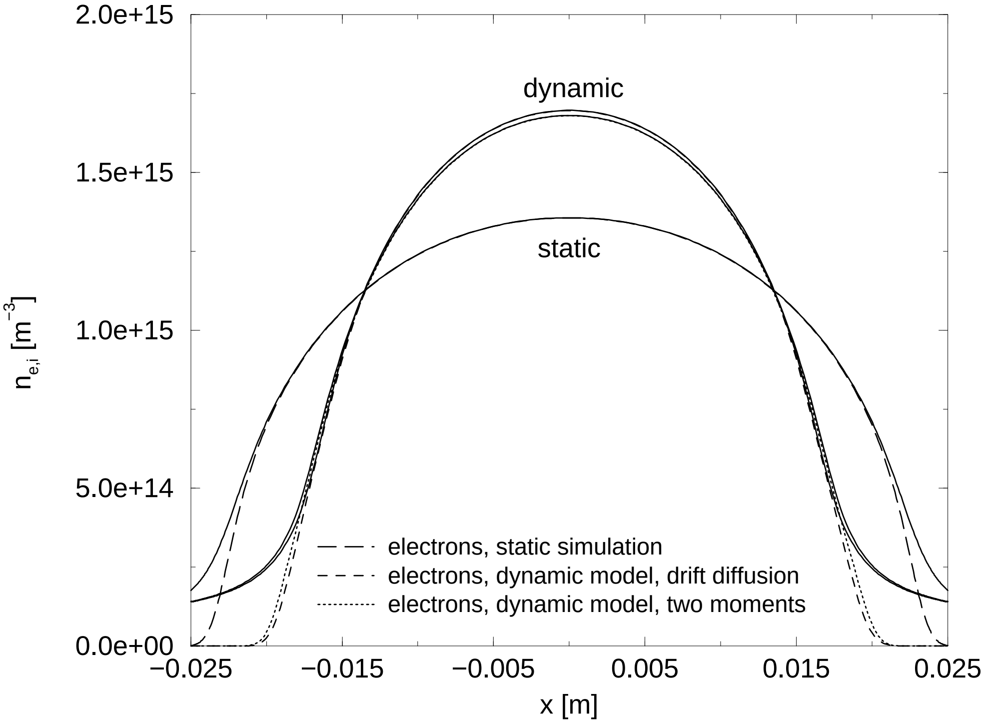

Figure 5.8: Comparison of static simulation results with dynamic calculations using a drift diffusion and a two-moment model for an argon discharge, operating at 1 Pa. Dashed, dotted and long dashed lines represent electron densities, the full lines the corresponding ion densities. $f_{RF} = 27\,\mathrm{MHz}, A_{RF} = 200\mathrm{V}$

The calculations were carried out for an argon discharge, operating at 1 Pa, the potential of the right boundary was assumed to be zero while the potential of the left boundary varied with a sinusoidal time dependency: $\Phi(t) = A_{RF}\,\sin(2\pi f_{RF}\,t)$. The amplitude of the RF-oscillation was set to a value of $A_{RF} = 200V$ and the common RF-frequency of $\omega = 27\,\mathrm{MHz}$ was used. The results for the different models are shown in Fig. 5.8. For comparison, the electron and ion density in case of a static calculation, i.e. without applied RF-voltage, as well as electron and ion density for the dynamic model are shown. The electron and ion densities in the dynamic case are shown for a time, when the phase of the RF is zero, i.e. $f_{RF} \cdot t \in \{0, 1, 2, 3, ...\}$.

All the shown results are calculated in case of an average electron density of $n_{e0} = 10^{15}\,\mathrm{m}^{-3}$. As the sheath regions are much larger for the dynamic case (i.e. with applied RF-voltage), the peak electron densities differ significantly. However, the two different dynamic models only show very small differences.

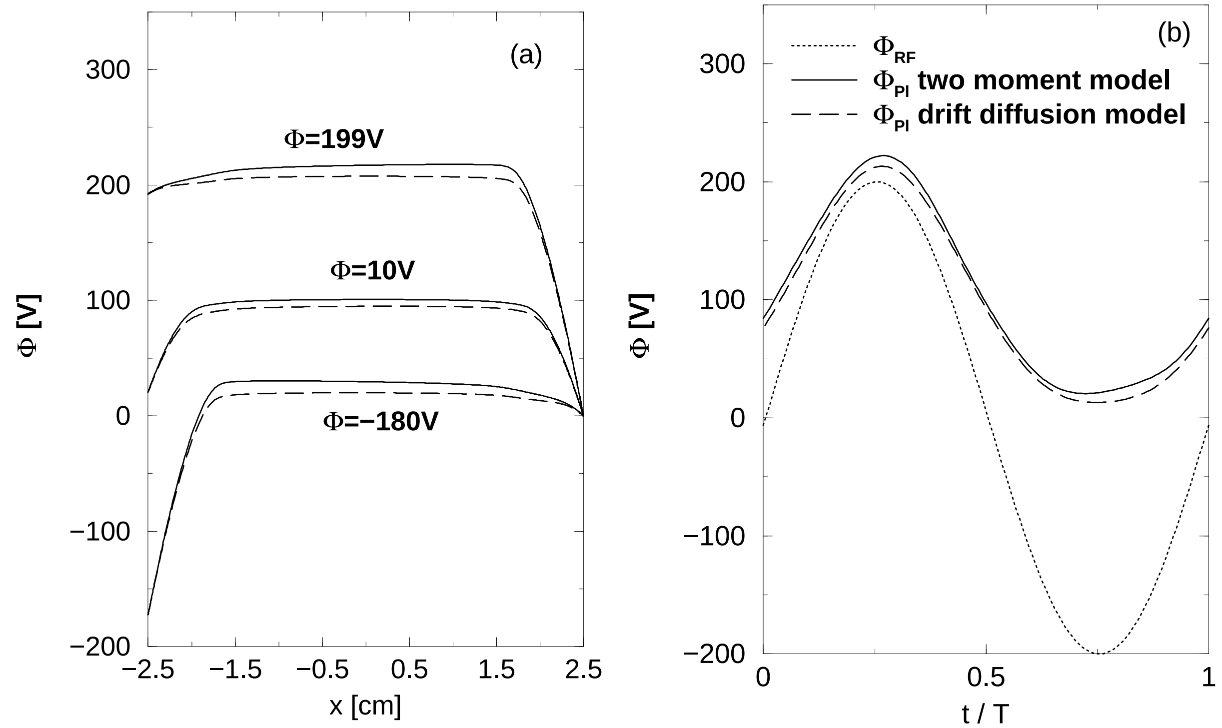

Figure 5.9: Potential distributions for two-moment and drift diffusion model. The left figure shows the spatial potential distribution in the discharge at different phases, the right figure displays the time dependence of the potential in the discharge centre.

When we compare the potential distributions, the essential differences between the drift diffusion and two-moment model become visible. In 5.9 (a) the potential in the discharge for three selected RF-voltages is shown. It is remarkable that the two-moment approach generally shows a slightly higher potential than the corresponding drift diffusion calculation. Furthermore, in the bulk region of the discharge the potential is almost flat in the case of the drift diffusion model, while in some cases the two-moment model predicts a potential gradient. The reason herefore is the electron inertia. In order to accelerate the bulk electrons, a certain amount of the electric field, i.e. potential gradient, is required. With a changing sign of the RF-voltage the direction of this gradient also changes, as indicated by the curves for $\Phi = 199$ V and $\Phi = -180$ V.

The modulation of the potential in the centre of the discharge i.e. the plasma potential Φ_{pl} is shown in Fig. 5.9 (b). If the potential of the driven electrode is positive, the plasma potential follows with an offset voltage in the order of a few ten volts. If the electrode potential turns negative, a significant voltage drop develops. It is remarkable that the plasma potential in the discharge center is not sinusoidal. Deviations from a sinusoidal voltage are pronounced for the case of the two-moment model but also visible for the drift diffusion model. A slight phase shift between driving RF-frequency and the plasma potential is also visible for both models.

However, the overall differences between the two model approaches can be considered to be small. The effect of inertia terms is visible, but does not cause the two models to differ drastically. This is true for a wide range of average electron densities, therefore no further parameter variations are carried out. Instead, some further consequences of the sheath nonlinearity will be discussed.

5.2.2 Asymmetric discharges, self bias

In many cases a CCP discharge consists of a small electrode which is usually driven by RF while the counterelectrode (the walls of the reactor chamber) is larger in size. Typically, the RF-generator and the driven electrode are connected by a capacitor so that no DC current from the electrode flows to the plasma. During operation, a negative charge accumulates on the electrode exposed to the plasma, which is known as the so-called self bias. A more detailed description and scaling laws relating the self bias voltage to the area ratio of the electrodes, can be found in [63].

The self bias is a desired effect, particularly for applications (e.g. dry etching) depending on energetic, directed ions hitting the substrate surface. The self bias voltage is the reason why ions are accelerated towards the electrode, while electrons are repelled for most of the time of an RF-cycle. Only for a very short part of the RF-cycle, the potential barrier is reduced so much that electrons can reach the electrode. As the electronic thermal velocity of the electrons is typically about two orders of magnitude larger than the velocity of ions leaving the discharge, the short period, when electrons can reach the electrode, is sufficiently long to compensate the permanent ion flux. As already discussed in the previous subsection, the RF causes a periodic change in the plasma potential (see Fig. 5.9). On the other hand, to what extent the driven electrode is able to modulate the plasma potential, depends on the geometry, i.e. on the area ratio of the electrode to the counterelectrode.

A possibility to use a one-dimensional model in order to investigate this effect is to assume a cylindrical or spherical geometry. In a realistic setup the discharge would consist of a cylindrical volume in which a driven electrode with a certain diameter is inserted. The length of the discharge should be significantly larger than the diameter of the outer boundary. An alternative possiblity is the use of a spherical geometry as proposed in [63]. In that case, both electrodes are assumed to be spherical, the small driven electrode is included in a larger grounded shell.

The calculated values of the plasma potential in equal distance from both electrodes for a cylindrical setup with three different radii r_e of the inner electrode are shown in Fig. 5.10. In all the cases, the outer electrode had a radius of 10 cm. Results are presented for inner electrodes

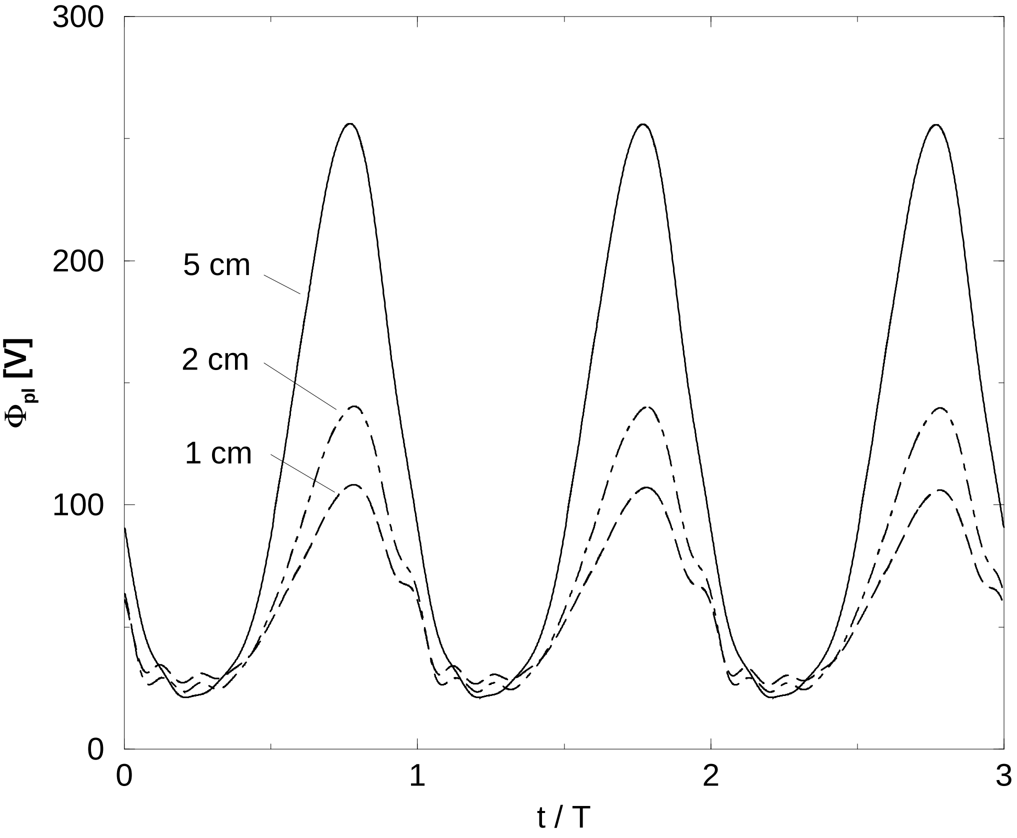

Figure 5.10: Plasma potential versus time for asymmetric RF-discharges. The results are shown for argon, $p_N = 1\,\mathrm{Pa}$, $A_{RF} = 500\,\mathrm{V}$, $f_{RF} = 27\,\mathrm{MHz}$.

with a radius of $1\,\mathrm{cm}$, $2\,\mathrm{cm}$ and $5\,\mathrm{cm}$. The inner electrode was driven while the outer electrode was grounded. It is not surprising that the modulation of the plasma potential Φ_{pl} increases with the area of the driven electrode. The maximum value rather than the minimum are influenced by the area of the driven electrode. By subtracting the maximum value of the plasma potential from the amplitude A_{RF}, which drives the discharge, one obtains an approximate value of the bias voltage. $V_{bias} = 245\,\mathrm{V}$ for $r_e = 1\,\mathrm{cm}$, $V_{bias} = 360\,\mathrm{V}$ for $r_e = 2\,\mathrm{cm}$ and $V_{bias} = 395\,\mathrm{V}$ for $r_e = 5\,\mathrm{cm}$. Higher bias voltages for smaller driven electrodes are in accordance with well known theories about self bias voltages [63].

Another remarkable detail is the occurance of high frequency oscillations which are especially pronounced for small driven electrodes, i.e. for highly asymmetric discharges. Such variations are particularly pronounced in asymmetric discharges which operate in a low pressure regime and at high RF voltages. Those oscillations can in fact be measured and used to perform non-invasive diagnostics of the discharge. This will be the topic of the following section.

5.2.3 Self Excited Electron Resonance Spectroscopy (SEERS)

In recent years, the manufacturers of semiconductors have showed an increasing interest in process monitoring and control. Different diagnostic methods have been tested [101] under real process conditions and can be expected to be part of plasma processing equipment in the future. For the manufacturer, it is desirable to know the electron density in the process plasma while the process must not be influenced by the diagnostic system. For this reason, the use of Langmuir probes is considered to be inapplicable for the highly sensitive semiconductor processing equipment. Furthermore, coating or etching plasmas make the operation of a probe in real process plasmas difficult. The risk of contamination is another commonly used argument against probes in semiconductor applications.

It is possible to determine average electron density with passive and non invasive systems. This can be achieved by the detection of higher harmonics generated by the plasma itself. In capacitively driven and non symmetric discharges, a combination of a nonlinear sheath characteristic and electron inertia in the bulk, generate a sequence of higher harmonics which can be measured by using a passive sensor integrated in the chamber wall. A commercially available system[7] exploits these effects and offers process monitoring.

The underlying theory is based on a lumped circuit model of the discharge consisting of diodes, capacitors, inductors and resistors. The values for the lumped elements have to be derived from geometry data using semiempirical relations.

A more physically rigorous approach is the use of a hydrodynamic model to describe the sheath-bulk interaction. In this section corresponding results will be presented.

As already shown in the previous section, the capacitive operation of a discharge causes a time-dependent modulation of the plasma potential. Under certain conditions the plasma potential might show even oscillations with a frequency which is higher than the RF-frequency powering the discharge. This correlates with a modulation of the electric field at any surface exposed to the plasma. A change in time of the electric field causes a displacement current. The net current to all electrodes in the plasma is a superposition of electron, ion, and displacement current. While the ion current contributes an almost constant offset, electrodes reach the wall only at the very short period where the potential difference between plasma and wall is small enough. A numerical analysis or a simple estimation reveal that the displacement current is the dominant component.

A direct measurement of the displacement current is possible by using a passive sensor consisting of a conducting area in contact with the plasma connected to a shunt resistor. As the displacement current is the time derivative of the electric field, high frequency components are amplified proportionally to their frequency. Higher harmonics become clearly visible.

Basically, SEERS (Self Excited Electron Resonance Spectroscopy) might be understood, using a simple model based on splitting the discharge into bulk and sheath regions. Generally, the sheath regions show a capacitive behaviour as a voltage change causes electrons to leave or to re-enter the sheath region and drives a current. The bulk shows inductive behaviour because an applied voltage causes a change in current. The connection of bulk and sheath forms a circuit with the ability to oscillate.

---

[7] HERCULES, a system based on high frequency electron resonance current low pressure spectroscopy.

From a modelling point of view, the use of a two-moment model is a must to solve this problem. The electron inertia in the bulk plays an important role and therefore has to be included in the model. Experimental evidence shows that electron resonances are most pronounced in asymmetric systems, i.e. in discharges where one electrode is (much) smaller than its counter electrode. In order to achieve an asymmetry in analogy to the results presented in the previous section, a one-dimensional model for a cylindrical geometry can be used.

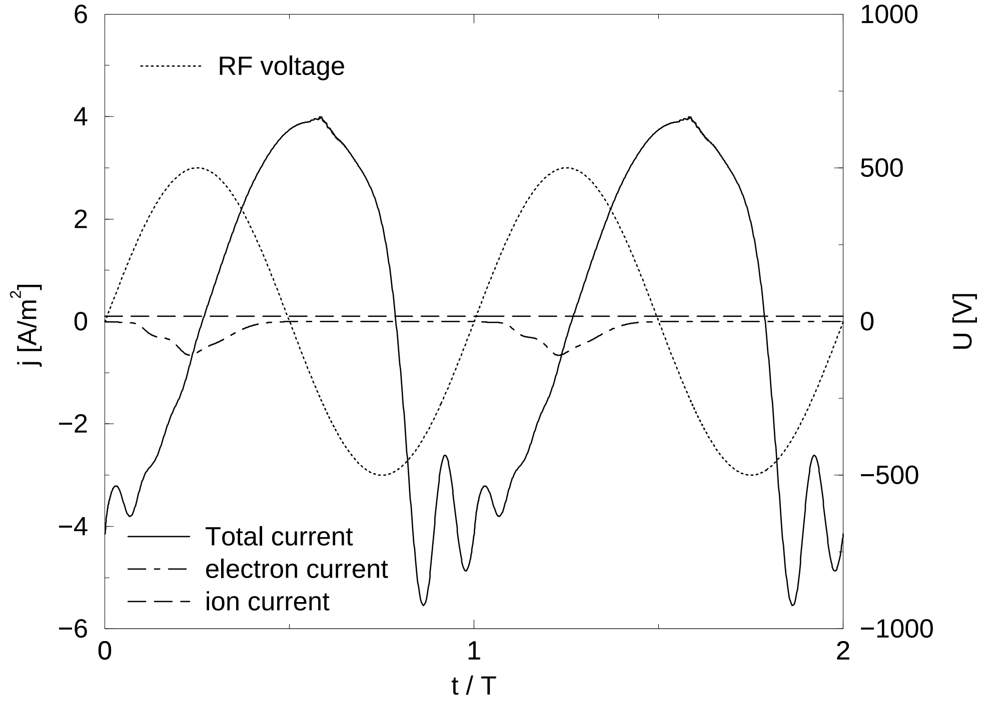

Figure 5.11: Calculated current (left scale) flowing to the grounded electrode of an asymmetric 13.56 MHz argon discharge. Neutral gas pressure was $p_N = 1\,\mathrm{Pa}$, the driven inner electrode had a radius of $r_i = 1\mathrm{cm}$ the grounded outer electrode a radius of $r_a = 10\,\mathrm{cm}$. The sinusoidal voltage V_{RF}, driving the discharge, is shown as dotted line (right scale).

The current to the grounded outer wall of the discharge in case of an argon discharge operating at a neutral pressure of $p_N = 1\,\mathrm{Pa}$, is shown in Fig. 5.11. The total current consists of three components: An ion current which appears to be almost constant, an electron current which only reaches the electrode when the sheath is almost collapsed, and a dominating displacement current. The displacement current shows a periodic structure (RF-period of the driving frequency) as well as higher order harmonics.

Electrons only contribute to the total current when the RF-voltage V_{RF}, applied to the inner electrode is sufficiently negative. The electron current appears to be slightly different for rising and for falling V_{RF}. The electron flux on time average is balanced by an ion flux which for the chosen scale appears to be almost constant. However, the potential variations in the sheath region cause a slight modulation of this ion current in the order of of few percent. Because the displacement current is almost equal to the total current in the largest part of the RF-cycle, it is not displayed separately in Fig. 5.11. The displacement current shows clearly visible oscillations which occur once V_{RF} has passed this maximum, i.e. when they are triggered by a reversal of the displacement current.

The oscillations appear to be damped and one can expect a pressure dependence which means that a higher damping occurs with an increasing neutral gas pressure.

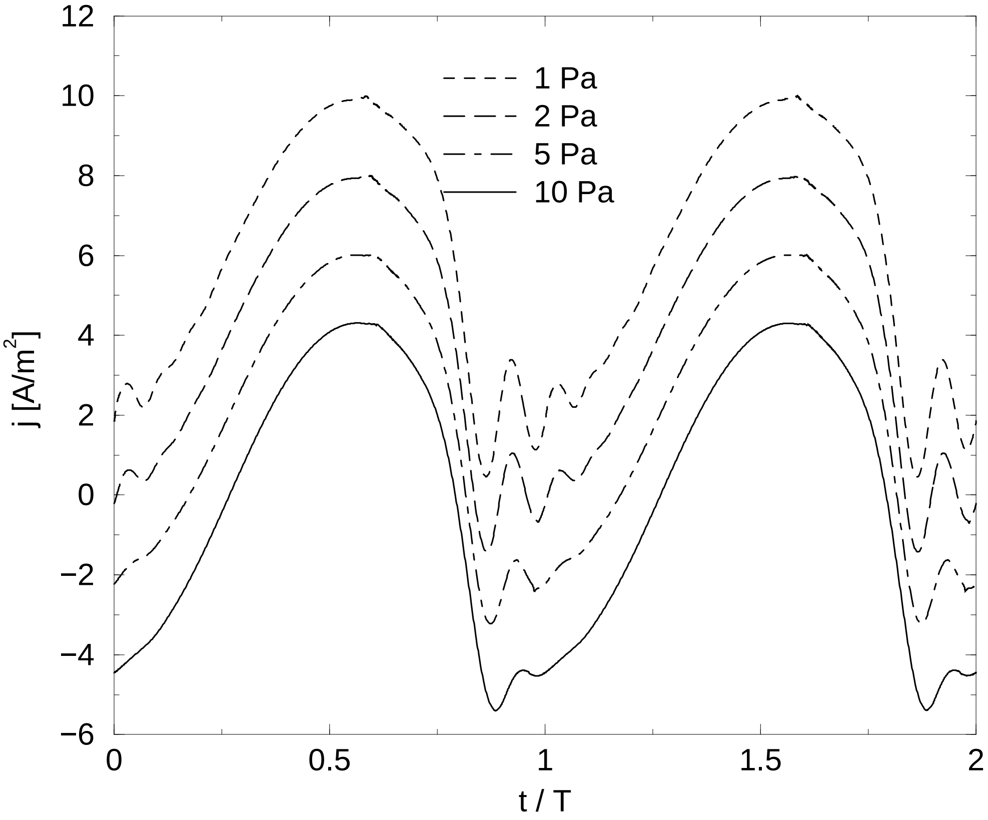

Figure 5.12: Calculated total current flowing to the grounded electrode of an asymmetric 13.56 MHz RF discharge. Results are shown for an argon discharge, operating at neutral gas pressure in the range $p_N = 1\,\mathrm{Pa} - 10\,\mathrm{Pa}$. For better distinction, the curves for 2 Pa, 5 Pa, 10 Pa are shifted 2, 4, and 6 $\mathrm{A/m^2}$, respectively.

A pressure variation leads to results as shown in Fig. 5.12. Under the asspumtion of constant electron density, the total current was plotted versus time. The pressure variation predominantely affects the damping of the oscillations while the frequency remains constant. This is especially remarkable as a variation of the neutral gas pressure has a strong influence on the eigenvalue of the electron temperature (c.f. Sect. 5.1.5).

The damping of electron resonances is an important example, where the electron-neutral momentum transfer frequency ν_e has a clearly visible influence. Normally, the ion-neutral collisions determine the efficiency of an ambiplor diffusion process, while due to the small electron mass the electronic friction can be neglected. In case of electron resonances which typically occur with frequencies of several ten MHz, the damping caused by electron-neutral collisions, is the dominant effect. As the discussed oscillations are a pure electronic effect[8], damping can only be caused by electronic collision processes. Performing non-invasive plasma diagnostics by monitoring the displacement current, the damping can be used to calculate the frequency of the momentum exchange between electrons and neutrals. Experimental evidence shows that the derived quantity tends to react sensitively on changes in the process conditions [101].

However, the quantity with dominant influence on important process parameters like ion fluxes or the production of chemically active species is the electron density.

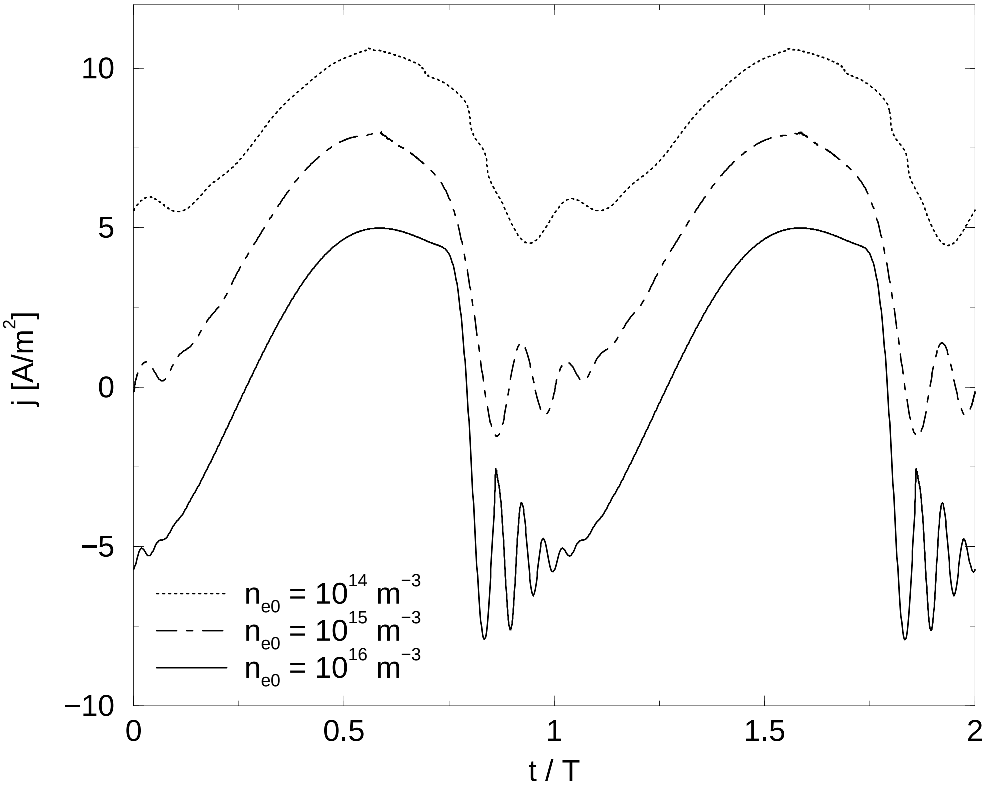

Figure 5.13: Calculated current flowing to the grounded electrode of an asymmetric 13.56 MHz argon discharge. Results are shown for an argon discharge, operating at neutral gas pressure of $p_N = 1\,\mathrm{Pa}$. The average electron density n_{e0} in the discharge was varied in the range $10^{14}\,\mathrm{m}^{-3} - 10^{16}\,\mathrm{m}^{-3}$.

The average electron density in the discharge bulk is also a measure for the number of

---

[8] Typically, the plasma frequency of ions is at least one order of magnitude lower, which means that ions do almost not react to the changes of the electric field.

electrons in the sheath regions of the discharge. The sheath regions show a capacitive behaviour, i.e. a change in voltage results in a current, which is proportional to the number of electrons in the sheath region. Considering the sheath capacitance to be dependent on the electron density and keeping in mind that electron resonances are generated in an LC-tank circuit, the frequency of those resonances depends on the average electron density in the discharge.

A change in the electron density has two effects: The inductance of the bulk is inversely proportional to the electron density, i.e. a larger electron density means smaller inductance. On the other hand a larger electron density causes a smaller Debey length, and therefore an increased sheath capacitance. Because the Debey length is proportional to the square root of the electron density, the influence of the electron density on the bulk inductance dominates. A higher electron density means a higher resonance frequency.

This dependency is illustrated in Fig. 5.13, where the total current flowing to the grounded wall is shown for different average electron densities in the discharge. In all presented calculations a neutral gas pressure of $1\,\mathrm{Pa}$ was assumed.

In case of an average electron density of $n_{e0} = 10^{16}\,\mathrm{m}^{-3}$, approximately six full cycles can be identified, while for an average density which is one order of magnitude lower ($n_{e0} = 10^{15}\,\mathrm{m}^{-3}$) only three cyles are visible. In the case of an extremely low average electron density $n_{e0} = 10^{14}\,\mathrm{m}^{-3} = 10^{8}\,\mathrm{cm}^{-3}$, the resulting electron resonance frequency is so low that only one cycle can be identified.

The results, shown in Fig. 5.13, illustrate the merits as well as the limitations of electron resonances. The damping of the electron resonances appear to be independent of the electron density, and to depend only on the neutral gas pressure.

A value of $n_{e0} = 10^{14}\,\mathrm{m}^{-3} = 10^{8}\,\mathrm{cm}^{-3}$ seems to be the low detection limit. The frequency of the self excited electron resonances is so low that only one cycle can be identified at a background pressure of $p_N = 1\,\mathrm{Pa}$. On the other hand this is not a serious disadvantage. Electron density and neutral gas pressure in a capacitive discharges, used for semiconductor production processes, are typically in an order of magnitude, which makes an evaluation of resonances in the displacement current possible.

Chapter 6

2-D Results

Various possibilities of the application of hydrodynamic transport models have been discussed in the previous chapter. In order to separate different effects and to discuss the influence of the inherent parameters, one-dimensional models are the optimal choice. Unfortunately, for realistic applications like process plasmas, where especially the question of discharge homogeneity is of interest, the use of one-dimensional models is not adequate.

As the especially for dynamic calculations, even for a simple looking one-dimensional problem the computational effort can be quite high, calculations in the two-dimensional case are only possible with optimised and efficient models. One possibility is the use of the drift diffusion model for electrons, because it tends to be much more stable in combination with larger time steps. The number of discretisation points is a critical quantity. A static calculation for a two-dimensional mesh with about 5000 grid points on-state-of-the-art personal computers may be performed in a few hours. Static means that, instead of time-dependent quantities, period averaged quantities are calculated. The number of 5000 grid points is not exceptionally high, for more complicated geometries are even more points required.

In this chapter, calculations and experimental data measured in inductively coupled discharges, will be presented. It will be shown how modelling can contribute to reactor design and how the chamber design influences key parameters like homogeneity and ion flux. As a model system for all following calculations, the equations (2.22), (2.24), (2.26), (2.31), (2.32), (2.46), and (2.48) are used.

One of the fundamental issues in ICP design is the geometry of the RF-antenna. The induced electric field, which is radiated from the antenna, decreases rapidly with increasing distance from the coil. Heating in this type of discharge only takes place in small zones localised in the proximity of the coil. That is the reason why, except for the case of very low pressure[1], an at least two-dimensional model is required, in order to calculate a realistic electron temperature distribution.

---

[1] At low pressures, the high electronic heat conductivity is the reason why the electron temperature is almost homogeneous.

6.1 Antenna design

A typical planar, cylindrical ICP chamber with three coils and the corresponding strength of the induced electric field is shown Fig. 6.1. The induced electric field shows maximum values at the location of the coils and decreases rapidly with increasing distance from the coils. In the setup shown here this has the consequence that a heating of the plasma only takes place in a region directly below the quartz window. The chosen input power of 200W represents a typical value of ICP discharges. In the following, the question of discharge power will be discussed in more detail.

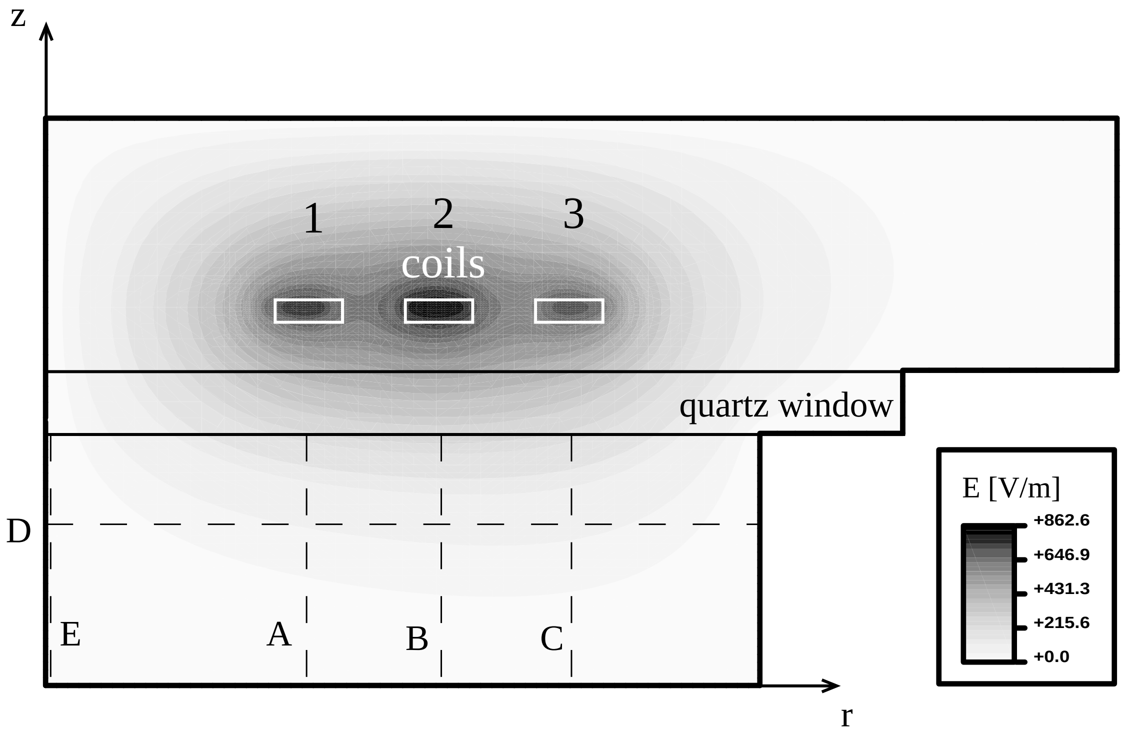

Figure 6.1: Cross section of a cylindrical ICP chamber with three coils and the corresponding induced electric field lines. The chamber has a diameter of 20 cm and a height of 4 cm. The field distribution shown is valid at an argon pressure of 5 Pa and at a discharge power of 200 W. The corresponding current flowing in each of the three coils was 6.6 A.

The dashed lines represent cutlines for which data will be presented in the following.

6.1.1 Influence of coil geometry

Starting point for all the following results is the field distribution in the unperturbed case, i.e. without a conducting plasma in the reactor chamber. In order to find out what the contribution of each single coil is, we start our considerations by calculating the induced electric field which is produced by each of the three coils. This quantity in dependence of the axial coordinate z is presented in Fig. 6.2. Data are shown for axial cuts along the cutlines A,B, and C (c.f Fig. 6.1). In all the cases the maximum of the field is located at $z = 40\,\mathrm{mm}$, i.e. on the border of the quartz window. For each cutline the dominant contribution to the field stems from the coil which is located directly above. However, a geometry effect is visible: Comparing the contribution of coil "3" to the field at cutline A with the contribution of coil "1" to the field at cutline "C", one can see that the induced field depends on the diameter of the coil. The influence of coil "1", the coil with the smallest diameter, is about 50% less than the influence of coil "3" which is twice as large.

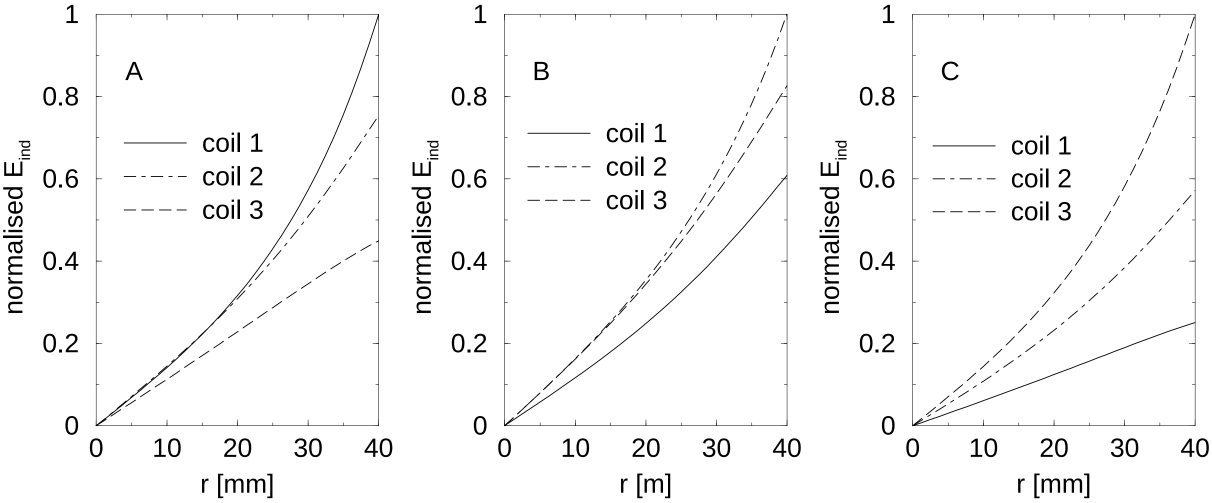

Figure 6.2: Normalised induced electric field E_Θ in dependence of the axial position z. (A) shows the field intensity along the cutline A (c.f. Fig. 6.1) in case that coil "1","2" or "3" are driven. (B), (C) show the same result for the cutlines B and C.

The attenuation of the field intensity with increasing distance from the coils appears to be unavoidable. The homogeneity of the field distribution in radial direction is more important. The variation of the induced electric field in radial direction is shown in Fig. 6.3.

The field of each coil shows a maximum whose position is correlated with the position of the corresponding coil. Due to rotational symmetry, the field vanishes on the axis of the chamber ($r = 0$). The assumption of a conducting outer boundary causes a zero field at $R = 100\,\mathrm{mm}$. If all three coils work instantaneously, the superposition produces a field distribution which is shown as full line.

The similarity of the total field distribution and of the up scaled field distribution of coil "2" is remarkable. The field distribution, generated by a superposition of the three parts, is only slightly wider than the induced electric field, produced by coil "2" on its own. This reflects one of the fundamental problems with the design of antennas: The field distribution produced by a set of coils which are driven with the same current, is often not significantly more homogeneous than the field distribution which is caused by a single coil. In any case, the induced field on the

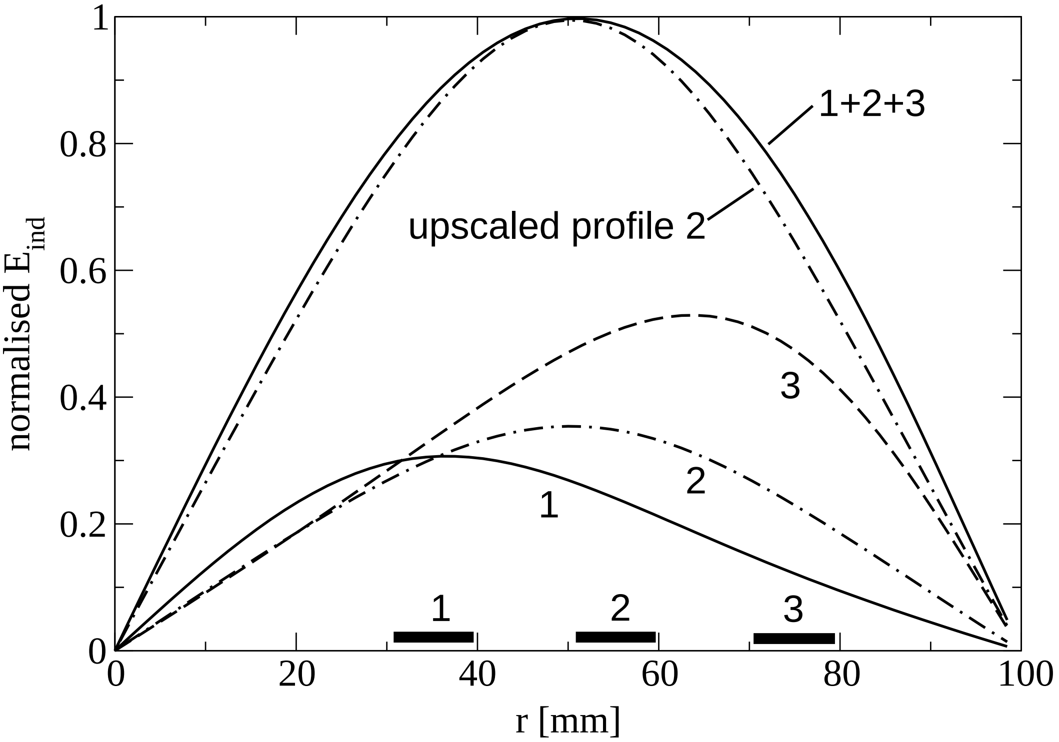

Figure 6.3: Induced electric field E_Θ along cutline D in case of a separate operation of the coils “1”, “2”, “3” and for the case of simultaneous operation “1+2+3” (full line). For simultaneous operation an in-series connection was assumed, i.e. equal current in all coils. The bars close to the r-axis indicate the position of the coils.

axis of symmetry as well as at the outer boundary vanishes.

This means that a heating can only take place in a torus shaped region. For any rotationally symmetric chamber, a zone close to the axis exists, where no induced electric field exists, and therefore no discharge heating takes place. Depending on the chamber geometry, the non heated zone will have influence on the density distribution and might result in a torus shape electron density distribution, as will be shown in the following section.

The presented results of the induced electric field agree qualitatively well with the measurements performed by Hopwood [41].

6.1.2 Experimental validation

In order to find a correlation between the induced electric field and the electron density, experiments with separately powered coils were carried out in the chamber shown in Fig. 6.1.

Langmuir probe measurements along the line, denoted as D, provided information about the electron density variation in radial direction.

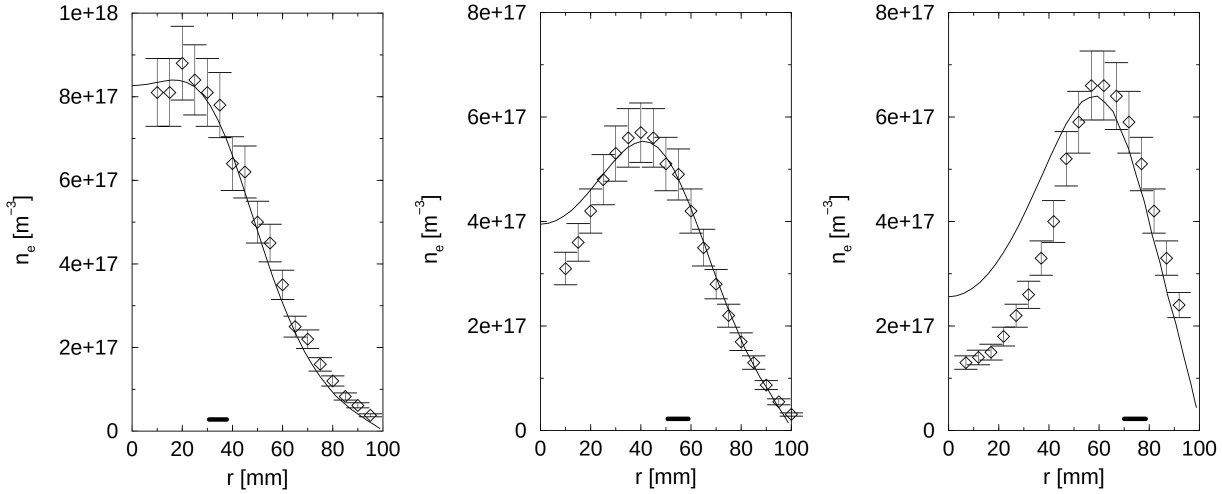

Figure 6.4: Experimental and theoretical radial electron density profiles of a planar ICP discharge (see Fig. 6.1) operating in argon at $p_N = 10\,\mathrm{Pa}$, $T_N = 300\,\mathrm{K}$. The three coils were powered separately, the bars indicate the coil positions.

The calculated and measured results are shown in Fig. 6.4. The neutral gas pressure of 10 Pa was chosen because at this pressure for the given chamber dimensions a correlation of the coil position and the electron density becomes visible. The electron densities for each of the three coils show pronounced maxima whose positions on the r-axis are located close to the coils. Simulation and experiment are in good agreement. The applied hydrodynamic model seems to be capable of predicting the local density distribution.

6.1.3 Skin effect

In a general case, the field distribution will significantly depend on the electrical conductivity of the plasma in the chamber. This conductivity is proportional to the electron density (c.f Sect. 2.3). Assuming a proportionality between input power and electron density this means that for low input power, i.e. low electron density, the field distribution in the chamber will be approximately equal with the undisturbed distribution. At a high input power, a high conductivity reduces the skin depth, and an induced electric field only exists in a thin layer below the quartz window.

The field distributions which illustrate the skin effect for an argon discharge operating at 5 Pa and with variable input power, are shown in Fig. 6.5. In that case each coil was driven with the same current. The coil current was adjusted so that the total power transferred to the plasma equals 100, 400, 1600 or 6400W.

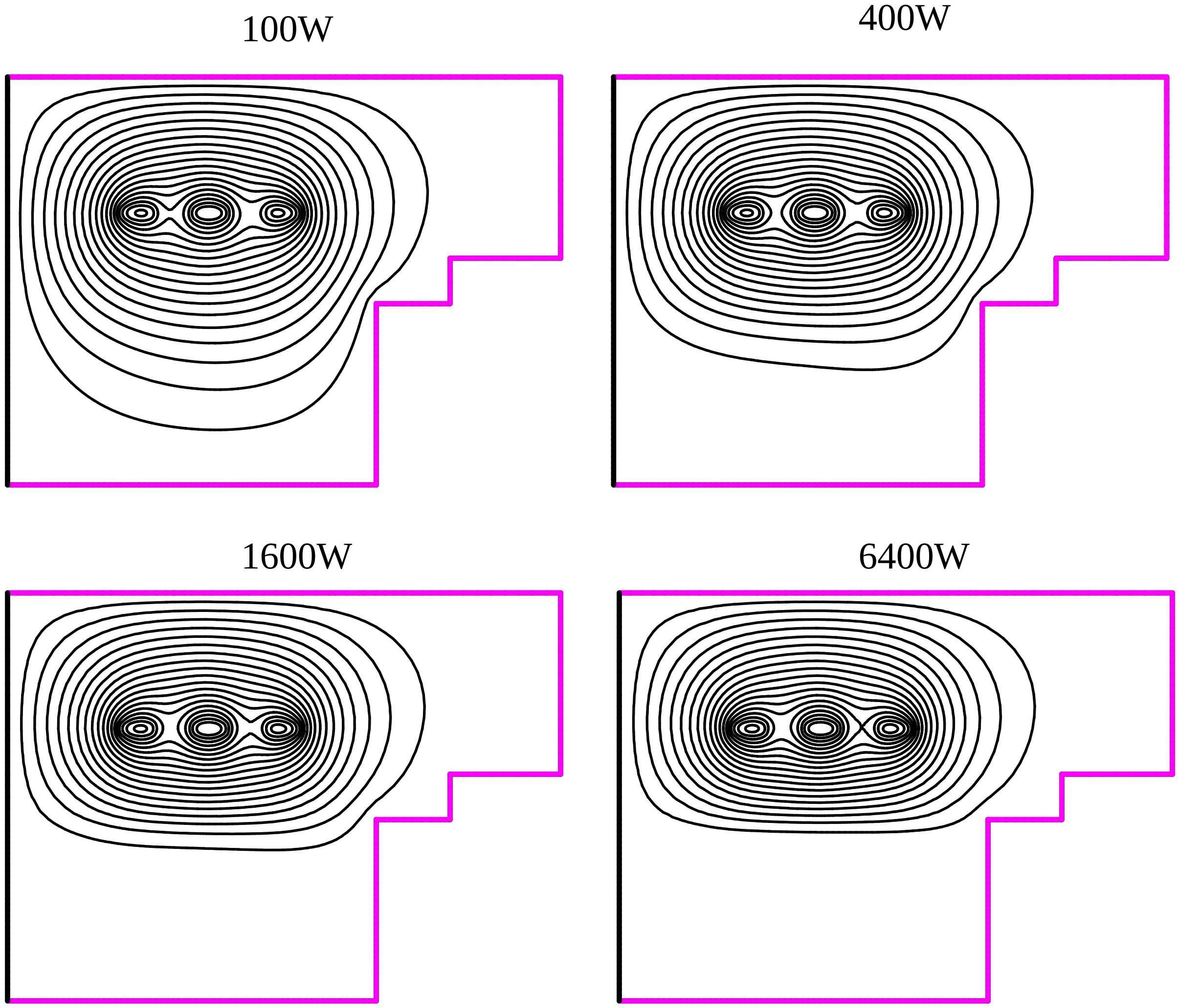

100W

400W

1600W

6400W

Figure 6.5: Induced electric fields at different values for the discharge power. Calculations were carried out for an argon discharge operating at a neutral gas pressure of $p_N = 5\,\mathrm{Pa}$ and a neutral gas temperature of $T_N = 300\,\mathrm{K}$.

The calculations show that with increasing input power the intensity distribution of the induced electric field changes drastically. While for an input power of 100 W the resulting electron density allows the induced electric field to fill the upper half of the reactor chamber, in the case of higher electron density the conductivity is the reason why eddy currents, flowing in the plasma, compensate the induced electric field almost completely. An area with significant field strength remains only in a very thin layer directly below the quartz window. The shielding caused by the conductivity of the plasma might be understood as a well known effect in the field of high frequency electronics, the so-called skin effect.

The skin effect effectively limits the electron density which can be produced by ICP discharges. Once the electron density exceeds a certain level, the discharge protects itself from further heating. The typical maximum electron density is in the order of $10^{13}\,\mathrm{cm}^{-3}$.

6.2 Influence of neutral gas pressure

In Sect. 5.1.5 the dependence on the neutral gas pressure has been investigated thoroughly. Especially the slowdown of the ambipolar transport process by an increasing number of ion-neutral collisions had been discussed.

When we use a two-dimensional model including an electron energy conservation equation, an additional aspect gains importance. The discussion of the induced electric field distribution revealed the fact that discharge heating only takes place in relatively small regions in the proximity to the antenna. The energy which is transferred to the electrons in this region is redistributed in the whole discharge chamber, and (elastic) electron neutral collisions (friction) are the reasons why a certain electron temperature gradient is required to enable the energy transfer. The electronic heat conductivity (c.f. Sect. 4.3.3), on the other hand, is indirectly proportional to the number of neutral particles, which means that, for higher pressure, the heating zones of the discharge are the regions with the highest mean electron energy, too. The critical pressure value, at which such inhomogeneities start to develop, is dependent on the dimensions of the considered discharge.

6.2.1 Pressure variation in a planar chamber

For the reactor chamber given in Fig. 6.1, the critical pressure is in the order of 10 Pa. The experimental and theoretical data, presented in Fig. 6.4, illustrate the existence of inhomogeneous density distributions.

In order to investigate the pressure dependence of the density distribution, measurements were carried out for neutral gas pressure values of 0.5, 2 and 5 Pa.

At a neutral gas pressure of $p_N = 0.5\,\mathrm{Pa}$, the simulation and the measurement show a profile with an electron density maximum in the centre of the discharge at $r = 0$ (c.f Fig 6.6 (a)). In the pressure range between $p_N = 2\,\mathrm{Pa}$ and $p_N = 5\,\mathrm{Pa}$, a transition occurs and the maximum in the proximity of the coil develops. The electron density distribution takes the shape of a torus. The torus shape becomes even more pronounced at higher pressure values, as Fig. 6.4 (b) indicates.

The formation of a torus shaped electron density distribution at higher neutral gas pressure is not surprising bearing in mind the radial variation of the induced electric field as shown in Fig. 6.3. The local maximum of the induced field correlates with local heating and local production of electron ion pairs by impact ionisation. One might conclude that this is valid for

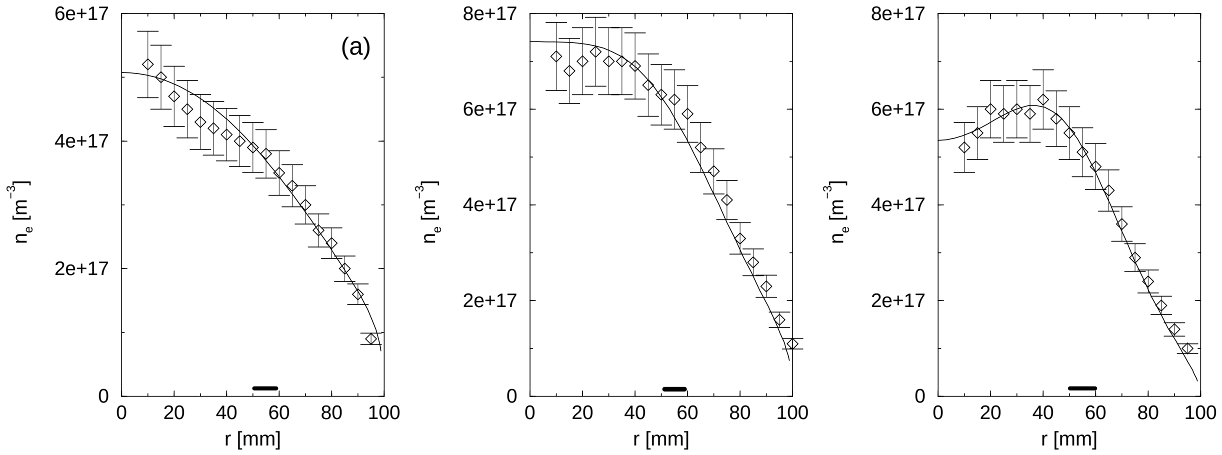

Figure 6.6: Experimental and theoretical radial electron density profiles for a planar ICP discharge operating in argon at different neutral gas pressure values: (a) $p_N = 0.5\,\mathrm{Pa}$, (b) $p_N = 2\,\mathrm{Pa}$ and (c) $p_N = 5\,\mathrm{Pa}$. Coil “2” was powered.

any chamber geometry but this generalisation should be avoided. Reasons will be given in the following section.

6.3 Influence of the reactor geometry

The previous sections focused on the question, how do different antenna configurations and a change in the working pressure determine the electron density distribution in the discharge chamber? Generally, in case of “low” pressure, the coil geometry does not have significant influence on the electron density distribution. The thermal conductivity of the electrons causes a redistribution of the energy, which is transferred to the discharge and produces a relatively homogeneous electron temperature profile[2]. The working pressure is in this regime in many process applications[3]. However, the question whether a certain pressure value can be considered to be low depends on the chamber dimension.

The high thermal conductivity at low pressure is the reason for the fact that in this regime characteristic plasma parameters like electron density and electron temperature can hardly be influenced by the geometry of the coils. The electron density distribution is determined by the reactor geometry rather than by the antenna design. Regarding the design of inductively coupled plasmas, two different cases can be distinguished:

- In a low pressure regime the coil configuration has a minor influence on the electron den-

---

[2] Here, the use of a discrete electron eigenvalue like in the case of one-dimensional hydrodynamic plasma models would be possible in this case.

[3] For example, etch processes try to minimise the number of ion-neutral collisions in the sheath region to obtain an ion impact perpendicular to the wafer surface. This is achieved by a working pressure in the sub-Pascal pressure range.

sity and temperature distribution in the reactor chamber. Homogeneity is predominantly influenced by the geometry of the chamber.

- In a high pressure regime a correlation between the coil position and the density as well as the temperature distribution exist. The discharge homogeneity is partly influenced by the coil position as well as by the discharge geometry.

6.3.1 Influence of aspect ratio

A good example which can be used to illustrate the effect of geometry and neutral gas pressure is the planar discharge which was discussed in the previous sections. The torus shaped region of high electron density, indicated by simulation and experiment at a neutral gas pressure of $p_N \geq 5.0\,\mathrm{Pa}$ is a typical phenomenon in planar chambers with an aspect ratio similar to the discussed example shown in Fig. 6.1. A number of other authors reported the same phenomenon [116], [53].

One might assume that the existence of the plasma torus is correlated with the distribution of the induced electric field as shown in Fig 6.3, but the geometry of the chamber, particularly the aspect ratio, play an important role. In the example discussed above, the chamber can be considered as “flat”. With a height of 4 cm and a diameter of 20 cm, most of the ions generated in the discharge will be absorbed by the top or bottom boundaries, i.e. ambipolar diffusion causes a particle transport, predominantly in z-direction. The situation turns out to be different in the case of “higher” chambers.

Theoretical data for a ratio of height to diameter of $H/2R = 100\,\mathrm{mm}/150\,\mathrm{mm}$ are shown in Fig. 6.7. The calculated electron temperatures in the case of an argon discharge, which operates at a neutral gas pressure of $p_N = 1.0\,\mathrm{Pa}$ (left plot) and $p_N = 5.0\,\mathrm{Pa}$ (right plot) can be seen. The discharge is driven by a set of three coils through which an equal current flows. In both cases the RF-power transferred to the discharge was chosen as $P_{RF} = 80\,\mathrm{W}$.

The resulting electron temperature distribution shows a maximum close to the quartz window because this is the region, where the largest part of the RF-power is deposited. The electron temperature shows a decrease towards all conducting boundaries of the discharge and towards the axis of symmetry of the cylindrical setup. This behaviour could be expected as in these regions almost no heating takes place. If $p_N = 1.0\,\mathrm{Pa}$, the temperature difference between the hottest spot close to the quartz window and the coldest region close to the lower boundary of the chamber is about $3500\,\mathrm{K}$. At $p_N = 5.0\,\mathrm{Pa}$, this temperature difference takes a value of $6500\,\mathrm{K}$. With respect to the temperature dependence of the ionisation rate of argon (c.f. Fig. 4.1), this temperature difference cannot be considered to be small. Ionisation will predominantly take place in the hot zone close to the quartz window. For the given chamber size this indicates that at a pressure of about $p_N = 5.0\,\mathrm{Pa}$ the discharge is localised closer to the quartz window.

This is confirmed by the corresponding contour plot of the electron density, as shown in Fig. 6.8. At a neutral gas pressure of $p_N = 1.0\,\mathrm{Pa}$, the discharge is almost symmetric in z-direction while for $p_N = 5.0\,\mathrm{Pa}$ the density distribution moves upwards in the direction of the quartz window, where the heating of the discharge takes place. Further simulations for higher neutral gas pressure values show that the maximum of the electron density remains on the axis $r = 0$.

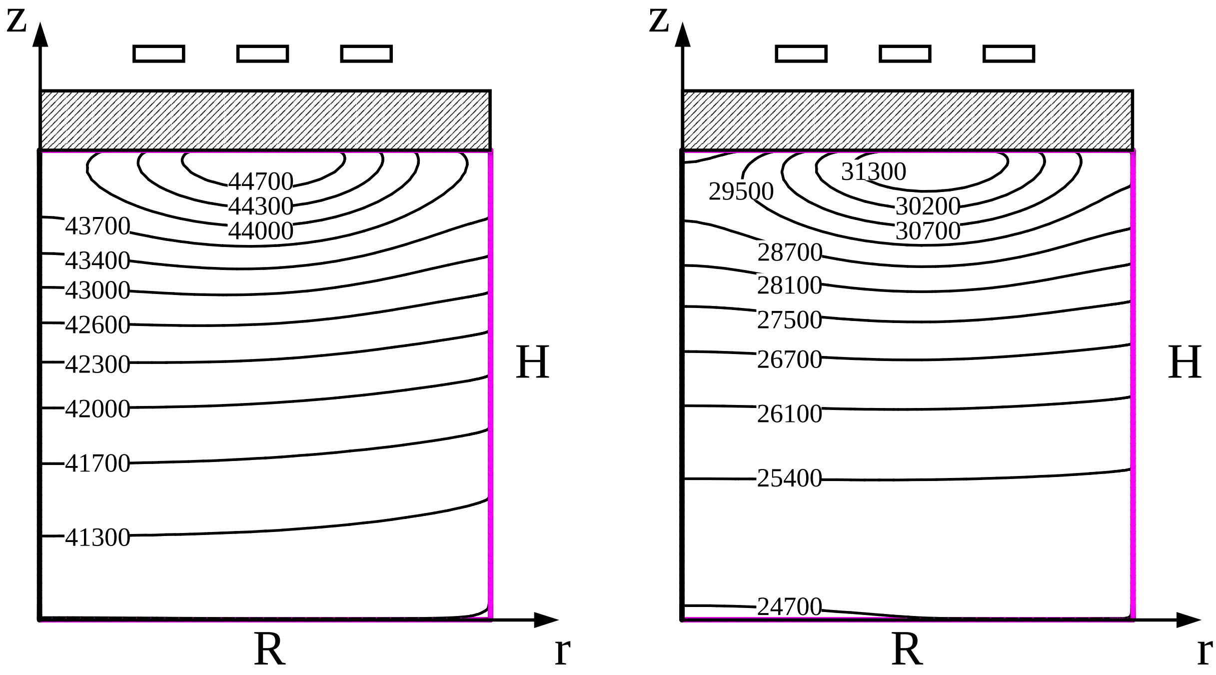

Figure 6.7: Contour plots of the electron temperature in K for a cylindrical ICP discharge operating in argon at $p_N = 1.0\,\mathrm{Pa}$ (left plot) and $p_N = 5.0\,\mathrm{Pa}$ (right plot). Calculations are based on a chamber height of $H = 100\,\mathrm{mm}$, a diameter of $2R = 150\,\mathrm{mm}$ and a neutral gas temperature of $T_N = 300\,\mathrm{K}$.

In no case, a torus like electron density distribution with an off-axis maximum develops. This is an example how geometric data, like the chamber aspect ratio, have a significant influence on the resulting density distribution in the discharge.

6.3.2 Experimental validation

The theoretical results in the previous section have predicted a localisation of the discharge close to the quartz window for high neutral gas pressure. They also indicate that a torus shaped electron density profile does not occur in the chosen chamber geometry. However, it would be desirable to check with what accuracy the model is in agreement with experimental data.

In Fig. 6.9, electron density measurements [4] and the corresponding simulations of the discharge, shown in Fig 6.7, are presented. Measurements were carried out in z-direction (z-profile, r = 0) and in r-direction (r-profile, $z = 50\,\mathrm{mm}$).

As only one Langmuir probe was available, the measurements in radial and axial direction were carried out sequentially. The discharge conditions seem to be not exactly the same, this

---

[4] This and all following experiments were carried out at the University of Augsburg, Germany. The ICP chamber was especially designed for plasma diagnostics in combination with chemical erosion experiments. Due to 5 flanges, radial as well as axial measurements were possible. Special thanks to H. Paulin and U. Fantz for cooperation.

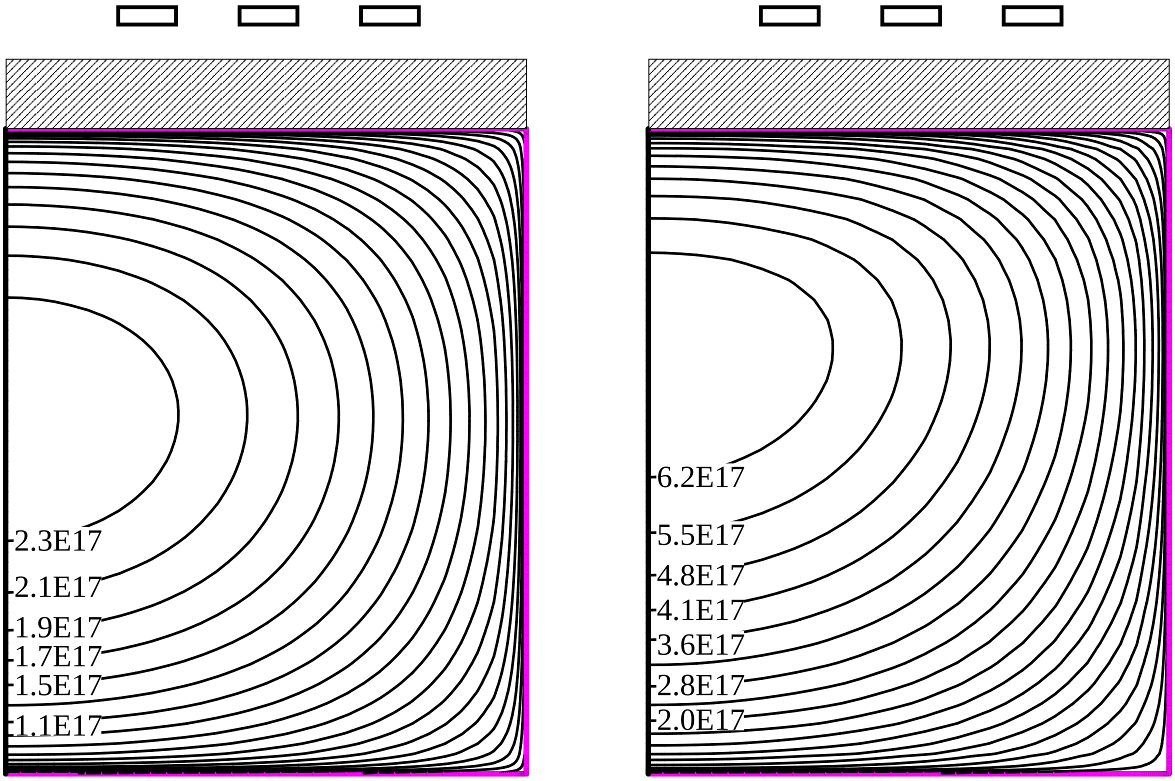

Figure 6.8: Contour plots of electron density $[\mathrm{m}^{-3}]$ for a cylindrical ICP discharge operating in argon at $p_N = 1.0\,\mathrm{Pa}$ (left plot) and $p_N = 5.0\,\mathrm{Pa}$ (right plot) for a neutral gas temperature $T_N = 300\,\mathrm{K}$.

is the reason why the peak values of the electron densities differ slightly. In order to be able to compare the measured values to the simulations, the RF-power needed as simulation input parameter was adjusted to match the measured electron peak densities. The resulting electron density profiles are in good agreement with the measurement.

Especially the asymmetry in z-direction predicted by the simulation is in excellent agreement with the measurement. The maximum of the electron density has clearly shifted towards the quartz window indicating a correlation with the hot zone (c.f Fig 6.7), where most of the impact ionisation takes place.

In radial direction, the simulation as well as the measurement show a monotonic decrease indicating that the maximum of the electron density is located at $r = 0$, i.e. on the axis of the rotational symmetric discharge.

The given results calculated for argon are comparable to data of other noble gases because the underlying effects like decreasing thermal conductivity at an increasing neutral gas pressure are similar.

Using helium as a discharge gas, one can expect a concentration of the discharge close to the quartz window at an increasing neutral gas pressure. On the other hand, the different

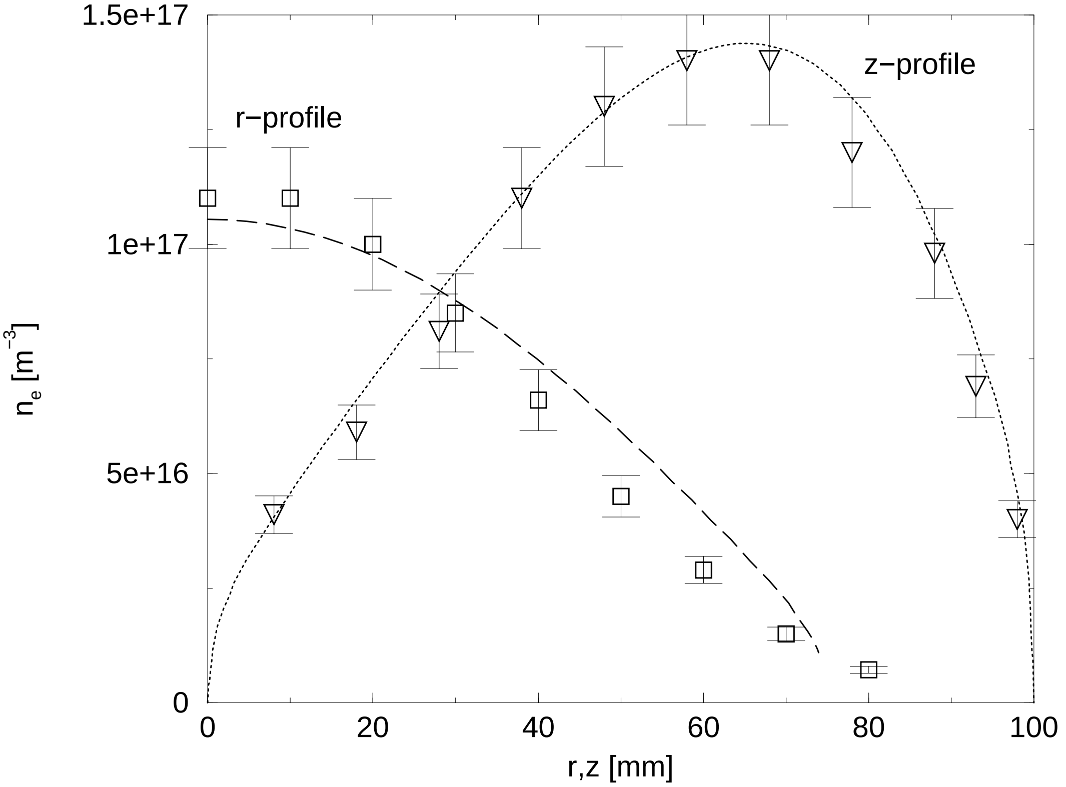

Figure 6.9: Measured and simulated electron density in an argon ICP discharge, operating at 5 Pa. The dashed line shows theoretical data for the profile in r-direction, the squares the corresponding measurement. The dotted line represents simulated data in z-direction, the triangles the corresponding measurement. Discharge power, used for the simulation, was adjusted to match the peak value of the measurement.

electron-neutral momentum transfer frequencies for argon and helium, as shown in Fig. 4.8, are the reason for the fact that the concentration of the discharge in the heating zone starts at higher pressure for helium than for argon. A collection of data illustrating this effect is given in Fig. 6.10. In order to achieve a comparability of the different profiles, simulated as well as calculated profiles were normalised to their maximum. Measured and calculated z-profiles show a fairly good agreement over the whole pressure range. Especially, the shift of the electron density maximum towards high z-values, i.e. in proximity to the quartz window, occurring with a rising neutral gas pressure, is in excellent agreement with the hydrodynamic model.

6.4 Input power and discharge efficiency

In the previous sections different examples for electron density distributions in ICP discharges have been presented. In order to achieve comparability of the model with the experiment, the

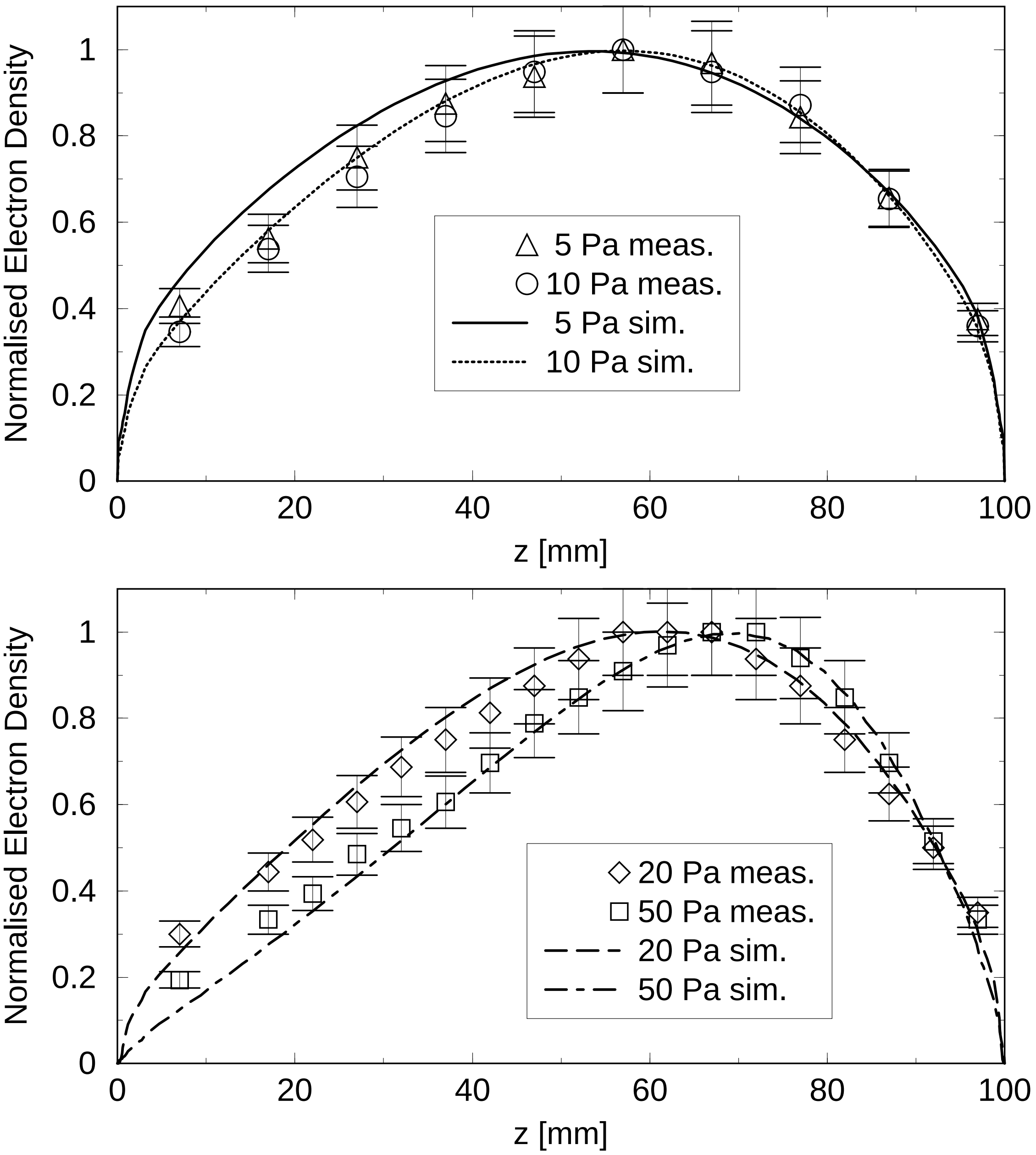

Figure 6.10: Measured and simulated electron density in a Helium discharge, operating in a pressure range from $5 - 50\,\mathrm{Pa}$. The data were normalised to the corresponding maximum.

model input parameter for the RF-power had been adjusted. At first glance this might look like using an additional degree of freedom to get a nice agreement of simulation and experiment. As will be shown in the following, the input parameter RF-power is more like a “knob to adjust” the results.

In order to assemble a complete set of boundary conditions, not only neutral gas pressure, temperature, generation rates, and collision frequencies have to be known, but also the coil current as input parameterfor the electrodynamic model are needed. The coil current, in combination with the electron density distribution in the plasma, is a measure for the power which causes a heating of the discharge. This power is a certain fraction of the power delivered by the RF-generator. To find a correlation between generator power and electron density is everything but trivial. Consider the following experimental experiences:

- ICP discharges typically show a warming-up-behaviour. Time-resolved measurements of the average electron density in the chamber typically vary significantly directly after ignition of the plasma. It takes several minutes up to hours until a steady state is reached. The variations in density can be several 10 percent of the final density value.
- Only a certain percentage of the RF-generator power can actually be transferred to the discharge. Power losses caused by the ohmic resistance of the coils or by eddy currents in the grounding walls or shieldings are the reason why the efficiency typically is in the order of several ten percent. The efficiency is strongly influenced by the electron density in the reactor and therefore is indirectly depending on adjustable external parameters like neutral gas pressure [40].
- Most process chambers are coated. Sputtering, redeposition, and surface chemistry are the reasons why very slow time constants (in the order of hours) can influence the discharge conditions. Long term measurements reveal a change in the plasma parameters which, for example, can be monitored by energy and mass spectrometry [4].

One has to confess that the power delivered to a discharge by the RF-generator is not a quantity which makes exact characterisation of the discharge possible. Depending on the process conditions, coil currents as well as the discharge efficiency could change in time while the RF-generator power remains constant.

In order to perform a simulation, some measure of the power transferred to the discharge must be known. The use of the RF-generator power instead of the coil current as an input parameter is a correct boundary condition from the model's point of view. But eventually only a small percentage[5] of the generator power will actually contribute to the heating of the discharge. The use of the experimental value for the generator power would therefore lead to average electron densities which are too high.

An alternative possibility, to achieve the comparability of experiment and the simulation, would be to measure the actual antenna coil current and to use it as an input parameter for the simulation. Unfortunately, the current values in the resonance circuit formed by the matching network and the antenna (in extreme cases more than 100 A and several 1000 V), make it a very demanding task to measure the coil currents in ICP systems. Despite the experimental difficulties, there exist publications where corresponding measurements are presented [40]. While such investigations provide valuable insights into the range of typical discharge efficiencies,

---

[5] Experimental investigations show that typical discharge efficiencies vary between 20 and 90 percent [63], [40].

the use of measured coil currents does not necessarily guarantee a well posed simulation setup. Calculations show that in a wide range of discharge power values the corresponding coil currents are almost equal (c.f. Fig. 6.11). The use of an experimental value with a certain range of accuracy could result in a disastrous deviation of the discharge power. The reason for this very high sensitivity is the following:

The current flowing through the antenna causes an induced electric field which heats the plasma in the reactor. The power transferred to the plasma is directly proportional to the induced currents in the plasma. These currents, on the other hand, are proportional to the conductivity and therefore proportional to the electron density (c.f. Fig. 2.2). So finally, the power consumed by the plasma is proportional to its average density[6]. For a given coil current, the power used for heating of the discharge is ambiguous and depends on the electron density distribution in the chamber.

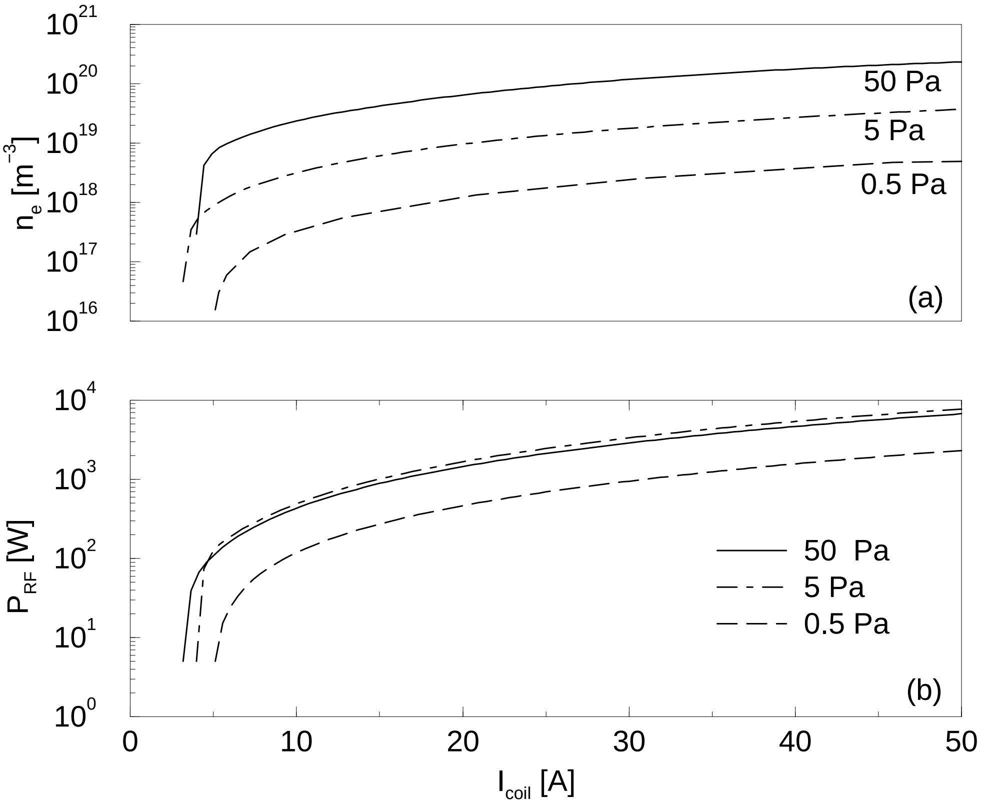

Figure 6.11: Peak electron density (a) and calculated heating power (b) versus coil current for a planar argon ICP discharge, operating at neutral gas pressure values of 0.5, 5 and 50 Pa

In Fig. 6.11, the dependence of discharge heating power on the coil current is displayed for the case of a planar cylindrical ICP discharge (c. f. Fig. 6.1). In dependence of the coil current

---

[6] A proportionality exists in good approximation in the case of electron densities which are so low that the skin effect can be neglected.

I_{coil}, the corresponding peak value of the electron density 6.11 (a) as well as the integral value of the power absorbed by the discharge 6.11 (b) have been calculated for an argon discharge operation in the neutral gas pressure range from $P_N = 0.5 - 50\,\mathrm{Pa}$. Please note the logarithmic scales, which have been used for the total power transferred to the plasma as well as for the peak electron density.

At all the considered pressure values in the range from $0.5 - 50\,\mathrm{Pa}$, the discharge power shows a very steep increase at low coil currents. In fact there exists a threshold current (for the given geometry with an antenna consisting of three coils about $3 - 5\,\mathrm{A}$) which is required to sustain the discharge. The minimum current is slightly depending on the neutral gas pressure, so for higher neutral gas pressures, it becomes lower. In the region close to this threshold current, the power shows a steep increase with the over one and a half orders of magnitude if $P_N = 5, 50\,\mathrm{Pa}$.

At higher power values the resulting higher average electron density in combination with the skin effect is the reason why significantly more coil current is needed a further increase the discharge power. In real applications this region is often never reached and discharges are typically operating in the region close above the threshold current.

The corresponding peak electron density in the discharge shows a very similar behaviour to the discharge power. For a low discharge power, i.e. in the current region just below the threshold current, the peak density rises as steep as the discharge power, while for higher coil currents a similar saturation like that of the discharge power is visible. The pressure dependence of the peak electron density is remarkable. As has been discussed in the previous sections, the discharge can be expected to become more concentrated in the region which is situated close to the antenna in case of a neutral gas pressure of $p_N = 50\,\mathrm{Pa}$. This concentration leads to the development of a distinct maximum, while in other regions of the discharge the electron density is significantly lower. At the low pressure of $p_N = 0.5\,\mathrm{Pa}$, the whole discharge chamber is filled with plasma, which leads to a peak electron density, which is significantly lower for the same coil current values.

Summarising the results of this section, the following points can be mentioned:

- Experimental evidence shows that only a part of the RF-generator power does contribute to the heating of the discharge. The efficiency depends on process parameters like neutral gas pressure and coil geometry.

- A minimum coil current exists which is necessary to sustain the discharge. In the region directly above this minimum coil current (i. e. at low discharge power values) the power coupled to the discharge is extremely dependent on the coil current.

- At low pressures the required coil current which corresponds with a certain value of the discharge power is higher than that at higher pressures. This correlates with efficiency measurements [40] which show lower efficiencies for lower neutral gas pressures.

- Neither the RF-generator power nor the coil current are parameters which can guarantee accurate accordance of simulation and experiment over a wide range of parameters.

The discussed effects are the reason why in this work, where experimental data have been compared with calculated results, the discharge power (i.e. this part of the RF-generator power which effectively heats the discharge) was adjusted to match the measured electron density in one point.

6.5 A design study

Especially the comparison of simulated results with experimental data presented in the previous sections indicates that hydrodynamic models are able to deliver reliable data about particle density distributions as well as transport processes in ICP discharges. While the models have been "tested" in a wide range of parameters so far, in this section the question will be treated how hydrodynamic models might be used in order to optimise design of process reactor chambers. The following issues are important especially for the designer of the chamber:

- **Homogeneity**: For many processes, it is essential to have homogeneous process conditions over the whole substrate area. It is a key feature of the chamber design, to ensure this property.
- **Scalability**: Especially, when considering the semiconductor fabrication with its continously increasing wafer diameters, one has to answer the question whether an upscaling of existing process equipment will be possible.
- **External parameters**: In many cases the requirements of the process will limit the range in which process parameters can be chosen.[7] However, it would be desirable to know how typical properties like the average electron density and the ion flux depend (qualitatively) on the external parameters, and over which range a proper discharge operation can be expected.

A simulation might provide some valuable insights or even answers to all the questions mentioned above. In this section will be demonstrated how simulation might contribute to the design of an optimised process chamber.

6.5.1 A model problem

Consider the following problem: An ICP discharge chamber has to be designed for the purpose of providing an ion flux to a substrate which should be as homogeneous as possible. The substrate has a diameter of about 20 cm, special requirements of the process[8] make it necessary that the operating pressure of the discharge is in the sub-Pascal region. The question is how to find a reactor and antenna geometry which provide the desired properties.

---

[7] Etching processes depend on a minimum number of ion collisions in the sheath region and are therefore typically operating in the sub-Pascal pressure range.

[8] Especially in dry etch processes it is important to minimise the number of ion-neutral collisions in the sheath region in order to get an ion flux as perpendicular as possible to the wafer surface.

6.5.2 General considerations

The experimental and theoretical data presented in the previous section deal with chambers which had the geometry of a cylinder. If the height of the cylinder is significantly smaller than its diameter (c.f. Fig. 6.1), the resulting electron density distribution has been shown to become torus-like if the neutral gas pressures is in the order of several ten Pascals. In the sub-Pascal pressure range a density profile in radial direction can be expected which has approximately the shape of a Bessel function. The density decreases monotonically from a maximum value on the axis of the cylinder towards zero at the outer boundary. This monotonic decrease of the electron density[9] is the reason why the ion flux which hits the top or bottom boundary also shows a monotonic decrease with increasing distance from the axis of the chamber. Only in a comparatively small region in the discharge centre the ion flux can be expected to be approximately constant.

This reflects the key difficulty in finding an optimised reactor geometry for the given model problem. Cylinder-shaped chambers typically show a decrease of electron and ion density with increasing distance from the axis. The physical reason is the presence of the outer wall which acts as a particle sink and causes electron and ion density to be very low in its proximity. A workaround which seems to be obvious at first glance is an increased diameter of the discharge. By moving the outer wall as far as possible from the substrate, its negative influence can be diminished. On the other hand a discharge chamber with three times the diameter of the substrate means that a big volume is filled with plasma and does not directly contribute to the process. Nevertheless, the RF-generator, matching network as well as antenna must be able to transfer a sufficient amount of plasma to the discharge. For this reason it would be desirable to keep the "dead" volume in the discharge as small as possible.

6.5.3 An optimised chamber geometry

A remedy is to give up the concept of a chamber which is of cylindrical shape. Please recall what the reason for the inhomogeneity of electron density is: Every wall of the discharge chamber acts as a particle sink. This is true for the plane bottom and top of the chamber as well as for the cylindrical outer boundary. It is possible to reduce the negative influence of this chamber wall by increasing the chamber diameter. A possiblity to do this without creating excessive discharge volume is shown in Fig 6.12.

The optimised chamber is cylindrically symmetric and consists of a a pot-shaped dielectric window, which is inserted in a (conducting) reactor housing of cylindrical shape. As a consequence the chamber consists of a flat, cylindrical region (region B) directly above the substrate. In the outer part, the region above the substrate is surrounded by a ring-shaped outer volume (region A). The distance to the substrate and the dielectric window is so small in this region that a strong particle flux towards both of those discharge boundaries can be expected. Generally, the homogeneity of the discharge parameters like electron density or ion flux towards the wall will depend on the geometry parameters denoted as a, b, c, and d.

---

[9] Assuming quasi-neutrality in the discharge bulk, the ion density has the same shape.

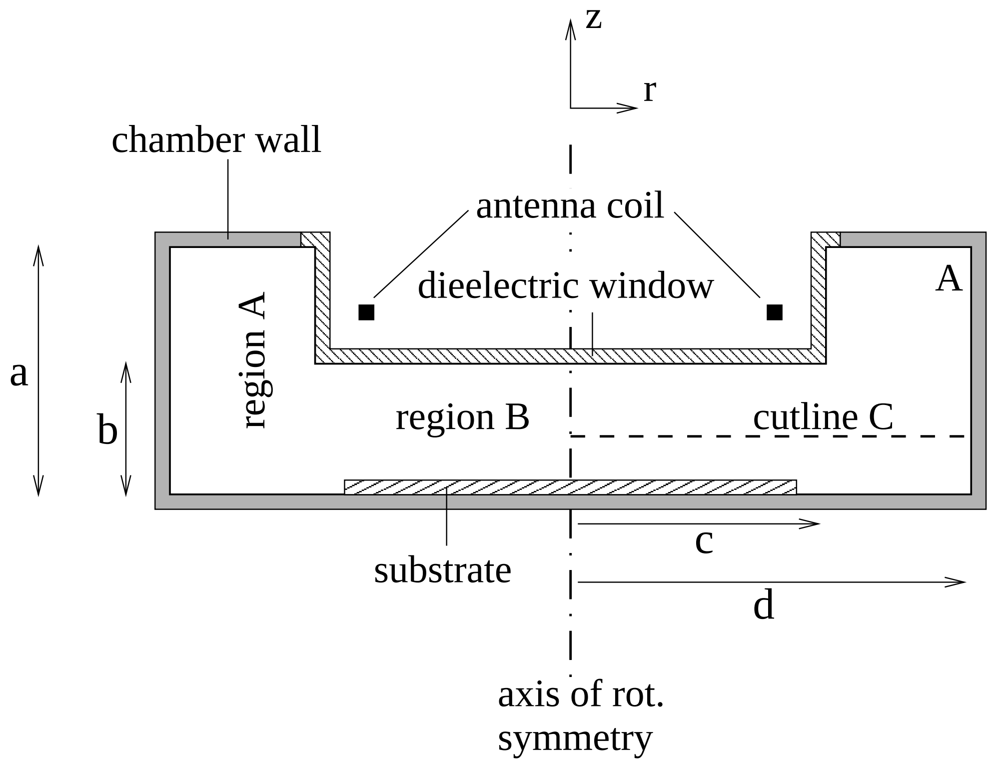

Figure 6.12: Optimised ICP chamber geometry to enhance the homogeneity in the region above a substrate to be processed.

How sensitively an electron density profile in the reactor chamber depends on the choice of the geometry parameters, and whether homogeneous plasma conditions over the substrate can be achieved, is shown in Fig. 6.13.

A variation of the geometry parameter b in Fig. 6.12 of approximately 25 percent causes significant changes in the discharge parameters. The given data were calculated along a cutline in radial direction in a distance of $20\,\mathrm{mm}$ from the bottom of the chamber (denoted as cutline "C" in Fig. 6.12).

Part a) of Fig. 6.13 shows the electron temperature variation in radial direction. Generally, the variation of electron temperature is small compared with its absolute value. A slight rise in the temperature in the proximity of the antenna can be observed, but the absolute change is less than two percent of the maximum value. The dependence on the geometry parameter b is interesting. For the highest value of b the average electron temperature takes its lowest value. This result is just another aspect of the results presented in Sect. 5.1.2. The eigenvalue of the electron temperature is depending on the discharge volume as well as the discharge geometry. A larger discharge volume (or a larger chamber height) correlates with a lower value of the electron temperature. This is also in accordance with the electron density values shown in Fig. 6.13 b). All the calculations were performed under the assumption that a discharge power of $100\,\mathrm{W}$ was transferred to the plasma. A larger discharge volume (caused by a larger value of b),

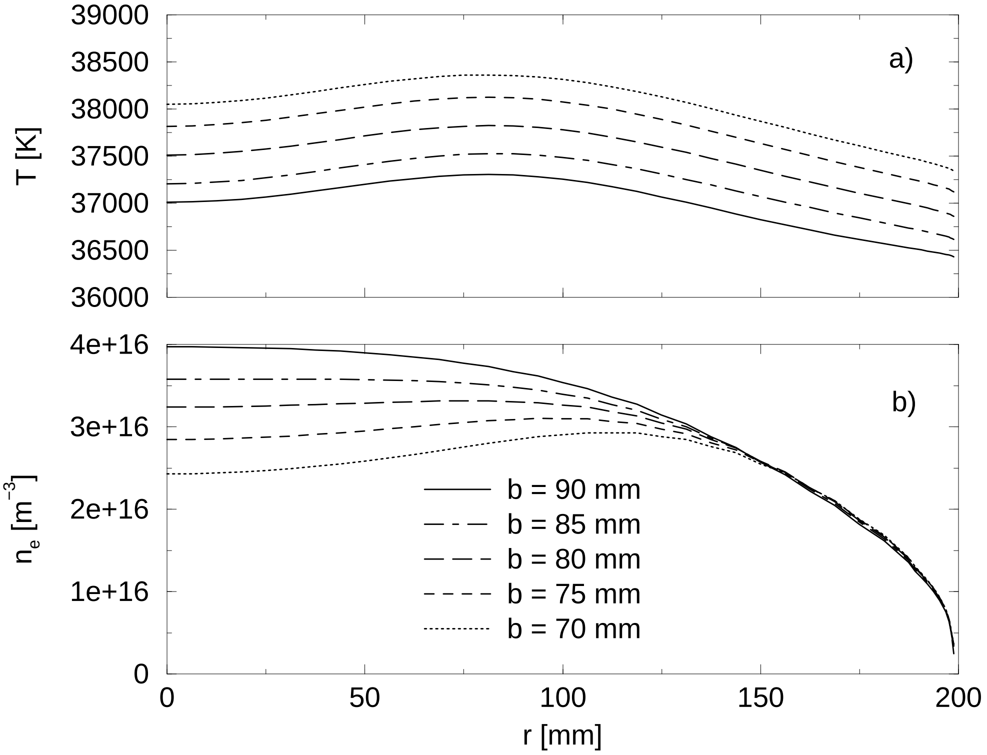

Figure 6.13: Electron temperature T_e a) and electron density n_e b) calculated for an argon discharge, operating at $p_N = 0.5\,\mathrm{Pa}$. Results are shown for a radial cut (cutline "C" in Fig. 6.12). Geometry parameters: $a = 150\,\mathrm{mm}$, $c = 100\,\mathrm{mm}$, $d = 200\,\mathrm{mm}$, b was varied in the range from $70 - 90\,\mathrm{mm}$.

therefore, corresponds to a higher value of the electron density n_e because in this case diffusion processes are slower. This is in accordance with the electron temperature profiles as shown in 6.13.

The main result of the presented study is the change of the electron density profiles. At the largest considered value of $b = 90\,\mathrm{mm}$, the chamber geometry can be considered as "almost cylindrical". The resulting electron density profile is monotonically decreasing. At the smallest considered chamber height of $b = 70\,\mathrm{mm}$, the electron density profile shows a clearly visible off axis maximum at the position of $r = 120\,\mathrm{mm}$ This maximum exists because the ambipolar diffusion process in the "small" gap between the chamber bottom and the quartz window causes a very effective transport of particles to the walls, leading to a reduction of the electron density in the discharge center.

The desired homogeneity lies in between the two discussed extremes. If $b = 85$ mm, the electron density profile is in fact almost perfectly flat over a radial distance of 90 mm. If $b = 85$ mm the variation is also acceptably small. The high sensitivity of the profile flatness in dependence of b is remarkable. If $b = 90\,\mathrm{mm}$, the electron density drops about ten percent in a distance of $100 \mathrm{~mm}$ from the axis of symmetry. This drop can be totally compensated by a five percent change of b.

This result underlines the importance of numerical modelling in order to get an optimised chamber geometry. On the other hand, it would be desirable to have some rules of thumb to understand the underlying scaling laws. It would also be interesting to answer the question why a certain set of geometry parameters caused a result which was sufficiently homogeneous. This is the topic of the following section.

6.6 Rules of thumb for ICP design

The numerical results shown in the last section underlined that desired quantities like homogeneity might be optimised by using a sophisticated chamber geometry. On the other hand it would be desirable to have a set of "rules of thumb" which allow an approximate prediction of results without having to perform intensive numerical modelling. It is the purpose of this section to suggest a few of these essential correlations which might be useful to the designer of a reactor chamber.

6.6.1 Low pressure versus high pressure

The question, how low a pressure would have to be that one can speak of "low pressure" is somewhat rhetoric. The discharge dimensions as well as the used process gases make it difficult to give an answer which is generally valid. Consider the quantities which depend directly on the operating pressure of a discharge:

- the ion-electron production by impact ionisation (c.f. Sect. 4.1),
- the ion neutral collision rate (c.f. Sect. 4.2),
- the electronic thermal conductivity (c.f. Sect. 4.3.3).

What does "low pressure" actually mean? Let us consider some typical discharge applications to find an answer. We have to distinguish several effects, all related to the number of neutral particles per volume:

A typical technical problem is the occurance of ion-neutral collisions in sheath regions which should be avoided in plasma etching applications. The probability of a collision is proportional to the number of neutral atoms per volume, i.e. to the neutral gas pressure and to the extension of the sheath region which depends indirectly proportional on the square root of the electron density in the source (c.f. Sect. 5.1.4). In order to avoid those collisions, two obvious solutions exist: The use of a low neutral gas pressure and/or a high density plasma source. For this reason in fact typical etching applications operate in the sub-Pascal region.

The second influence of the pressure concerns the overall ion-electron production in the discharge. A higher neutral gas pressure is correlated with a lower electron temperature (c.f. Sect. 5.1.5) as the number of atoms which can be ionised is proportional to the pressure. On the other hand, the friction of ions in the discharge bulk generally reduces the ability of the discharge to transport charged particles to the wall, which leads to reduced particle fluxes. The absolute value of the flux is geometry dependent. The particle flux is approximately directed towards the nearest surface. The average distance to the nearest surface is rather a measure to characterise a discharge than its volume. The question what is ment by “low pressure”, is rather a question of the ration of mean ion free path to a average distance from the nearest wall.

The last aspect concerns again the electrons in the discharge. Their thermal conductivity is indirectly proportional to the neutral gas pressure. The question, which pressure values will lead to an inhomogeneous temperature distribution, is rather a question of the electron mean free path compared to the extensions of the discharge. As the example in Sect. 6.5.3 shows, a pressure of $0.5\,\mathrm{Pa}$ for a discharge diameter of $0.5\,\mathrm{m}$ might still be considered to be low. Is this not the case (see. Sect. 6.2.1), an inhomogeneous electron temperature distribution can develop, which causes an inhomogeneous electron density distribution.

6.6.2 Antenna geometry

On one hand, the question of discharge homogeneity is related to the operating pressure. If the pressure should be high enough to cause significant inhomogeneities in the electron temperature, the chosen coil geometry will have influence on the density distribution. On the other hand, when “low” pressure leads to a homogeneous temperature distribution, the antenna design has minor influence on the density distribution. For reasons of efficiency, the distance of antenna and plasma should be as small as possible. As calculations of the induced electric field (c.f. Sect. 6.1.1) as well as measurements [41],[40] indicate, the induced electric field decreases exponentially with the distance from the antenna. In order to ensure a discharge operation for large distances between coil and plasma, high RF-currents are required, leading to ohmic and other losses and reducing the net discharge efficiency. In any case the antenna design is a problem of trade-off. A possibility to reduce the necessary current, is to enlarge the number of coils or coil turns. But the coil inductance in combination with a capacitor included in the matching network must form a tank circuit with a resonance frequency which is approximately equal to the driving RF. A large antenna inductance means small values for the capacitor and high voltages on one end of the coil, both of which are undesirable effects. A small coil inductance, on the other hand, means that large currents are required. The cross section of the coil and it’s total area have influence on the capacitive coupling. A large coil area means also an effective capacitive coupling.

6.6.3 Discharge geometry

Maybe the most difficult task in designing a reactor is the choice of an adequate discharge geometry.

The example discussed in Sect. 6.5.3 demonstrated the change of discharge parameters caused by a variation of a geometry parameter. In this section an explanation of this sensitivity will be given. In a deliberate simplification the chamber geometry as shown in Fig. 6.12, can be assumed to consist of two separate parts, denoted as “region A” and “region B”. In the case of

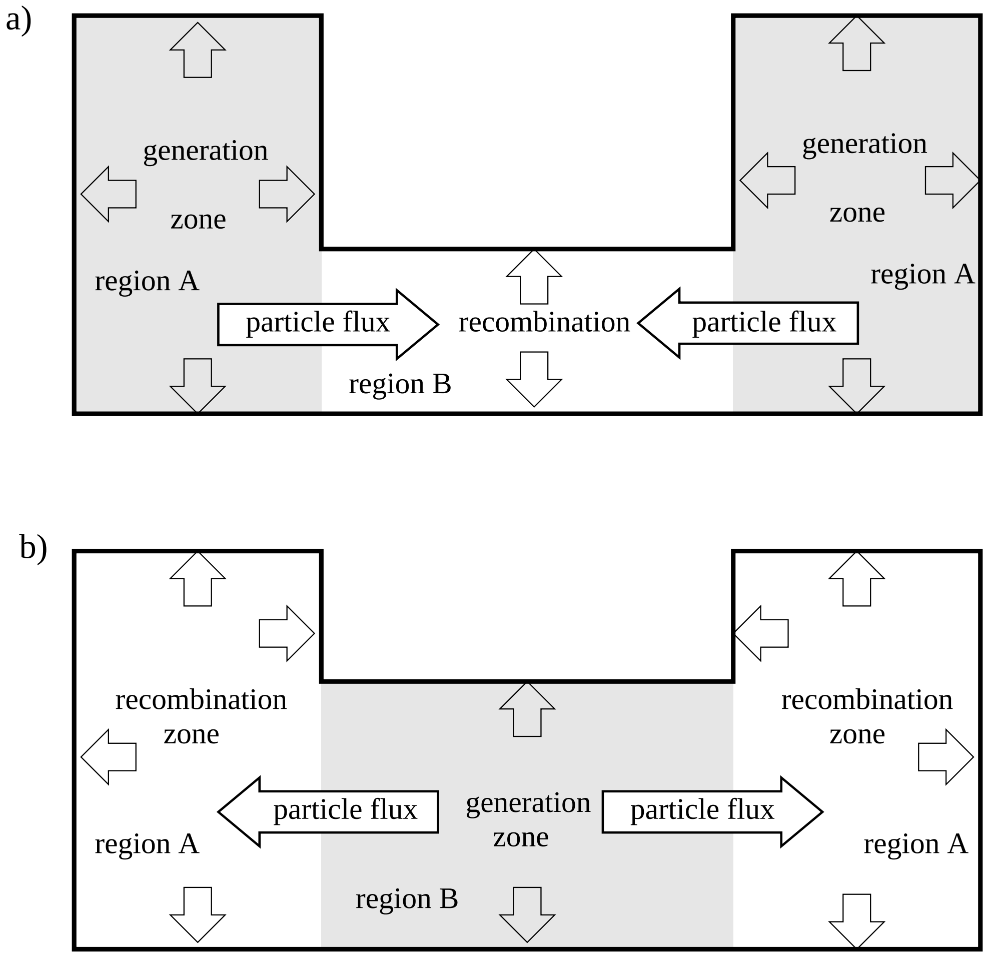

Figure 6.14: Particle exchange in different parts of the discharge in dependence of geometry parameters.

"low pressure" the electron temperature will be approximately equal in both regions, however, in dependence on the volume of the two regions, a particle flux from one region to the other may occur. Consider the case illustrated in Fig. 6.14 a): The central region of the discharge is flat, i.e. the average distance to the nearest wall is significantly smaller than that in region "A". As a consequence, the whole region "B" acts as a particle sink, i.e. more charged particles are transported to the walls than are produced by impact ionisation. The difference is balanced by a particle flux from region "A". In this region more particles are produced than can be transported to the walls so that the surplus amount is transferred to region "B". The calculated electron density profiles shown in Fig. 6.13 in the case of $b = 70\,\mathrm{mm}$ confirm the given explanation. Electron density takes its maximum at $r = 110\,\mathrm{mm}$, i. e. in region "A". A density gradient directed towards the axis of rotational symmetry drives a particle flux, causing a transfer of particles produced in region "B".

The opposite happens, when the height of region "B" is increased so much that the average distance to the nearest wall gets larger than in region “A”. As a consequence the regions “A” and “B” exchange their roles, region “B” now acts as a generation zone and surplus ions and electrons are transferred to region “A”. This case is illustrated in Fig. 6.14 b). The corresponding electron density profile is shown in Fig. 6.13 for $b = 90\,\mathrm{mm}$. The electron density gradient at any point is directed outward and, therefore, drives a particle flux from the discharge centre to the outer parts.

Having understood the consequences of chosing a high or low value for the parameter b, which controls the height of the central discharge region “B”, it is not surprising that intermediate values of b cause a almost perfectly homogeneous electron density profile in the centre of the discharge. If the particle production in region “A” as well as in region “B” equals the wall recombination, no (intergral) exchange of particles between the two regions will occur. This means that also no electron density gradient is required to drive such an exchange process which results in a density profile that is flat in radial direction. This is exactly what is needed for a maximum of homogeneity.

The result can be generalised: A discharge may be decomposed in separate regions acting as generation zones or particle sinks. A particle sink or recombination zone denote a part of the discharge in which more particles are driven to the walls (where recombination takes place) than are actally produced in the considered volume. Under stationary conditions, the electron temperature will have adjusted to a value which ensures that the overall particle generation balances the wall recombination (for the whole discharge). If certain regions of the discharge show a small average distance to the nearest wall (or the ratio of surface to volume is large compared with other parts of the discharge) these regions will serve as particle sinks (or recombination zones). A density gradient will exist, where a recombination zone is connected with a generation zone. If such a density gradient must be avoided (as in the example discussed above), the size of generation or recombination zones has to be altered.

So far, the given design criteria have been explained for a low pressure example. Low pressure has the advantage that the coil configuration has only minor influence on discharge homogeneity and that the electron temperature can be considered to be constant in the whole discharge. In case of higher pressures, the application of design rules becomes more difficult.

If the neutral gas pressure is so high that significant electron temperature differences exist in the discharge, one might be no longer able to decide whether a certain part of the discharge does act as generation or as a recombination zone. Generation takes place where the induced electric field produces the most energetic electrons. This automatically defines the source region. Another aspect which complicates the chamber design for high pressures are significant changes in the density distribution, which might be caused by small variations of the neutral gas pressure or the temperature. In high pressure discharges density distributions do generally depend on the chamber geometry as well as on the coil configuration.

Chapter 7

Conclusion

Goal of the presented thesis is to review briefly the theoretical background from which hydrodynamic models for low pressure low temperature plasmas can be derived. The resulting conservation equations are discussed, especially with respect to their numerical solution. The question of approximations which speed up numerical algorithms or make them more stable is treated in detail.

In a second part, the applicability of hydrodynamic models to low pressure, low temperature plasmas is shown. Different kinds of discharges are investigated theoretically. For the case of inductively coupled noble gas discharges theoretical data is compared with experimental values.

Excellent agreement with experimental data obtained from Langmuir probe measurements in inductively coupled discharges showed that a hydrodynamic model system can serve as an ideal tool for reactor design. The good agreement of density measurements with theoretical data in a wide pressure range at different positions is an indicator that a hydrodynamic model system can provide reliable predictive results.

The model system is able to resolve transport processes in the bulk of the discharge as well as in the sheath region. Ion inertia is considered throughout the whole plasma, which means that two-dimensional sheat regions are described by the model. By using such a hydrodynamic model it is possible to calculate quantities like ion fluxes or energies for all surfaces exposed to the plasma. Those quantities can be determined only with high experimental effort. A further example is the overall discharge efficiency which can be determined by using a combination of a hydrodynamic model calibrated with data from Langmuir probe measurements.

In a final section, it was demonstrated how hydrodynamic plasma simulations can be used to design optimised reactor geometries. It could be shown, how geometry parameters like the chamber height and diameter have crucial influence on electron density in the discharge chamber. The electron density is a good measure for the ion flux to the surface, which is a quantity of technological interest. Further it could be shown, how the chamber can be optimised with respect to the homogeneity by chosing a certain chamber geometry. Additional chamber volume can, if carefully chosen, contribute to almost perfect density profiles in the chamber center.

Appendix A

Tables

	2.0 eV	2.4 eV	2.8 eV	3.2 eV	3.6 eV	4.0 eV	4.4 eV	4.8 eV	5.2 eV
0.10 Pa	0.019	0.023	0.026	0.028	0.030	0.032	0.032	0.033	0.033
0.15 Pa	0.028	0.033	0.038	0.042	0.044	0.046	0.048	0.049	0.049
0.22 Pa	0.040	0.049	0.056	0.061	0.065	0.068	0.070	0.071	0.072
0.32 Pa	0.059	0.072	0.082	0.090	0.096	0.100	0.102	0.104	0.106
0.46 Pa	0.086	0.105	0.120	0.131	0.140	0.146	0.150	0.153	0.155
0.68 Pa	0.126	0.153	0.175	0.192	0.205	0.214	0.220	0.224	0.227
1.0 Pa	0.182	0.222	0.254	0.279	0.298	0.311	0.321	0.327	0.331
1.5 Pa	0.258	0.317	0.365	0.402	0.430	0.451	0.465	0.475	0.482
2.2 Pa	0.360	0.443	0.514	0.571	0.614	0.646	0.669	0.686	0.696
3.2 Pa	0.490	0.607	0.710	0.795	0.863	0.914	0.952	0.980	0.998
4.6 Pa	0.655	0.815	0.962	1.09	1.19	1.28	1.34	1.39	1.42
6.8 Pa	0.864	1.08	1.29	1.47	1.63	1.76	1.86	1.94	2.00
10 Pa	1.14	1.43	1.71	1.97	2.20	2.40	2.57	2.70	2.80
15 Pa	1.49	1.88	2.27	2.64	2.98	3.27	3.53	3.74	3.91
22 Pa	1.97	2.50	3.02	3.54	4.02	4.46	4.84	5.17	5.44
32 Pa	2.62	3.33	4.06	4.78	5.47	6.10	6.67	7.16	7.57
46 Pa	3.53	4.50	5.50	6.52	7.48	8.40	9.23	9.96	10.6
68 Pa	4.79	6.14	7.53	8.96	10.3	11.7	12.9	14.0	14.9
100 Pa	6.56	8.45	10.4	12.4	14.4	16.3	18.1	19.7	21.1

Table A.1: Normalised effective momentum transfer frequency ν_{eff}/ω_{RF} for argon for a pressure range from 0.1 Pa to 100 Pa and an electron temperature from $2 - 5.2$ eV. A neutral gas temperature of $T_N = 300\,\mathrm{K}$, $\omega_{RF} = 2\pi \cdot 27\,\mathrm{Mhz}$ was assumed.

	2.0 eV	2.4 eV	2.8 eV	3.2 eV	3.6 eV	4.0 eV	4.4 eV	4.8 eV	5.2 eV
0.10 Pa	1.00	1.00	1.00	1.00	1.00	1.00	1.00	1.00	1.00
0.15 Pa	1.00	1.00	1.00	1.00	1.00	1.00	1.00	1.00	1.00
0.22 Pa	1.00	1.00	1.00	1.00	1.00	1.00	1.00	1.00	1.00
0.32 Pa	1.00	1.00	1.00	1.00	1.00	1.00	1.00	1.00	1.00
0.46 Pa	1.00	1.01	1.01	1.01	1.00	1.00	1.00	1.00	1.00
0.68 Pa	1.01	1.01	1.01	1.01	1.01	1.01	1.01	1.01	1.01
1.0 Pa	1.02	1.02	1.02	1.02	1.02	1.02	1.02	1.02	1.01
1.5 Pa	1.04	1.05	1.05	1.05	1.04	1.04	1.04	1.03	1.03
2.2 Pa	1.08	1.09	1.09	1.09	1.08	1.08	1.07	1.06	1.06
3.2 Pa	1.13	1.16	1.16	1.16	1.15	1.14	1.13	1.12	1.10
4.6 Pa	1.21	1.25	1.27	1.27	1.26	1.24	1.22	1.20	1.18
6.8 Pa	1.31	1.37	1.41	1.42	1.41	1.39	1.36	1.33	1.30
10 Pa	1.44	1.52	1.58	1.61	1.61	1.59	1.55	1.51	1.47
15 Pa	1.59	1.71	1.80	1.85	1.86	1.84	1.80	1.75	1.70
22 Pa	1.78	1.94	2.06	2.14	2.17	2.16	2.12	2.07	2.00
32 Pa	2.00	2.21	2.37	2.48	2.54	2.55	2.51	2.46	2.37
46 Pa	2.27	2.53	2.74	2.89	2.99	3.01	2.98	2.93	2.83
68 Pa	2.60	2.92	3.19	3.38	3.51	3.56	3.55	3.49	3.38
100 Pa	3.01	3.40	3.73	3.98	4.15	4.23	4.23	4.17	4.04

Table A.2: Normalised effective RF frequency ω_{eff}/ω_{RF} for argon for a pressure range from 0.1 Pa to 100 Pa and an electron temperature from $2 - 5.2$ eV. A neutral gas temperature of $T_N = 300\,\mathrm{K}$, $\omega_{RF} = 2\pi \cdot 27\,\mathrm{Mhz}$ was assumed.

	2.0 eV	2.4 eV	2.8 eV	3.2 eV	3.6 eV	4.0 eV	4.4 eV	4.8 eV	5.2 eV
0.10 Pa	0.019	0.023	0.026	0.028	0.030	0.032	0.032	0.033	0.033
0.15 Pa	0.027	0.033	0.038	0.042	0.044	0.046	0.047	0.048	0.049
0.22 Pa	0.040	0.049	0.056	0.061	0.065	0.068	0.069	0.071	0.072
0.32 Pa	0.059	0.071	0.081	0.089	0.094	0.098	0.101	0.103	0.104
0.46 Pa	0.085	0.103	0.117	0.128	0.136	0.142	0.146	0.149	0.150
0.68 Pa	0.121	0.146	0.166	0.181	0.193	0.201	0.206	0.210	0.213
1.0 Pa	0.169	0.202	0.228	0.248	0.263	0.274	0.282	0.287	0.291
1.5 Pa	0.224	0.264	0.296	0.319	0.338	0.351	0.361	0.368	0.373
2.2 Pa	0.279	0.320	0.352	0.377	0.395	0.409	0.420	0.428	0.435
3.2 Pa	0.321	0.357	0.382	0.401	0.416	0.427	0.437	0.444	0.450
4.6 Pa	0.346	0.367	0.380	0.389	0.396	0.402	0.408	0.412	0.416
6.8 Pa	0.350	0.355	0.354	0.353	0.351	0.350	0.350	0.351	0.352
10 Pa	0.338	0.327	0.315	0.305	0.296	0.290	0.285	0.282	0.280
15 Pa	0.313	0.291	0.271	0.255	0.242	0.232	0.225	0.219	0.215
22 Pa	0.279	0.250	0.226	0.207	0.193	0.182	0.173	0.167	0.162
32 Pa	0.241	0.208	0.184	0.165	0.150	0.140	0.131	0.125	0.120
46 Pa	0.200	0.169	0.146	0.128	0.115	0.105	0.098	0.092	0.088
68 Pa	0.161	0.133	0.113	0.098	0.087	0.078	0.072	0.067	0.064
100 Pa	0.126	0.102	0.085	0.073	0.064	0.057	0.052	0.049	0.046

Table A.3: Normalised real part of the complex conductivity defined in (4.10) for argon in a pressure range from 0.1 Pa to 100 Pa and an electron temperature from 2 eV to 5.2 eV. A neutral gas temperature of $T_N = 300\,\mathrm{K}$, $\omega_{RF} = 2\pi \cdot 27\,\mathrm{Mhz}$ was assumed.

Bibliography

[1] J. E. Allen, R. L. F. Boyd, and P. Reynolds. The collection of positive ions by a probe immersed in a plasma. *Proc. Phys. Soc. London*, 70:297–304, 1956.

[2] Semiconductor Industry Association. *International Technology Roadmap for Semiconductors: 1999 edition*. TX:International SEMATECH, 1999.

[3] S. A. Astashkevic, M. Käning, E. Käning, N. V. Kokina, B. P. Lavrov, A. Ohl, and J. Röpke. *J. Quant. Spectro. Radiat. Transfer*, 56:725–751, 1996.

[4] P. Awakowicz, R. Schwefel, M. Werder, and W. Kasper. Diamond deposition and plasma diagnostics in a 27 MHz inductive coupled reactor (ICP). *Diamond Relat. Mater.*, 6:1816–1823, 1997.

[5] R. E. Bank, Jr. W. M. Coughran, W. Fichtner, E. H. Grosse, D. J. Rose, and K. Smith. Transient simulation of silicon devices and circuits. *IEEE Trans. CAD*, 4(4):436–450, 1985.

[6] M. S. Barnes, T. J. Colter, and M. E. Elta. Large-signal time-domain modeling of low pressure rf glow discharges. *J. Appl. Phys.*, 61(1):81–89, 1987.

[7] M. S. Barnes, T. J. Colter, and M. E. Elta. A staggered-mesh finite-difference numerical method for soling the transport equations in low pressure RF glow discharges. *J. Comp. Phys.*, 77:53–72, 1988.

[8] M. S. Barnes, J. C. Foster, and J. H. Keller. Electron energy distribution function measurements in a planar inductive oxygen radio frequency glow discharge. *Appl. Phys. Lett.*, 62(21):2622–2624, 1993.

[9] K. Behringer. Diagnostics and modelling of ECRH microwave discharges. *Plasma Phys. and Contr. Fusion*, 33(9):997–1028, 1991.

[10] K. L. Bell, H. B. Gilbody, J. G. Hughes, A. E. Kingston, and F. J. Smith. Recommended data on the electron impact ionization of light atoms and ions. *J.Phys. Chem. Ref. Data*, 12(4):891–916, 1983.

[11] I. B. Bernstein and I.N. Rabinowitz. Theory of electrostatic probes in a low density plasma. *Physics Fluids.*, 2:112–121, 1959.

[12] C. K. Birdsall. Particle-in-cell charged-particle simulations plus monte carlo collisions with neutral atoms, PIC-MCC. *IEEE Trans. Plasma Sci.*, 19(2):65–85, 1991.

[13] C. K. Birdsall and A. B. Langdon. *Plasma Physics via Computer Simulation*. Institute of Physics Publishing, 1991.

[14] J.-P. Boeuf. Numerical model of rf glow discharges. *Phys. Rev. A*, 36(6):2782–2792, 1987.

[15] D. Bose, T. R. Govindan, and M. Meyyappan. A continuum model for the inductively coupled plasma reactor in semiconductor processing. *J. Electrochem. Soc.*, 146(7):2705–2711, 1999.

[16] F. Bose, R. Patrick, and H. P. Baltes. Characterisation of plasma etch processes using measurements of discharge impedance. *J. Vac. Sci Technol. B*, 12(4):2805–2809, 1994.

[17] H.-J. Bungartz, F. Durst, and C. Zenger. *High Perfomance Scientific and Engineering Computing*. Springer, 1998.

[18] C. Cercignani. *Theory and application of the Boltzmann Equation*. Scottish Academic Press, 1975.

[19] S. Chapman and T. Cowling. *The mathematical theory of non-uniform gases*. Univ. Press, 1934.

[20] W. Z. Collison, T. Q. Ni, and M. S. Barnes. Studies of low-pressure inductively-coupled plasma etching for a larger area wafer using plasma modeling and Langmuir probe. *J. Vac. Sci. Technol. A*, 16(1):100–107, 1998.

[21] R. W. Crompton, M. T. Elford, and A. G. Robertson. The momentum transfer cross section for electrons in helium derived from drift velocities at 77k. *Aust. J. Phys*, 23:667–681, 1970.

[22] A. Danjo. Electron scattering from Kr: I. differential cross section for elastic scattering. *J. Phys. B*, 21:3759–3766, 1988.

[23] H. Date, Y. Sakai, and H. Tagashira. Boltzmann equation analysis of e^- collision cross sections and swarm parameters for krypton. *J. Phys. D.*, 22:1478–1481, 1989.

[24] F. de Jong and M. Meyyappan. Numerical simulation of silicon carbide chemical vapor deposition. *Diam. Rel. Mat.*, 6:141–150, 1996.

[25] D. Economou, E. S. Aydil, and G. Barna. In situ monitoring of etching uniformity in plasma reactors. *Solid-State-Technology*, 34(4):107–111, 1991.

[26] H. W. Ellis, E. W. McDaniel, D. L. Albritton, L. A. Viehland, S. L. Lin, and E. A. Mason. Transport properties of gaseous ions over a wide energy range. part ii. *Atomic Data and Nuclear Tables*, 22(3):179–217, 1978.

[27] H. W. Ellis, R. Y. Pai, E. W. McDaniel, E. A. Mason, and L. A. Viehland. Transport properties of gaseous ions. *Atomic Data and Nuclear Tables*, 17(3):178–210, 1976.

[28] A. Fiala, L. C. Pitchford, and J. P. Boeuf. Two-dimensional, hybrid model of low-pressure glow discharges. *Phys. Rev. E*, 49(6):5607–5622, 1994.

[29] W. C. Fon, K. A. Berrington, and A Hibbert. The elastic scattering of electrons from inert gases: IV. krypton. *J. Phys. B*, 17:3279–3294, 1984.

[30] A. Forghieri, R. Guerrieri, P. Ciampolini, A. Gnudi, M. Rudan, and G. Baccarani. A new discretisation strategy of the semiconductor equations comprising momentum and energy balance. *IEEE Trans. CAD*, 7(2):231, 1988.

[31] L. S. Frost and A. V. Phelps. Momentum-transfer cross sections for slow electrons in He, Ar, Kr and Xe from transport coefficients. *Phys. Rev.*, 136(6a):1538–1545, 1964.

[32] J. E. Furst, D. E. Golden, M. Mahgerefteh, J. Zhou, and D. Mueller. Absolute low-energy e^{-}-Ar scattering cross sections. *Phys. Rev. A*, 40(10):5592–5600, 1989.

[33] V. E. Golant, A. B. Zhilinsky, I. E. Sakharov, and S. C. Brown. *Fundamentals of plasma physics*. John Wiley and Sons, 1980.

[34] A. S. Gosh, C. Flacon, and D. Bhattacharya. Model potential approach to elastic electron-helium scattering. *J. Phys. B: At. Mol. Phys*, 14:4619–4626, 1981.

[35] D. B. Graves and K. F. Jensen. A continuum model of DC and RF discharges. *IEEE Trans. Plasma Sci.*, 14(2):78–91, 1986.

[36] R. Haberland, L. Fritsche, and J. Noffke. Elastic scattering of low energy electrons by Ne, Ar Kr and Xe. *Phys. Rev A*, 33(4):2305–2314, 1985.

[37] J. M. Hammersley and D. C. Handscomb. *Monte Carlo Methods*. Methuen, London, 1967.

[38] C. K. Hanish, J. W. Grizzle, H.-H. Chen, L. I. Kamlet, S. Thomas, F. L. Terry Jr, and S. W. Pang. Modeling and algorithm development for automated optical endpointing of an HBT emitter etch. *J. Electronic Materials*, 26(12):1401–1408, 1997.

[39] M. J. Higgins, M. A. Lennon, J. G. Hughes, K. L. Bell, H. B. Gilbody, A. E. Kingston, and F. J. Smith. Atomic and molecular data for fusion, part 3 ”recommended cross sections and rates for electron impact ionization of atoms and ions: Copper to uranium” CLM-R294. Technical report, Culham Laboratory, 1989.

[40] J. Hopwood. Planar RF induction plasma coupling efficiency. *Plasma Sources Sci. Technol.*, 3:460–464, 1994.

[41] J. Hopwood, C. R. Guarnieri, S. J. Whitehair, and J. J. Cuomo. Electromagnetic fields in a radio-frequency induction plasma. *J. Vac. Sci. Technol. A*, 11(1):147–151, 1993.

[42] S. R. Hunter, J. G. Carter, and L. G. Christophorou. Low-energy electron drift and scattering in krypton and xenon. *Phys. Rev A*, 38(11):5539–5551, 1988.

[43] J. H. Ingold. Moment method applied to gaseous electronics. *Phys. Rev. E*, 40(7):3855–3863, 1989.

[44] E. F. Jaeger, L. A. Berry, J. S. Tolliver, and D. B. Batchelor. Power deposition in high-density inductively coupled plasma tools for semiconductor processing. *Phys. Plasmas*, 2(6):2597, June 1995.

[45] H.-M. Katsch, A. Goehlich, T. Kawetzki, E. Quandt, and H.-F. Döbele. Attachment-induced ionization instability of a radio frequency excited discharge in oxygen. *Appl. Phys. Lett.*, 75:2023, 1999.

[46] J. H. Keller. Inductive plasmas for plasma processing. *Plasma Sources Sci. Technol.*, 5:166–172, 1996.

[47] M. Klick. Nonlinearity of the radio-frequency sheath. *J. Appl. Phys.*, 79(7):3345–3352, 1996.

[48] M. Klick and W. Rehak. RF plasma monitoring using self excited electron resonance spectroscopy. In *Proc of 12th International Symposium on Plasma Chemistry*, volume 1, page 511, Minneapolis, 1995.

[49] M. Klick, W. Rehak, W. Kasper, and P. Awakowicz. Innovative plasma diagnostics and control of process in reactive low-temperature plasmas. In *Proc. of 5th Int. Conf. on Plasma Surface Engineering*, Garmisch-Partenkirchen, 1996.

[50] L. E. Kline and M. J. Kushner. Computer simulation of materials processing plasma discharges. *Solid State and Mat. Sci*, 16(1):1–35, 1989.

[51] U. Kortshagen. On the influence of energy transfer efficiency on the electron energy distribution function in HF sustained rare gas plasmas: experimental and numerical study. *J. Phys. D: Appl. Phys.*, 26:1230–1238, 1993.

[52] U. Kortshagen, C. Busch, and L. D. Tsendin. On simplifying approaches to the solution of the Boltzmann equation in spatially inhomogeneous plasmas. *Plasma Sources Sci.Technol.*, 5:1–17, 1996.

[53] U. Kortshagen and B. G. Heil. Kinetic two-dimensional modeling of inductively coupled plasmas based on a hybrid kinetic approach. *IEEE Trans. Plasma Sci.*, 27(5):1297–1309, 1999.

[54] U. Kortshagen and L. D. Tsendin, editors. *Electron Kinetics and Applications of Glow Discharges*, chapter Optical Characterisation of RF Inductively Coupled Plasmas, page 489. Plenum Press, New York, 1998.

[55] D. Kröner. *Numerical Schemes for Conservation Laws*. Wiley, Teubner, 1997.

[56] M. Kushner. Advances in plasma equipment modeling. *Solid State Technology*, 6:135–144, 1996.

[57] R. W. LaBahn and J. Callaway. Differential cross sections for the elastic scattering of 1- to 95ev electrons from helium. *Phys. Rev.*, 2(2):366–369, 1970.

[58] J. G. Laframboise. *Theory of Spherical and Cylindrical Langmuir Probes in a Collisionless, Maxwellian Plasma at Rest*. UTIAS Rep. No. 100, Institute for Aerospace Studies, Toronto, 1966.

[59] L. T. Sin Fai Lam. Relativistic effects in electron scattering by atom III. elastic scattering by krypton, xenon and radon. *J. Phys. B: At. Molec. Phys.*, 15:119–142, 1982.

[60] M. A. Lennon, K. L. Bell, H. B. Gilbody, J. G. Hughes, A. E. Kingston, M. J. Murray, and F. J. Smith. Recommended data on the electron impact ionization of atoms and ions: Fluorine to nickel. *J.Phys. Chem. Ref. Data*, 17(3):1285–1363, 1988.

[61] J. Leroy, J. Perrin, J. Jolly, and M. Péalat. Thermal accomodation of a gas on a surface and heat transfer in CVD and PECVD experiments. *J. Phys. D: Appl. Phys*, 30:499–509, 1997.

[62] C. Li and H.-M. Wu. Three fluid transport models by particle-in-cell method for RF glow discharges. *IEEE Trans. Plasma Sci.*, 20(6):1000–1013, 1992.

[63] M. A. Liebermann and A. J. Lichtenberg. *Principles of Plasma Discharges and Materials Processing*. Wiley Interscience, New York, 1994.

[64] G. G. Lister, Y.-M. Li, and V. A. Godyak. Electrical conductivity in high-frequency plasmas. *J. Appl. Phys.*, 79(12):8993–8997, 1996.

[65] D. P. Lymberopoulos and D. Economou. Modeling and simulation of glow discharge plasma reactors. *J. Vac. Sci. Technol. A*, 12(4):1229–1236, 1994.

[66] D. P. Lymberopoulos and D. J. Economou. Fluid simulations of glow discharges: Effect of metastable atoms in argon. *J. Appl. Phys.*, 73(8):3668–3679, 1992.

[67] R. P. McEachran and A. D. Stauffer. Relativistic low-energy elastic momentum transfer cross sections for electron scattering from xenon. *J. Phys. B: At. Mol. Phys.*, 20:3483–3486, 1987.

[68] E. Meeks and M. A. Capelli. A multi-fluid stagnation-flow plasma model with a self-consistent treatment of the collisional sheath. *IEEE Trans. Plasma Sci.*, 21(6):768–777, 1993.

[69] A. Metze, D. W. Ernie, and H. J. Oskam. Application of the physics of plasma sheaths to the modelling of rf plasma reactors. *J. Appl. Phys.*, 60(9):3081–3087, 1986.

[70] P. Meyer, G. Wunner, W. Schmidt, and H. Ruder. Unified particle simulation technique for the plasma bulk and the cathode sheath of a dc glow discharge. *J. Appl. Phys.*, 77(3):992–1000, 1995.

[71] M. Meyyappan and J. P. Kreskovsky. Glow discharge simulation through solutions to the moments of the Boltzmann transport equation. *J. Appl. Phys.*, 68(4):1506, 1990.

[72] H. B. Milloy, R. W. Crompton, J. A. Rees, and A. G. Robertson. The momentum transfer cross section for electrons in argon in the energy range 0-4 eV. *Aust. J. Phys.*, 30:61, 1977.

[73] G. Mümken. *Teilchenflüsse und räumliche Profile in planaren, induktiv gekoppelten Niederdruckentladungen in Argon*. PhD thesis, Ruhr-Universität Bochum, 1998.

[74] T. E. Nitschke and D. B. Graves. A comparison of particle in cell and fluid model simulations of low-pressure radio frequency discharges. *J. Appl. Phys.*, 76(10):5646–5660, 1994.

[75] T. E. Nitschke and D. B. Graves. Matching a RF sheath model to a bulk plasma model. *IEEE Trans. Plasma Sci.*, 23(4):717–727, 1995.

[76] J. D. P. Passchier and W. J. Goedheer. A two-dimensional fluid model for an argon rf discharge. *J. Appl. Phys.*, 74(6):3744, 1993.

[77] S. Patankar. *Numerical Heat Transfer and Fluid Flow*. Hemisphere Publ., 1980.

[78] O. Pironneau. *Finite Element Methods for Fluids*. Wiley, 1989.

[79] B. Plenkiewicz, P. Plenkiewicz, P. Baillargeon, and J.-P. Jay-Gerin. Pseudopotential approach to low energy (0 - 3 eV) elastic electron-argon scattering. *Phys. Rev. A*, 36(5):2002–2007, 1987.

[80] B. Plenkiewicz, P. Plenkiewicz, C. Houee-Levin, and J.-P. Jay-Gerin. Pseudopotential calculations for elastic scattering of slow electrons (0-20eV) from noble gases. II krypton. *Phys. Rev. A*, 38(12):6120–6128, 1988.

[81] W. H. Press, S. A. Teukolsky, W. T. Vetterling, and B. P. Flannery. *Numerical Recipes in C*. Cambridge University Press, 2nd edition, 1992.

[82] Z. M. Raspopović, S. Sakadzic, S. A. Bzenic, and Z. L Petrovic. Benchmark calculations for monte carlo simulations of electron transport. *IEEE Trans. Plasma Sci.*, 27(5):1241–1248, 1999.

[83] D. D. Reid and J. M. Wahedra. Low-energy differential scattering of electrons and positrons from noble gases. *Phys. Rev. A*, 50(6):4859–4867, 1994.

[84] A. D. Richards, B. E. Thompson, and H. H. Sawin. Continuum modeling of argon radio frequnecy glow discharges. *Appl. Phys. Lett*, 50(9):492–494, 1987.

[85] K.-U. Riemann. Bohm criterion and ion-acoustic sound barrier. *Phys. Fluids B*, 3(12):3331–3338, 1991.

[86] K.-U. Riemann. The Bohm criterion and sheath formation. *J. Phys. D*, 24(4):493–518, 1991.

[87] K.-U. Riemann. The Bohm criterion and boundary conditions for a multicomponent system. *IEEE Trans. Plasma Sci.*, 23(4):709–716, 1995.

[88] A. G. Robertson. The momentum transfer cross section for low energy electrons in neon. *J. Phys. B: Atom. Molec. Phys.*, 5:648–664, 1972.

[89] H. P. Saha. Accurate ab initio calculation on the low-energy elastic scattering of electrons from helium. *Phys. Rev. A*, 40(6):2976–2990, 1989.

[90] H. P. Saha. Ab initio calculation of scattering length and cross sections at very low energies for electron-helium scattering. *Phys. Rev. A*, 48(2):1163–1170, 1993.

[91] P. Scheubert, U. Fantz, P. Awakowicz, and H. Paulin. Experimental and theoretical characterization of an inductively coupled plasma source. *accepted J. Appl. Phys.*, 2001.

[92] W. Schottky. Diffusionstheorie der positiven Säule. *Phys. Zeitschr.*, 25:635, 1924.

[93] P. Segur, A. Alkaa, S. Pineau, A Zahraoui, A. Chouki, and C. Moutarde. Kinetic description of electrons in inhomogeneous electric fields. *Plasma Sources Sci. Technol.*, 4:183–199, 1995.

[94] S. A. Self. Steady-state theory of a low-pressure discharge column in an axial magnetic field. *Phys. Fluids*, 10(7):1569, 1967.

[95] I.P. Shkarofsky, T.W. Johnston, and M.P. Bachynski. *The particle kinetics of plasmas*. Addison-Wesley, 1996.

[96] H. R. Skullerud. The stochastic computer simulation of ion motion in a gas subjected to a constant electric field. *J. Phys. D*, 1:1567, 1968.

[97] T. J. Sommerer, W. N. G. Hitchon, R. E. P. Harvey, and J. E. Lawler. Self-consistent kinetic calcuations of helium rf glow discharges. *Phys. Rev. A*, 43(8):4452–4472, 1991.

[98] T. J. Sommerer and M. J. Kushner. Numerical investigation of the kinetics and chemistry of rf glow discharge plasmas sustained in He, N_2, O_2, $He/N_2/O_2$, $He/CF_4/O_2$, and SiH_4/NH_3 using a Monte Carlo-fluid hybrid model. *J. Appl. Phys.*, 71(4):1654–1673, 1992.

[99] L. Spitzer. *Physics of Fully Ionized Gases*. John Wiley, 2nd edition, 1962.

[100] J. L. Steger and R. F. Warming. Flux vector splitting of the inviscid gasdynamic equations with application to finite difference methods. *J. Comp. Phys.*, 40:263–293, 1981.

[101] A. Steinbach. Real time plasma etch diagnostics by plasma monitoring system hercules. In *Proc. of Frontiers in Low Temperature Plasma Diagnostics III LRP 629/99*, pages 51–60, Lausanne, 1999. Centre de Recherches en Physique des Plasmas EPFL.

[102] R. A. Stewart, P. Vitello, and D. B. Graves. A two-dimensional fluid model of high density inductively coupled plasma sources. *J.Vac.Sci.Technol.B*, 12:478, 1994.

[103] R. A. Stewart, P. Vitello, D. B. Graves, and L. A. Berry. Plasma uniformity in high-density inductively coupled plasma tools. *Plasma Sources Sci. Technol*, 4:36–46, 1995.

[104] M. Surendra, D. B. Graves, and G. M. Jellum. Self-consistent model of a direct-current glow discharge: Treatment of fast electrons. *Phys. Rev. A*, 41(2):1112–1125, 1990.

[105] J. D. Swift and M. J. R. Schwar. *Electrical Probes for Plasma Diagnostics*. Iliffe, 1970.

[106] K.-U. Riemann T. Daube and H. Schmitz. Particle simulation of a magnetized plasma contacting the wall. *Phys. Plasmas*, 5(1):117–126, 1998.

[107] L. Tonks and I. Langmuir. A general theory of the plasma of an arc. *Physical Review*, 34:876–916, 1929.

[108] M. M. Turner. Simulation of kinetic effects in inductive discharges. *Plasma Sources Sci. Technol.*, 5:159–165, 1996.

[109] D. Uhrlandt, M. Schmidt, and R. Winkler. A method to solve the nonlinear kinetic equation of the “nonlocal approach” including coulomb interaction of electrons. *Computer Physics Communications*, 118:185–199, 1998.

[110] H.-B. Valentini. The theory of the low-pressure, high-current discharge column: the influence of the degree of ionization and of the neutral gas temperature on the radial profiles of the charged particle density, the neutral gas density, and on the electron temperature. *Plasmaphysik*, 12(3):151, 1979.

[111] H.-B. Valentini. Removal of singularities in the hydrodynamic description of plasmas including space-charge effects, several species of ions and non vanishing ion temperature. *J. Phys. D: Appl. Phys.*, 21:311–321, 1988.

[112] H.-B. Valentini. Sheaths, particle fluxes, floating potentials and electromotive force in a cylindrical discharge plasma containing an internal coaxial wall. *J. Phys. D: Appl. Phys*, 27:119–128, 1994.

[113] H.-B. Valentini. Sheath formation in low-pressure discharges. *Plasma Sources Sci. Technol.*, 9:574–582, 2000.

[114] H.-B. Valentini, E. Glauche, and D. Wolff. Modelling of sheaths, presheaths, current-voltage characteristics and double probes in low-pressure plasmas in coaxial and concentric geometries. *Plasma Sources Sci. Technol.*, 4:353–365, 1995.

[115] H.-B. Valentini and F. Herrmann. Boundary value problems for multi-component plasmas and a generalized Bohm criterion. *J.Phys.D: Appl.Phys.*, 29:1175, 1996.

[116] P. L. G. Ventzek, R. J. Hoekstra, and M. J. Kushner. Two-dimensional modeling of high plasma density inductively coupled sources for materials processing. *J. Vac. Sci. Technol. B*, 12(1):461–477, 1994.

[117] P. L. G. Ventzek, T. J. Sommerer, R. J. Hoekstra, and M. J. Kushner. Two-dimensional hybrid model of inductively coupled plasma sources for etching. *Appl. Phys. Lett.*, 63(5):605–607, 1993.

[118] D. A. White, B. E: Goodlin, A. E. Gower, D. S. Boning, H. Chen, H. H. Sawin, and T. J. Dalton. Low open-area endpoint detection using a PCA-based t^2 statistic and Q statistic on optical emission spectroscopy measurements. *IEEE Trans. Semicon. Manufacturing*, 13(2):193–207, 2000.

[119] F. F. Young and C.-H. Wu. A comparative study between non-equilibrium and equilibrium models of RF glow discharges. *J. Phys. D: Appl. Phys.*, 26, 1993.

[120] M. Yousfi, A. Hennad, and A. Alkaa. Monte Carlo simulation of electron swarms at low reduced electric fields. *Phys. Rev. E*, 49(4):3264–3273, 1994.

[121] B. W. Yu and S. L. Girshick. Modelling of inductively coupled plasmas: The coil current boundary condition. *J. Appl. Phys.*, 69(2):656–661, 1991.